Université de Neuchâtel

Institut de Microtechnique

Bistable GaAs Fabry-Perot and Bragg Reflector Devices for Optical Computing

Thèse

Présentée à la Faculté des sciences

pour obtenir le titre de docteur ès sciences

par

Bruno Acklin

Neuchâtel, Juin 1992

IMPRIMATUR POUR LA THÈSE

Bistable GaAs Fabry-Perot and Bragg Reflector Devices for Optical Computing

de Monsieur Bruno Acklin

UNIVERSITÉ DE NEUCHÂTEL

FACULTÉ DES SCIENCES

La Faculté des sciences de l'Université de Neuchâtel sur le rapport des membres du jury,

MM. R. Dändliker, H. Beck, F.-K. Reinhart (EPF-Lausanne), J.-L. Oudar (CNET Bagneux) et J.L. Jewell (Photonics Research, Broomfield)

autorise l'impression de la présente thèse.

Neuchâtel, le 15 juin 1992

Le doyen :

A. Robert

ABSTRACT

The nonlinear Fabry-Perot device (NLFP) is an all-optical switch with potential application in the field of parallel optical computing. It is based on an optically nonlinear spacer layer enclosed between two dielectric mirrors which form a resonant optical cavity. Modern semiconductor growth technology allows the integrated fabrication of such devices in a single epitaxial process.

A first part of my thesis presents the theoretical and experimental work which lead to the successful realization of integrated NLFP devices based on AlGaAs. A second part details my experimental investigations of the operational properties and tolerances of the fabricated devices. In the final part I discuss different aspects of the NLFP device, namely the potential for improvement by device scaling, the application and the properties of the device in a system, and finally I compare the NLFP with three other optical computing devices.

An important prerequisite for the device design is a numerical model to simulate the optical structures. In close collaboration with the Institut de Micro- et Optoélectronique (IMO) at the EPFL in Lausanne, we have developed a tool which allows the simulation of planar dielectric structures with arbitrary numbers of nonlinear layers. Due to its versatility, this program has since been used for a variety of structures and numerical experiments. In particular, we used it to optimize the nonlinear Bragg reflector devices, for which we could demonstrate bistable switching for the first time. Parallel to this, I tried to improve the analytical understanding of the device. Examples are the study of the threshold dependence, of transverse effects, and the model for critical slowing down. Also, I derived an analytical expression for the phase dispersion in a dielectric mirror, which describes an equivalent penetration depth. The importance of this lumped parameter is particularly apparent in the scaling considerations.

All of the investigated structures were grown at IMO-EPFL. They rely on bulk GaAs as the nonlinear material and different AlGaAs alloys for the dielectric mirrors. The nonlinear measurements allowed us to determine the nonlinear cross section η and the Kerr coefficient n_2, as well as the saturation properties of the carrier-induced nonlinearity in GaAs. These results, together with our demonstration of thermally stable, latched switching at a threshold as low as 1 mW, support the use of bulk GaAs as the nonlinear material in such optical devices.

In this thermally stable NLFP device I have studied critical slowing down effects. If the device is critically biased close to threshold it can be switched with a small signal increment. I have demonstrated a differential signal gain of 8 at a switching time of about 200 ns. In agreement with a simple model, the experiments reveal a constant switching energy, independent of the switching increment. This time-power trade-off indicates the existence of a gain-bandwidth product, which is essentially the relaxation rate of the nonlinear effect used.

I have studied the dependence of the device properties on transverse effects. Experiments with variable spotsize demonstrate the influence of carrier diffusion and diffraction which limit the minimal area of a Fabry-Perot device. Indeed, the scaling considerations indicate that the effective device volume, and therefore the minimal switching energy, of a NLFP cannot be reduced below a diffraction determined limit. This limit arises because of the finite longitudinal confinement imposed by the dielectric mirrors. To reduce the switching energy below this limit of about 0.2 pJ, waveguiding confinement is required.

An important concern of my work was the study and the improvement of the demanding fabrication and operating tolerances of the NLFP device. A technological limitation originates from the thickness accuracy of the epitaxial growth process. With a rapid feedback of calibration data, obtained from our optical reflection measurements, to the crystal growers at IMO-EPFL, we were able to meet the required thickness tolerances of about 0.5%. I also measured the transverse thickness gradients on the wafer surface which appear to limit the area of arrays to less than 1 mm^2 with the present technology. This is a consequence of the extreme sensitivity to variations of the operating wavelength (critical biasing), which is inherent to devices with a passive resonant cavity. My investigations indicate that this wavelength sensitivity severely restricts the operational parameters of the device, such as the achievable gain and the fan-in, and the wavelength stability of sources.

TABLE OF CONTENTS

1 **Introduction** 1
- 1.1 Some historical milestones 5
- 1.2 Approach and content of the present work 6

2 **Theoretical Part** 7
- 2.1 Nonlinear Fabry-Perot resonator (NLFP) 8
- 2.2 Nonlinear material properties 24
- 2.3 Integrated layered structures 41
- 2.4 Dielectric (Bragg) reflector 49
- 2.5 Numerical optimization 58

3 **Experimental Work** 69
- 3.1 Characterization techniques 70
- 3.2 Thickness calibration for MBE growth 81
- 3.3 Post-growth device adjustments 84
- 3.4 Nonlinear refractive index measurements 89
- 3.5 Bistable switching 95
- 3.6 Ultrashort cavity NLFP 108
- 3.7 Nonlinear Bragg reflector devices 112
- 3.8 Conclusions 117

4 **Aspects of Optical Logic Devices** 119
- 4.1 Device scaling 120
- 4.2 Modes of operation 130
- 4.3 Tolerances 140
- 4.4 Device criteria 142
- 4.5 Comparison with related devices 144

5 **Summary and Outlook** 151

Acknowledgments 155
Bibliography 157
Index 169

1 INTRODUCTION

The end of the 20th century may once be remembered as the light age (or, alternatively the dark age). Light as a broad band, long distance information carrier is already revolutionizing our potential for communication. A similar revolution is about to start in the field of computation, where the high parallelism offered by optical interconnects could widen the bottleneck of electronics: In contrast to electronic signals which are bound to mutually isolated conductors, optical signals can propagate through free space without interaction.

It is a straight forward idea to use light not only for information transport, but also for information processing, such as self routing or parallel computation. The field of photonic switching is concerned with fast all-optical switching devices, mostly for (sequential) telecommunication.

Optical computing idea

On the other hand, in the field of optical computing the emphasis lies primarily on the parallelism of light. Modern diffractive optics[1], based on holography and nano-technology, allows one to address and interconnect highly integrated two-dimensional arrays of processing elements through free-space. A proposition for an integrated interconnection architecture[2] is shown in Fig. 1.1. It is based on self-aligning planes which incorporate processing elements (GaAs-plane) and interconnection elements such as micro-lenses, beamsplitters and diffractive optical elements.

Computing algorithms and systems which make efficient use of the parallelism of light have yet to be found. A promising approach is that of neural networks[3] which offer features such as content addressability, learning capabilities, fault-tolerance, etc. They are based on simple processing elements (neurons) which perform a nonlinear operation on a number of optical input signals.

Whether future parallel processing elements will be hybrid optoelectronic devices, embodying optical detectors and sources / modulators together with electronic circuitry, or if they will be of all-optical (intrinsie) origin, such as the nonlinear Fabry-Perot device introduced in the following text, is not yet clear and in fact the distinction disappears in some cases.

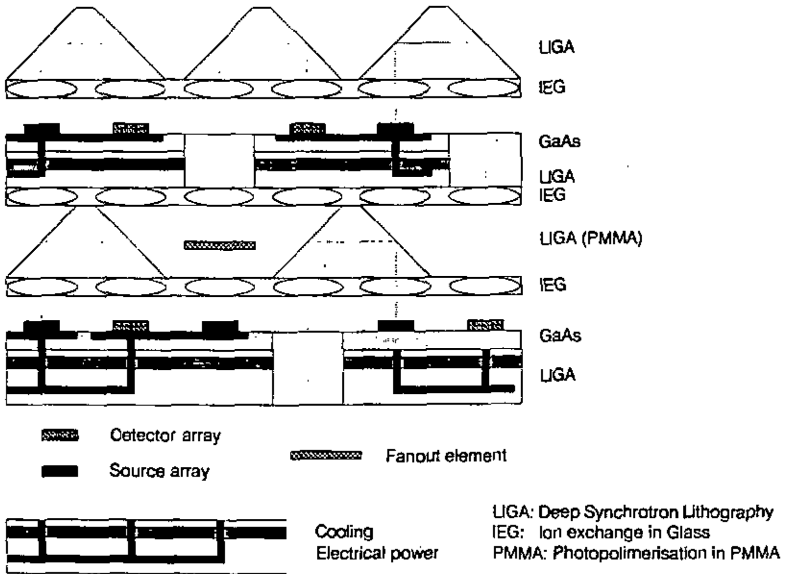

Fig. 1.1: *Proposition for an integrated optical computing system*[2] *where optical processing elements (GaAs source and detector arrays) in one plane are optically interconnected through other self-aligning planes which contain passive refractive and diffractive elements. Of interest here is the concept of combining integrated micro-optic elements, rather than the mentioned technologies to produce the micro-lenses, beamsplitters, mirrors and diffractive optics.*

Resonant nonlinear material

The basis of the "parallelism" offered by optics is that electromagnetic waves do not interact with each other. To make them interact in an optical processing element, one has to make use of the coupling between electromagnetic fields and charged particles, such as electrons in solids. This coupling is described by the electric polarization of macroscopic media which determines the refractive index n and the absorption α encountered by an optical wave. Coherent nonlinear polarization effects (characterized by nonlinear susceptibilities $\chi^{(2)}$, $\chi^{(3)}$, ..) are generally weak and extremely fast. They are used in photonic switching applications, where high speed is desired, and large signals, or alternatively, long interaction lengths, can be tolerated (note that long transit times do not limit the processing speed, for instance in systolic architectures).

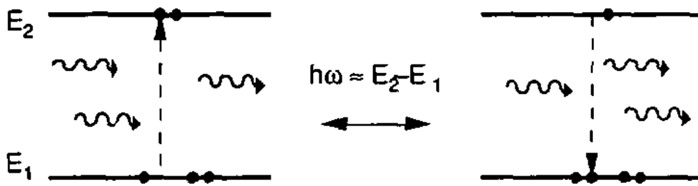

Fig. 1.2: *Resonant interaction of an optical field (photon energy $\hbar\omega$) with an electronic two level transition between energy states E_1 and E_2.*

The nonlinear polarization effects can be much larger (but correspondingly slower) if the electromagnetic field interacts resonantly with an electronic transition (Fig. 1.2). Optical nonlinearities, which couple resonantly to the bandgap of direct semiconductors, are the basis of today's optical computing devices. These large nonlinearities allow for low power signals, which are crucial to reduce the dissipation in integrated parallel systems.

Resonant optical cavity

The nonlinear optical effects provided by a material can be enhanced further if the material is placed inside a resonant optical cavity (feedback). An example is the Fabry-Perot resonator, which is based on multiple beam interference between two planar mirrors (Fig. 1.3a).

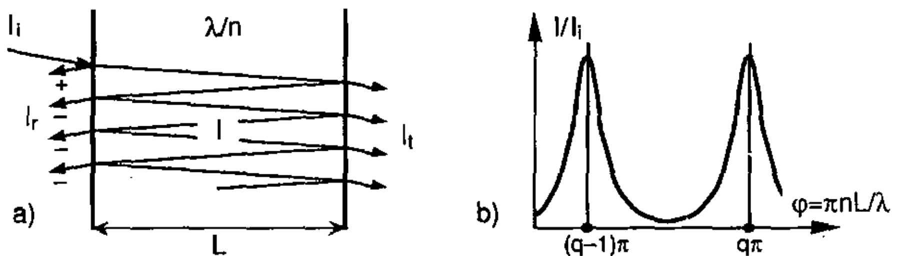

Fig. 1.3: *If an electromagnetic wave is resonant with an optical cavity (distance 2L equal to a multiple of the wavelength λ/n), the intensity I inside the cavity may be a multiple of the incident I_i, so that the transmitted intensity I_t is enhanced, while the reflected I_r is reduced.*

If the round-trip distance 2L between the two mirrors is a multiple of the optical wavelength λ/n, the optical field inside the cavity can be a multiple of the incident field (Fig. 1.3b). The reflected signal is suppressed, while the transmitted signal is enhanced. The quality or finesse of the cavity is limited by the cavity losses.

Intrinsic optical bistability

Intrinsic optical bistability based on the interplay of a nonlinear material and a surrounding resonator was suggested[4,5] in 1969. The initial propositions relied on nonlinear absorption changes, but refractive nonlinearities have proved superior for intrinsic bistability. The nonlinear Fabry-Perot (NLFP) is the prominent example for refractive nonlinear devices. Fig. 1.4 illustrates its operation principle.

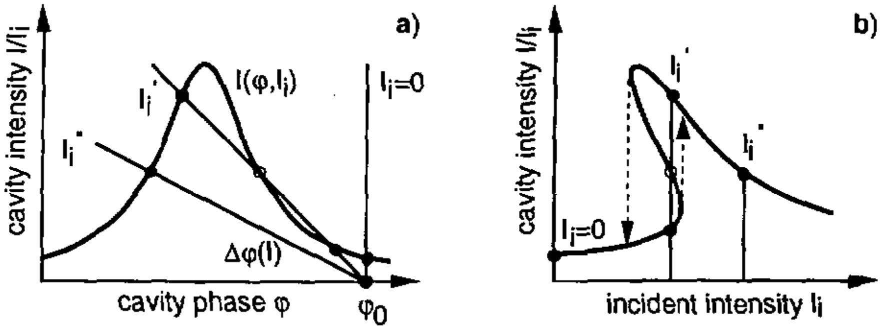

Fig. 1.4: Optical bistability based on nonlinear refraction inside a FP cavity: (a) The intensity $I(\varphi,I_i)$ in the cavity depends resonantly on the cavity phase φ. On the other hand, the nonlinear spacer material leads to a cavity phase change $\Delta\varphi(I)$ proportional to the cavity intensity I (straight lines). For a given initial detuning φ_0 and incident intensity I_i (determining the slope) one or three solutions (intersections) of these two relations exist.
(b) For a large enough initial detuning φ_0, the cavity intensity I shows a bistable hysteresis loop as a function of the incident intensity I_i.

The relative intensity I/I_i inside a Fabry-Perot resonator depends resonantly on the cavity phase φ (Fig. 1.3). On the other hand, the phase φ depends on the cavity intensity I via the nonlinear refractive index of the cavity material; in Fig. 1.4 the index change $\Delta n(I) < 0$ causes a negative phase change $\Delta\varphi(I)$ proportional to I. An increase of the (incident) intensity reduces the initial detuning φ_0 from the resonance, and thus, in turn, enlarges the cavity intensity. This positive feedback can eventually lead to optical bistability, where two stable states of phase φ and intensity I exist for one input intensity I_i. In the sketch this case is represented by three intersections; the middle intersection is unstable.

The graphical solution illustrates the fundamental requirements for optical bistability: feedback and nonlinearity. The system must contain two state variables which are mutually interdependent. One of these relations must be nonlinear.

1.1 Some historical milestones

Some significant milestones in the history of optical bistability were[6]:

Optical bistability was first observed in Na vapor[7]. It was caused by a dispersive nonlinear effect, while the researchers had been looking for absorptive bistability.

Most theoretical models for optical bistability were based on nonlinear absorption and refraction in an atomic two level system[8]. Nevertheless, the potential of the resonant nonlinearity at the gap of semiconductors was recognized early on[9].

The first observation of bistability in semiconductors was due to a thermal refractive index change in ZnS[10]. Thermal bistability has been reported in various materials since, and remarkably, nonlinear interference filters with ZnSe are still the only intrinsic optically bistable devices which have reached the level of system demonstration[11].

Bistability based on the electronic nonlinearity of a semiconductor was first observed in bulk GaAs at low temperature[12]. An intensive period of experimental and theoretical investigation began with the discovery of room temperature bistability in an AlGaAs multiple quantum well structure[13], and in GaAs[14].

The early nonlinear Fabry-Perot (NLFP) devices were based on a thin semiconductor slab which was mounted between external dielectric mirrors. Nowadays, the precise control of composition achieved with molecular beam epitaxy (MBE), allows one to integrate the dielectric mirrors together with the nonlinear material in a single growth process[15]. This capability is fundamental for the fabrication of a whole family of passive and active optoelectronic devices with potential for optical computing, such as surface emitting laser logic[16] (CELL), self-electrooptic effect device[17] (SEED) and asymmetric Fabry-Perot modulators[18] (AFPM).

The present work illustrates that bistable NLFP devices with a high finesse and moderate switching power can be fabricated. Hopefully it contributes to elucidating the tradeoffs and limitations of this approach. The next phase of improvement has already started[19] and it will involve transverse confinement of light in the material.

1.2 Approach and content of the present work

This thesis presents work conducted within the framework of a project of the Swiss National Science Foundation. At the beginning of the project, a considerable effort was consumed by the development of a simulation tool for the calculation and optimization of layered dielectric structures. Simultaneously, an experimental setup for the linear and nonlinear device characterization was elaborated and improved. Only in a second phase did we reach a feedback process of theoretical conception followed by sample growth, characterization and evaluation, which proved essential for the advancement of the project.

The thesis is structured into a theoretical, an experimental and a discussion part:

The theoretical part begins with the introduction to the lumped, dissipative Fabry-Perot cavity (Sect. 2.1), and the properties of the AlGaAs semiconductor material (Sect. 2.2), discussing the carrier rate equation which links the optical intensity with the material excitation. The simple model (Sect. 2.1.3) for a nonlinear Fabry-Perot (NLFP), based on a high finesse cavity with a Kerr-type material, is illustrative, and indeed appropriate for most NLFP. The remaining sections deal with the distributed nature of layered dielectric structures. The description of the propagation and interaction of homogeneous plane waves in layered media (Sect. 2.3) is at the origin of a numerical simulation tool. The periodic dielectric mirrors can be described analytically, and their resonant properties are at the origin of a nonlinear Bragg reflector (NLBR) device (Sect. 2.4). Numerical results from optimization and tolerancing of NLFP and NLBR devices are summarized in Section 2.5.
Similarly, the experimental part falls into two parts: Section 3.1 introduces the employed characterization techniques. The principal problem of NLFP fabrication is the small thickness tolerance of below 1%. Sections 3.2 and 3.3 describe efforts to improve the thickness calibration of the growth process, and to eventually correct the thickness after growth. The remaining sections give details on the nonlinear measurements of refractive index (Sect. 3.4), and on optical bistability experiments performed on specific devices (Sects. 3.5 to 3.7).
In Chapter 4, NLFP (and NLBR) devices are assessed from an application point of view. Starting from energy considerations, the effects of diffraction and carrier diffusion are illustrated (Sect. 4.1). Device operation is discussed in Sect. 4.2, which highlights the inherent limitations of fan-in and gain-bandwidth product. The main issue of tolerancing for resonant devices, their wavelength sensitivity, is addressed in Section 4.3. A comparison of the NLFP with three similar optical computing devices concludes the chapter (Sect. 4.4).

2 THEORETICAL PART

This chapter introduces the physical models used and developed during this work. The relevant device mechanisms can be understood from simple analytical models. Even so, the explicit design and optimization of an integrated semiconductor device requires a precise model for the light propagation in layered structures together with accurate material data.

The first Section presents the theory of a lumped Fabry-Perot cavity with an absorbing spacer and introduces the impedance matching condition for reflective devices. The principles of a nonlinear Fabry-Perot device (NLFP) are illustrated in the approximation of a Kerr-type spacer and a high finesse cavity.

Section 2 reviews the linear and nonlinear optical material properties of aluminium-gallium-arsenide (AlGaAs). The carrier rate equation which governs the time dependent interaction of material and light is discussed.

The propagation of light in layered dielectric media such as epitaxial semiconductor structures is described in Section 3. This is the basis of a numerical model to simulate and to optimize nonlinear integrated devices which has been developed in collaboration with M.A. Dupertuis and M. Proctor at the Institut de Micro- et Optoélectronique (IMO) at the EPFL in Lausanne.

The light propagation in periodic Bragg mirrors can be described analytically. In Section 4 the results of a coupled wave approach are presented and compared with exact results. This allows some considerations on the nonlinear Bragg reflector (NLBR), a device which is a closely related to the NLFP.

Section 5 describes the numerical simulation and optimization of NLFP and NLBR devices. The optimum operating wavelength, spacer thickness and dielectric mirrors are discussed. Finally, the device tolerance with respect to design parameters is addressed.

2.1 Nonlinear Fabry-Perot resonator (NLFP)

The response of a dissipative Fabry-Perot interferometer[20] to plane waves is presented first. An impedance matching condition allows one to maximize the reflection contrast of a Fabry-Perot by adapting the mirror reflectivity to the cavity loss. The operating principles of the nonlinear refractive Fabry-Perot device (NLFP) are illustrated in the high finesse or short cavity approximation.

2.1.1 Dissipative Fabry-Perot

Lumped mirrors

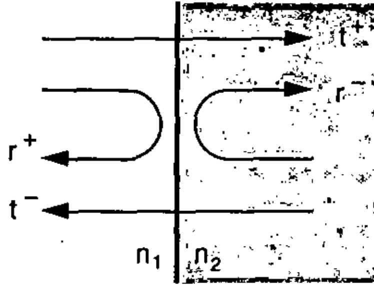

Fig. 2.1: Complex coefficients describing the reflection and the transmission of the electrical field by a lumped mirror.

The reflection and transmission properties of a mirror can be characterized by complex coefficients $r^{\pm}$ and $t^{\pm}$, respectively. These lumped mirror coefficients depend on the direction of propagation (+, –) and on the refractive indices of the media of incidence (n_1) and transmission (n_2, cf Fig. 2.1). The complex reflection and transmission coefficients $r^{\pm}$ and $t^{\pm}$ for the electrical field E are related to the corresponding coefficients R and T for the intensity by

$$r^{\pm} = \sqrt{R}\, e^{i\phi^{\pm}}, \tag{2-1}$$

$$t^{\pm} = \sqrt{\frac{n_2}{n_1}}\sqrt{T}\, e^{i\psi^{\pm}}.$$

The amplitudes of the mirror coefficients must obey energy conservation (if A represents an eventual intensity loss in the mirror), and their phases are related by

the law of reversibility

$$R + T = 1 - A\,, \qquad\qquad (2\text{-}2)$$

$$\psi \equiv \psi^- = \psi^+\,, \qquad\qquad \phi^- = \pi + 2\psi - \phi^+\,.$$

Fabry-Perot equations

A dissipative Fabry-Perot cavity (Fig. 2.2) consists of a spacer layer of thickness L, with absorption coefficient α and refractive index n, between two planar mirrors with intensity reflection and transmission coefficients R and T (indices f and b mark front and back mirrors, respectively).

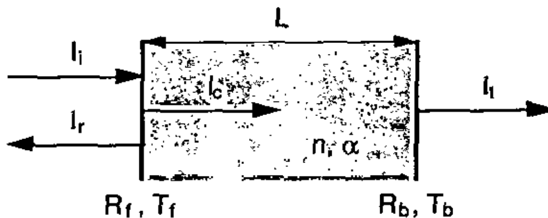

Fig. 2.2: Lumped parameters of an integrated Fabry-Perot cavity.

The well known Fabry-Perot relations are obtained from the boundary conditions for the electrical field on either side of the mirrors. The fields at the two mirrors are related by the phase and amplitude evolution in the cavity. Accordingly, the two principal cavity parameters (cf Fig. 2.3) are the cavity round-trip phase 2φ and the round trip attenuation ρ of the field (k is the vacuum wave number $2\pi/\lambda$)

$$2\varphi = 2knL + \phi_f^- + \phi_b^+\,, \qquad\qquad (2\text{-}3)$$

$$\rho = \sqrt{R_f R_b}\, e^{-\alpha L}\,.$$

By solving the boundary conditions for the electrical fields and replacing the field amplitudes by the corresponding intensities ($I = E^2/[2nZ_0]$, cf Eq. 2-65) one obtains the relationships between the intensities introduced in Fig. 2.2. It is convenient to express the incident intensity I_i, the transmitted intensity I_t, and the reflected intensity I_r as linear functions of a common parameter, the cavity intensity I_c (taken at the front mirror in forward direction):

$$I_i = I_c \frac{1}{T_f} \left[1 - 2\,\rho \cos 2\varphi + \rho^2\right] , \qquad (2\text{-}4)$$
$$I_r = I_c \frac{R_f}{T_f}\left[1 - 2\left(\frac{\rho}{\rho_f}\right)\cos 2\varphi + \left(\frac{\rho}{\rho_f}\right)^2\right],$$
$$I_t = I_c\, T_b\, e^{-\alpha L} .$$

In this, the variable ρ_f represents a normalized front mirror reflectivity

$$\rho_f \equiv \frac{R_f}{1 - A_f} . \qquad (2\text{-}5)$$

The intensity coefficients for the reflection R, the transmission T, or the absorption A (= 1–R–T) of the Fabry-Perot are obtained by eliminating the parameter I_c

$$R = (1 - A_f)\left[1 - T_{FP}(\varphi)\frac{(1-\rho_f)\,(1-\rho^2/\rho_f)}{(1-\rho)^2}\right], \qquad (2\text{-}6)$$
$$T = T_{FP}(\varphi)\,\frac{T_f\,T_b}{(1-\rho)^2}\,e^{-\alpha L} ,$$
$$A = A_f + T_{FP}(\varphi)\,\frac{T_f}{(1-\rho)^2}\left[1 - \frac{\rho^2}{\rho_f} - T_b\,e^{-\alpha L}\right].$$

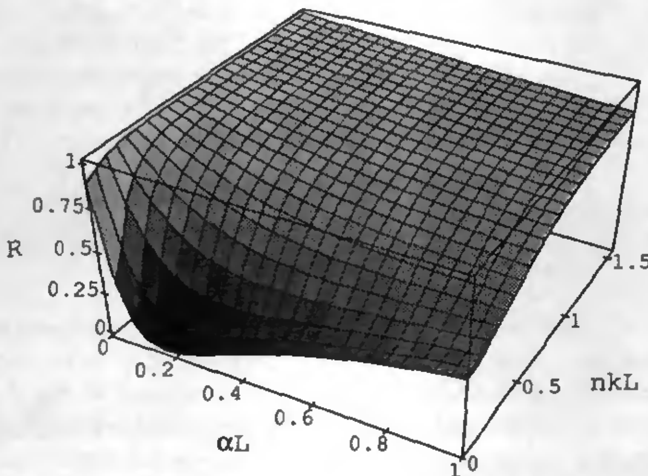

Fig. 2.3: *Reflectivity of a FP (R_f = 0.70, R_b = 0.99, A_f = A_b = 0) as a function of the amplitude and phase parameters αL and nkL.*

R, T and A are periodic functions of the cavity phase φ. The well known Airy function $T_{FP}(\varphi)$ describes the transmission of an ideal Fabry-Perot cavity

$$T_{FP}(\varphi) = \left[1 + F \sin^2\varphi\right]^{-1} ; \qquad (2\text{-}7)$$
$$F = \frac{4\rho}{(1-\rho)^2},$$

where F is sometimes called the contrast of the Fabry-Perot.

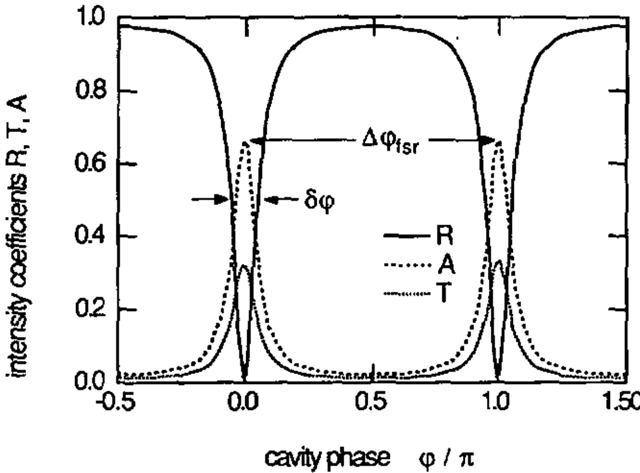

Fig. 2.4: *Reflection, transmission and absorption of a dissipative Fabry-Perot (R_f=0.7. $R_b=e^{-\alpha L}$=0.9, $A_f=A_b$=0) vs cavity phase φ: resonances with a FWHM $\delta\varphi$ are separated by the free spectral range $\Delta\varphi_{fsr} = \pi$.*

At a Fabry-Perot resonance the round trip phase 2φ is $2\pi \cdot q$. The integer q is the order of the resonance and gives the ratio of the total cavity phase φ_q to the free spectral range $\Delta\varphi_{fsr} = \pi$ between neighboring resonances

$$2\varphi_q = 2\pi q , \qquad \frac{\Delta\varphi_{fsr}}{\varphi_q} = \frac{1}{q} \approx \frac{\lambda_q}{2nL} . \qquad (2\text{-}8)$$

For the corresponding wavenumbers $k_q = 2\pi/\lambda_q$, the intracavity intensity (Eq. 2-4) and thus the transmitted intensity take a maximum with respect to the incident intensity (Fig. 2.4). As one is generally interested in the vicinity of a resonance $q \neq 0$, φ rather denotes the deviation or detuning from φ_q rather than the absolute cavity phase.

The finesse $\mathcal{F}$ of a Fabry-Perot is defined as the ratio of the free spectral range ($\Delta\varphi_{fsr} = \pi$) to the FWHM $\delta\varphi$ of the resonance. The finesse $\mathcal{F}$ is proportional to the square root of the contrast F:

$$\mathcal{F} \equiv \frac{\Delta\varphi_{fsr}}{\delta\varphi} = \frac{\pi\sqrt{\rho}}{1-\rho} = \sqrt{F}\,\frac{\pi}{2}\,. \tag{2-9}$$

Oblique incidence

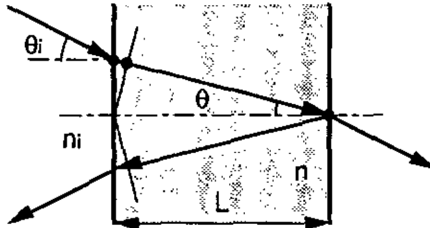

Fig. 2.5: Oblique incidence: the optical path, and thus the attenuation, in a layer of thickness L is increased to L/cosθ, but reflected wavefronts (round-trip phase) interfere after a reduced distance Lcosθ. (Snell's law relates θ to the angle of incidence: $n_i \sin\theta_i = n \sin\theta$).

The above equations were derived for normally incident plane waves. Figure 2.5 illustrates a plane wave which is incident at an oblique angle $\theta_i \neq 0$ on a layer of thickness L. For $n_i \neq n$, the internal propagation angle θ differs from θ_i, according to Snell's law of refraction (cf Eq. 2-57). The optical path through the layer is enlarged to $L/\cos\theta$, and therefore the attenuation increases. On the other hand, the distance after which a reflected wavefront coincides with itself, corresponding to the round-trip phase 2φ, is shortened to $L\cos\theta$. Thus, the change of the detuning φ and the attenuation ρ in a FP is (assuming constant mirror reflectivities and small deviations $\theta \ll 1$)

$$\frac{\Delta\varphi(\theta)}{\varphi} = \frac{\Delta\lambda_q(\theta)}{\lambda_q} = \log(\cos\theta) \approx -\frac{\theta^2}{2}\,, \tag{2-10}$$

$$\frac{\Delta\rho(\theta)}{\rho} = \alpha L\left[1 - \frac{1}{\cos\theta}\right] \approx -\,\alpha L\,\frac{\theta^2}{2}\,.$$

As a consequence, for non-normally incident plane waves, the FP resonances shift to the blue and they broaden because the loss in the spacer increases.

2.1.2 Impedance matching condition

Early papers on optical bistability dealt with ring or Fabry-Perot cavities used in transmission. Wherrett[21] suggested the use of NLFP in reflection, for several reasons: the threshold can be lowered by a factor ≤ 2 (also noted by Miller[22]), better throughput and contrast can be obtained, transverse defocusing effects reduce the reflected intensity in the low ON state (better contrast), and finally, the substrate of an epitaxially grown device does not have to be removed by etching, but is available for heat sinking.

Obviously in a reflective type device any *transmitted* power does not contribute to the nonlinearity and the throughput. The optimum rear mirror reflectivity is therefore unity

$$R_b^{opt} = 1 \,. \tag{2-11}$$

To optimize the front mirror, consider the reflectivity of a dissipative FP as the front mirror reflectivity ρ_f or the attenuation ρ changes (cf Fig. 2.3). The reflectivities at resonance and at antiresonance follow from Eq. 2-6

$$R\,|_{\varphi=0} = \frac{1-A_f}{\rho_f}\,\frac{(\rho_f-\rho)^2}{(1-\rho)^2} \equiv G(\rho_f,\rho)\,, \tag{2-12}$$

$$R\,|_{\varphi=\pm\pi/2} = G(\rho_f,-\rho)\,.$$

They are described by the same function G, for positive and negative arguments ρ and $-\rho$, respectively.

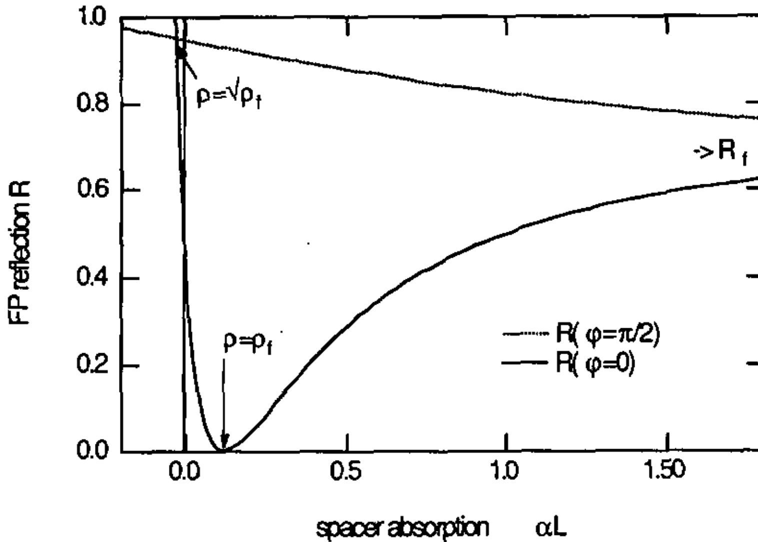

Fig. 2.6: Reflectivity of a dissipative FP at resonance and at antiresonance as a function of the absorption in the spacer (R_f=0.7, A_f=0.05, R_b=0.99).

Figure 2.6 shows the FP reflectivity as a function of the spacer absorption αL. The reflectivity on resonance vanishes if the mirror reflectivities and the spacer absorption satisfy

$$R_f = R_b\,(1-A_f)^2\,e^{-2\alpha L}\,, \qquad \text{or} \qquad (2\text{-}13)$$

$$\rho_f = \rho\,.$$

This condition has been named[23] impedance matching condition. It promises an infinite contrast ratio, which is robust to small deviations because of the quadratic dependence. At the same time the throughput, estimated by the reflectivity at an antiresonance, is close to unity (for large F)

$$R\,\big|_{(\varphi=\pi/2;\,\rho=\rho_f)} = \frac{1-A_f}{1+1/F}\,. \qquad (2\text{-}14)$$

In comparison, for a device optimized for transmission[22], the corresponding contrast ratio (transmission at resonance to transmission at antiresonance) is F+1, and the maximum transmission is less than 1/4 according to Eq. 2-6.

2.1.3 Analytic theory of the nonlinear Fabry-Perot

In his theory on the refractive nonlinear Fabry-Perot with linear background absorption, Miller[22] developed analytic optimization criteria for NLFP with a Kerr-type nonlinearity ($\Delta n = n_2 I$). The approach presented here to illustrate the operation and optimization of a NLFP differs in two points: Firstly, it is restricted to high finesse cavities, which is justified for the present NLFP devices. Secondly, it assumes a material where the nonlinear refractive index change Δn is proportional to the ambipolar carrier density N (or equivalently, a constant nonlinear cross-section $\eta = \partial n/\partial N$). The carrier density N is related to the intensity I by a carrier rate equation (cf Eq. 2-45). Under steady state conditions however, this nonlinearity is equivalent to a Kerr-type nonlinearity. The influence of nonlinear index saturation (cf Sect. 3.4.3) and absorption saturation on the NLFP are addressed.

High finesse approximation (HFA)

The epitaxially grown, integrated FP devices presented here have a typical finesse $\mathcal{F} \approx 30$, and values of $\mathcal{F} \geq 160$ have been reported[24]. The approximation $e^{-\alpha L} \approx 1-\alpha L$ is correct to 1% if the finesse $\mathcal{F}$ is larger than 10. Similarly, $\sin\varphi \approx \varphi$ is accurate to 1% in a vicinity $|\varphi| \leq 0.25$, which is larger than the resonance width $\delta\varphi = \pi/\mathcal{F}$. Thus, the shortcomings of the following model reside rather in the accuracy of the material parameters η and α, than in the high finesse approximation (HFA).

Feedback: balanced resonator

Any absorption in the mirrors (A_f, A_b) as well as the transmission of the rear mirror T_b represent undesired losses, because they reduce the finesse but do not contribute to the nonlinear effect. In an efficient cavity, therefore, these losses have to be small with respect to the principal dissipative term αL and the front mirror transmission T_f.

An optimized reflective FP cavity which fulfills the condition $R_b = 1$ together with the impedance matching condition (Eq. 2-13) represents a balanced cavity: the coupling penalty (the front mirror transmission T_f) is equal to the dissipative loss $2\alpha L$ (of the intensity) in the spacer

$$T_f \approx 2\alpha L\,. \tag{2-15}$$

The optimization of transmitting devices by minimizing the switching intensity[22] leads to an identical condition, with T_f+T_b rather than T_f representing the coupling losses. Thus, in any efficient and balanced cavity the round-trip attenuation ρ (Eq. 2-3) is, in the HFA,

$$1-\rho \approx 2\alpha L\,. \tag{2-16}$$

This simplifies the convenient finesse parameter $\sqrt{F}$ ($= 2\mathcal{F}/\pi = 2/\delta\varphi$) to

$$\sqrt{F} = -\sinh^{-1}\left[\frac{1}{2}\ln\rho\right] \approx \frac{1}{\alpha L}\,. \tag{2-17}$$

In a high finesse cavity the exponential attenuation of the intensity during a single round trip is small. Forward and backward waves interfere to a standing wave inside the cavity, but carrier diffusion (cf Sect. 2.2.3) bleaches the corresponding longitudinal variations of the carrier density. Therefore, it is convenient to use a spatially averaged cavity intensity I based on the incoherent sum of forward and backward intensities $I_c^{\pm}$ (Eq. 2-4)

$$I(\varphi) \approx I_i\,\sqrt{F}\;T_{FP}(\varphi) \approx I_i\,\sqrt{F}\,(1+F\varphi^2)^{-1}\,. \tag{2-18}$$

Also, the resonance of high finesse cavities is well approximated by a Lorentzian.

Nonlinearity: Kerr-type spacer

The nonlinear properties of the semiconductor spacer material will be described in Section 2.2. Here, a refractive index change Δn proportional to the change ΔN of the free carrier density, or a constant nonlinear refractive cross-section η, is assumed:

$$\Delta n = \frac{\partial n}{\partial N}\,\Delta N = \eta\,\Delta N\,, \qquad\qquad \Delta N = N - N_{th}\,. \tag{2-19}$$

The thermal carrier density N_{th} can often be neglected compared to N. The creation of carriers by the optical intensity I absorbed in the spacer is described by a carrier rate equation (cf Eq. 2-45). For steady state conditions, this relation reduces to a linear relationship between N and I ($\hbar\omega$ is the photon energy)

$$\Delta N(I) = \frac{\tau\,\alpha}{\hbar\omega}\,I\,. \tag{2-20}$$

For resonant semiconductor nonlinearities (cf Sect. 2.2.2) this approximation is valid for time scales larger than the carrier recombination time τ and for low excitation so that α is about constant. In this case, the refractive index change Δn is about proportional to the intensity I, and the material can be characterized by a phenomenological Kerr coefficient n_2

$$\Delta n(I) = \frac{\partial n}{\partial N}\frac{\partial N}{\partial I} I = \eta \frac{\tau\alpha}{\hbar\omega} I = n_2 I . \tag{2-21}$$

The nonlinear refractive index change Δn induces a phase change $\varphi - \varphi_0 = kL\Delta n$ in the cavity (Eq. 2-3), where φ_0 is the initial phase detuning from resonance. This leads to a second (linear) relationship between cavity phase φ and intensity I

$$\varphi - \varphi_0 = \frac{1}{\sqrt{F}}\frac{I}{\iota} ; \qquad \iota \equiv \frac{\hbar c}{\eta\tau} , \tag{2-22}$$

which has to be fulfilled together with the feedback relation of Eq. 2-18. The material parameters η and τ define the normalization parameter ι for the cavity intensity at steady state conditions.

Optical bistability

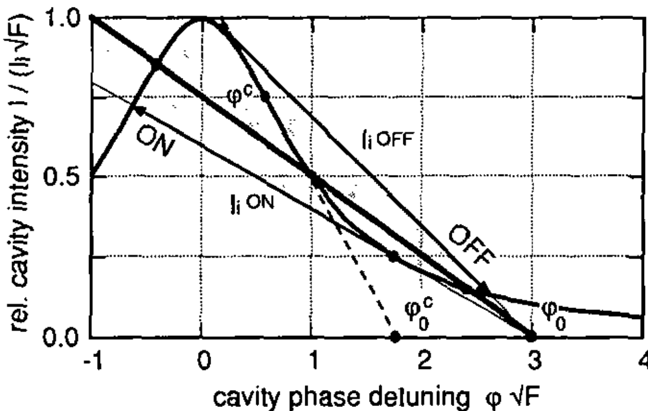

Fig. 2.7: Graphical solution for bistability in a NLFP with Kerr-type nonlinearity: if the initial detuning φ_0 is larger than the critical detuning $\varphi_0{}^c$, there is a bistable regime which is delimited by the thresholds I_i^{ON} and I_i^{OFF} (the slope of the straight lines decreases with the incident intensity).

Figure 2.7 illustrates the graphical solution of this nonlinear feedback situation between the cavity intensity I and phase φ of a NLFP. The Lorentz function represents the ratio of the cavity intensity to the incident intensity (Eq. 2-18), which peaks at resonance. The phase shift proportional to the cavity intensity (Eq. 2-22) is expressed by straight lines. Intersections of a straight line with the Lorentz function correspond to stationary states (I,φ). Three intersections indicate a bistable state; a stability analysis shows that the middle stationary state is unstable. Switching transitions start at tangential points (I^{ON}, I^{OFF}).

Critical switching condition

The point of inflection at φ^c reveals a necessary condition for bistability in a refractive NLFP: three stationary states exist only if the initial cavity detuning φ_0 exceeds a critical detuning $\varphi_0{}^c$ which is about one resonance width

$$\varphi^c = \frac{1}{\sqrt{3}} \frac{1}{\sqrt{F}}, \tag{2-23}$$
$$\varphi_0^c = \sqrt{3}\, \frac{1}{\sqrt{F}}.$$

The corresponding nonlinear phase change $\Delta\varphi^c = \varphi^c - \varphi_0{}^c$ determines the minimum threshold intensity $I_i{}^c$ and cavity intensity I^c at which switching can occur

$$I_i^c = \frac{8}{3\sqrt{3}} \frac{\iota}{\sqrt{F}}, \tag{2-24}$$
$$I^c = \frac{2}{\sqrt{3}}\,\iota.$$

According to equations 2-23 and 2-24 the critical phase change $\Delta\varphi^c$ and the threshold intensity $I_i{}^c$ can be reduced arbitrarily by increasing the finesse, for instance by reducing the spacer thickness. In reality however, the achievable finesse is limited by device fabrication and operating tolerances (cf Sect. 2.5.1).

On the other hand, the critical intensity I^c inside the cavity is determined by the material parameter ι (Eq. 2-22) and is thus independent of the cavity (finesse). Similarly, a critical carrier density N^c, or equivalently a nonlinear index change

$$\Delta n^c = \eta\, N^c = \frac{\lambda\alpha}{\pi\sqrt{3}}, \tag{2-25}$$

which both depend on the material only, have to be reached in the cavity. This requirement for a minimum carrier density inside the spacer corresponds to an absorbed energy which is used to introduce a material figure of merit and to discuss device scaling issues in Section 4.1.

Hysteresis region

If the initial detuning φ_0 exceeds the critical detuning φ_0^c, two distinct thresholds I_i^{ON} and I_i^{OFF}, larger than I_i^c, determine a region of hysteresis (Fig. 2.8). The switching transitions into and out off resonance involve a finite cavity phase change $\Delta\varphi$, related to a change of index and carrier density (Fig. 2.7).

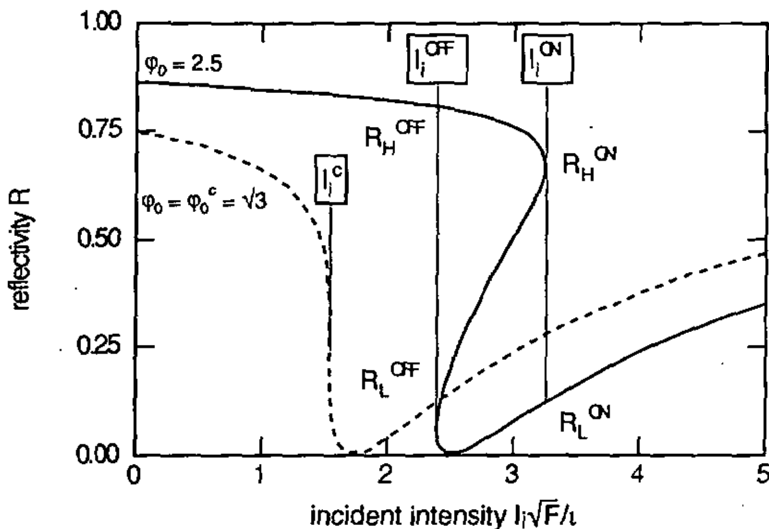

Fig. 2.8 *If $\varphi_0 \geq \varphi_0^c$, the reflectivity vs the incident intensity exhibits a hysteresis loop, delimited by the thresholds I_i^{ON}, and I_i^{OFF}. R_H^{ON} and R_L^{ON} are the high and low reflectivities at switch-ON, while R_L^{OFF} and R_H^{OFF} are the low and high reflectivities at switch-OFF.*

The threshold I_i^{ON} increases faster with the initial detuning $\varphi_0 > \varphi_0^c$ than I_i^{OFF}, which causes a widening of the hysteresis loop (Fig. 2.9a). For large φ_0, the thresholds evolve as

$$I_i^{ON}(\varphi_0) \rightarrow 4\,\frac{\iota}{\sqrt{F}}\left(\frac{\varphi_0}{\varphi_0^c}\right)^3, \qquad I_i^{OFF}(\varphi_0) \rightarrow \sqrt{3}\,\frac{\iota}{\sqrt{F}}\left(\frac{\varphi_0}{\varphi_0^c}\right). \tag{2-26}$$

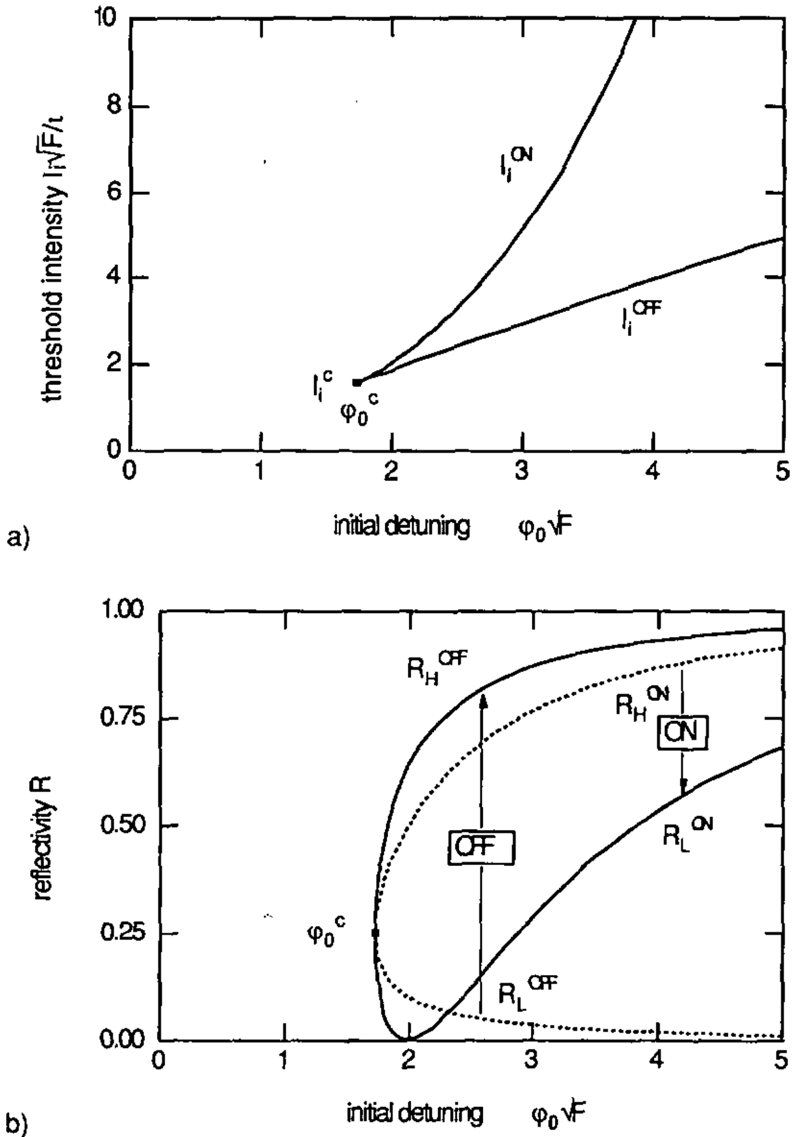

Fig. 2.9: *Bistable hysteresis loop as a function of the initial detuning j0:*
a) Increase of the switching thresholds I_i^{ON} (switch-ON) and I_i^{OFF} (switch-OFF).
b) Reflectivities before (dashed line) and after (solid line) switch-ON (R_H^{ON}, R_L^{ON}), and switch-OFF (R_L^{OFF}, R_H^{OFF}) transitions.

For a cavity with a high rear reflectivity ($R_b \approx 1$), the phase dependent reflectivity $R(\varphi)$ is the complement of the cavity absorption $A(\varphi)$

$$1 - R(\varphi) \approx A(\varphi) \approx T_{FP}(\varphi) = \frac{I(\varphi)}{\sqrt{F} I_i}, \qquad (2\text{-}27)$$

which, for an impedance matched cavity ($\rho = R_f$, $A_f \approx 0$), is equal to the normalized cavity intensity (Eq. 2-18). Using this relation, the reflectivities before and after the switching ON transition, R_H^{ON} and R_L^{ON}, and before and after the switching OFF transition, R_L^{OFF} and R_H^{OFF}, can be determined as a function of the initial detuning φ_0 (Fig. 2.9b). A high contrast ratio at switching ON is obtained for $\varphi_0 = 2$, but in this case the reflectivity before switching, and thus the throughput, is only 0.5. For a higher detuning (and a wider hysteresis loop) the ON contrast ratio (R_H^{ON}/R_L^{ON}) decreases, while the OFF contrast ratio (R_H^{OFF}/R_L^{OFF}) increases monotonically.

Index saturation

The carrier dependent nonlinear effects tend to saturate at high excitation. Some mechanisms will be discussed in Section 2.2.2 and quantitative measurements of refractive index saturation will be presented in Section 3.4. E. Garmire[23] has proposed a simple model which replaces the Kerr-type nonlinearity in Eq. 2-21 by a phenomenological two-level saturation model (cf Eq. 2-41)

$$\Delta n(I) = \Delta n_s \frac{I/I_s}{1 + I/I_s}. \qquad (2\text{-}28)$$

At the saturating intensity I_s the index change reaches half the saturating value Δn_s. For $I \ll I_s$, the model corresponds to a Kerr-type material ($n_2 \rightarrow \Delta n_s/I_s$).

The impact of saturation is shown in Fig. 2.10. A nonlinear relation with a nonlinear phase shift $\varphi - \varphi_0$ limited by a saturating phase shift $\Delta\varphi_s$ replaces Eq. 2-22

$$\varphi - \varphi_0 = \Delta\varphi_s \frac{I/I_s}{1 + I/I_s}; \qquad \Delta\varphi_s = kL\, \Delta n_s. \qquad (2\text{-}29)$$

A critical condition analog to Eq. 2-23, where $dI/d\varphi = 0$ and $d^2I/d\varphi^2 = 0$, leads to a *minimum saturating phase shift*

$$\Delta\varphi_s \geq \frac{4}{\sqrt{F}}. \qquad (2\text{-}30)$$

This condition determines a minimum saturating phase shift $\Delta\varphi_s$ for a given cavity finesse $\sqrt{F}$, or alternatively, it can also be viewed as a minimum critical cavity finesse for a given saturating phase shift[25]. Clearly, the saturating phase change $\Delta\varphi_s$ must be larger (by a factor $2/\sqrt{3}$) than the critical phase change $\Delta\varphi^c$ derived for a nonsaturating nonlinearity (Eq. 2-25). The case where $\Delta\varphi_s$ is minimum is illustrated in Fig. 2.10: Because of the nonlinear relation of Eq. 2-29 the critical initial detuning $\varphi_0{}^c$ $(3/\sqrt{F})$ and the critical detuning φ^c $(1/\sqrt{F})$ both occur at larger detuning $(\sqrt{3})$ than for the nonsaturating material (Eq. 2-23). As a consequence, the required change in refractive index is also larger by a factor $\sqrt{3}$.

For an impedance matched, or any balanced cavity the finesse is $\sqrt{F} = 1/(\alpha L)$ (Eq. 2-17), so that Eq. 2-30 reduces to the condition

$$\Delta n_s \geq \frac{2\lambda\alpha}{\pi} \qquad (2\text{-}31)$$

for the nonlinear material. For a poor nonlinear material this condition can be relaxed slightly by using an unbalanced cavity with higher mirror reflectivities ($\Delta n_s^c \geq \lambda\alpha/\pi$ for $T_f, T_b \ll \alpha L$), which, however, reduces the contrast.

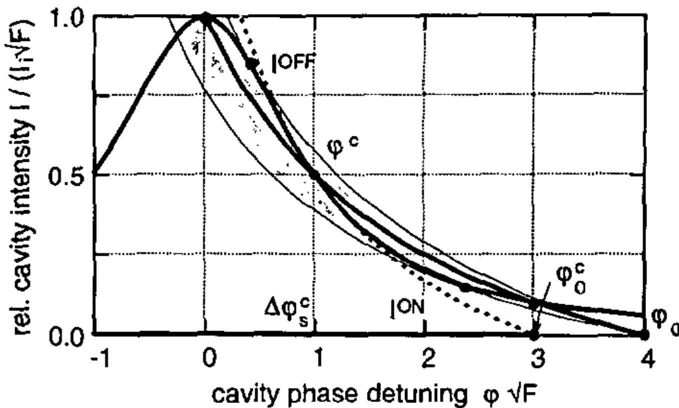

Fig. 2.10 *NLFP with saturating nonlinear index: the material relation $\Delta\varphi(I)$ becomes nonlinear (Eq. 2-29). There is a minimum saturating phase shift $\Delta\varphi_s^c \geq 4/\sqrt{F}$ (solid line at the bottom). In this case (dotted line), the critical initial detuning φ_0^c is $3/\sqrt{F}$ (instead of $\sqrt{3}/\sqrt{F}$ in Eq. 2-23).*

Absorption saturation

The large refractive nonlinearity close to a resonant electronic transition is accompanied by significant absorption effects (cf Fig. 2.16). The influence of absorption changes on a (refractive) NLFP is therefore briefly addressed.

The intensity in a Fabry-Perot cavity depends on the absorption via the finesse. Its change with absorption, at constant incident intensity and detuning, is (Eq. 2-18)

$$\frac{dI}{d\alpha} = I(\varphi)\,\frac{F\varphi^2-1}{F\varphi^2+1}\,\frac{1+\rho^2}{1-\rho^2}\,\frac{L}{2}\,. \tag{2-32}$$

Thus, for increasing absorption ($\partial\alpha/\partial I > 0$), the cavity intensity I augments for a detuning outside the FWHM ($|\varphi| > \delta\varphi/2 = 1/[2\sqrt{F}]$, Fig. 2.11).

On the opposite, a saturating absorption ($\partial\alpha/\partial I < 0$) leads to an intensity increase ($\partial I/\partial\alpha < 0$) for phases within the FWHM. This positive feedback is the origin of absorptive bistability. Its highly resonant mechanism explains why absorptive bistability was observed in specially prepared narrow line-width two-level systems only, five years after the observation of refractive bistability[26].

During a switching transition in a refractive NLFP the phase φ moves into resonance, from a critical detuning φ larger than $\delta\varphi$ (Eq. 2-23). Therefore, an absorption increase is welcome at low intensities, while absorption saturation contributes favorably once the phase has shifted into resonance.

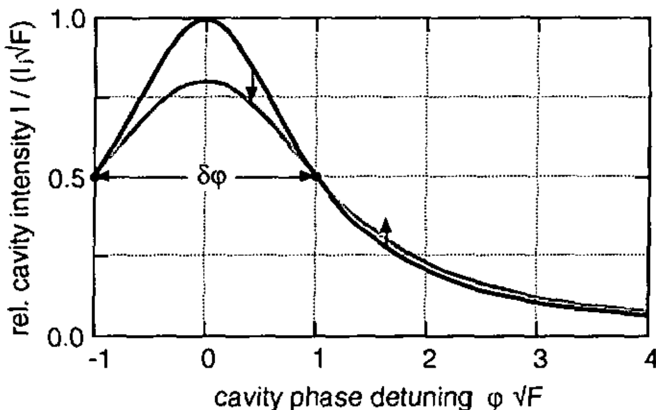

Fig. 2.11: On increasing absorption ($\partial\alpha/\partial I > 0$), the cavity intensity decreases within the FWHM of the resonance, but increases elsewhere.

2.2 Nonlinear material properties

Nonlinear optics is restricted to electromagnetic interaction in macroscopic media. (Electrical fields up to 10^8 Vm^{-1} produced by lasers are negligible compared to 10^{20} Vm^{-1} required for vacuum polarization effects.)

This section introduces the dielectric properties governing the light propagation in a material. Of particular interest are the resonant phenomena at the inter-band transition of the direct semiconductor AlGaAs.

2.2.1 Interaction of light and matter

Dielectric properties

The propagation of the electrical and magnetic fields **E** and **H** of an electromagnetic wave is governed by the macroscopic Maxwell equations[27]

$$\nabla\wedge\mathbf{E} + \dot{\mathbf{B}} = 0\,, \qquad \nabla\mathbf{B} = 0\,, \tag{2-33}$$
$$\nabla\wedge\mathbf{H} - \dot{\mathbf{D}} = \mathbf{j}\,, \qquad \nabla\mathbf{D} = \rho\;.$$

In dielectric materials, the charge density ρ and the current density **j** vanish. The relations between the macroscopic and microscopic fields are determined by the polarization **P** and the magnetization **M** of the material

$$\mathbf{D}(\mathbf{E}) = \varepsilon_0\,\mathbf{E} + \mathbf{P} \approx \varepsilon_0\varepsilon\,\mathbf{E}, \tag{2-34}$$
$$\mathbf{H}(\mathbf{B}) = \frac{1}{\mu_0}\,\mathbf{B} - \mathbf{M} \approx \frac{1}{\mu_0\mu}\,\mathbf{B}.$$

In the MKSA system, the magnetic and electric field constants, μ_0 and ε_0, are defined by $\mu_0 = 4\pi\cdot10^{-7}$ Vs/Am and $\mu_0\varepsilon_0 = 1/c^2$, respectively, where c is the vacuum speed of light (cf. Eq. 2-55). The dielectric permittivity ε and the magnetic permeability μ are the linear Taylor coefficients of the relations **D**(**E**) and **B**(**H**), respectively. In isotropic media the tensors ε and μ reduce to scalars. Except for ferromagnetic materials, the magnetization **M** is generally small, so that $\mu \approx 1$ can be assumed. The electric polarization **P** however, is generally frequency dependent (dispersion). Thus, the use of the frequency domain is appropriate, where fields have a harmonic time dependence $\mathbf{E}(\mathbf{x},t) = \mathrm{Re}\{\mathbf{E}_\omega(\mathbf{x})\,e^{-i\omega t}\}$. Then, the time-

dependent wave equation which follows from the Maxwell equations reduces to the Helmholtz equation for the complex Fourier component $\mathbf{E}_\omega(\mathbf{x})$

$$\nabla^2\mathbf{E}_\omega(\mathbf{x}) + \frac{\omega^2}{c^2}\mu\tilde{\varepsilon}(\omega)\,\mathbf{E}_\omega(\mathbf{x}) = 0\,. \tag{2-35}$$

The dielectric material properties are described by the complex dielectric function $\tilde{\varepsilon}(\omega)$, or the electrical susceptibility $\tilde{\chi}(\omega)$

$$\tilde{\varepsilon}(\omega) = \varepsilon'(\omega) + i\varepsilon''(\omega) = 1 + \tilde{\chi}(\omega)\,. \tag{2-36}$$

The real and the imaginary part ε' and ε'' describe the reactive and the dissipative polarization properties of the material. Due to the causality ($\chi[t<0] = 0$) of the linear material response, ε' and ε'' are related by the well-known Kramers-Kronig relations (P denotes the principal value of the integral)

$$\varepsilon'(\omega) - 1 = \frac{2}{\pi}\,P\int_0^\infty d\varpi\,\frac{\varpi\,\varepsilon''(\varpi)}{\varpi^2 - \omega^2}\,, \tag{2-37}$$

$$\varepsilon''(\omega) = -\,\omega\frac{2}{\pi}\,P\int_0^\infty d\varpi\,\frac{\varepsilon'(\varpi) - 1}{\varpi^2 - \omega^2}\,.$$

They are closely related to the refractive index $n(\omega)$ and the absorption coefficient $\alpha(\omega)$ which describe the phase velocity and the intensity attenuation of plane harmonic waves (cf Sect. 2.3.1)

$$n(\omega) = \sqrt{\frac{\mu}{2}\left[\varepsilon'(\omega) + \sqrt{\varepsilon'(\omega)^2 + \varepsilon''(\omega)^2}\,\right]} \approx \sqrt{\mu\varepsilon'(\omega)}\,, \tag{2-38}$$

$$\alpha(\omega) = \frac{\omega}{n(\omega)c}\,\mu\varepsilon''(\omega) = \mu Z_0\frac{\sigma(\omega)}{n(\omega)}\,.$$

The approximation is valid in most non-conductors ($\varepsilon'' \ll \varepsilon'$). In conducting media ($\sigma \neq 0$), Ohms law for the current density $\mathbf{j} = \sigma\mathbf{E}$ gives an additional dissipative contribution (resonant at $\omega = 0$) to the imaginary part of the dielectric function: $\varepsilon'' = \sigma/\omega\varepsilon_0$. Alternatively, any dissipation ε'' can be attributed to an AC-conductivity $\sigma(\omega) = \omega\varepsilon_0\varepsilon''(\omega)$.

Linear oscillator model (Lorentz)

The oscillator model[27] illustrates the dielectric material properties in the vicinity of a resonance (ω_0). In this simple phenomenological model, the material is described as a set of damped oscillators (of density N_0, mass m, charge e and damping constant γ), driven by a harmonic electrical field $E_\omega\, e^{-i\omega t}$

$$\ddot{x} + 2\gamma \dot{x} + \omega_0^2\, x = \frac{-e\, E_\omega}{m} e^{-i\omega t}. \tag{2-39}$$

The solution of this equation of motion (assuming $\omega \approx \omega_0$, $\gamma \ll \omega_0$) leads to a simple model for the susceptibility close to the resonance at ω_0 (ω_{pl} is the plasma frequency)

$$\tilde{\chi}(\omega) = N_0 \frac{-e x_\omega}{\varepsilon_0 E_\omega} \approx \frac{\omega_{pl}^2}{2\omega_0} \left(\frac{-\Delta\omega + i\gamma}{\Delta\omega^2 + \gamma^2} \right); \tag{2-40}$$

$$\omega_{pl} = \sqrt{\frac{N_0 e^2}{\varepsilon_0 m}}, \qquad \Delta\omega \equiv \omega - \omega_0 .$$

The resulting (Lorentzian) absorption peak and the anomalous dispersion region of the refractive index shown in Fig. 2.12 are typical for the dielectric properties near an atomic resonance.

Saturation of a two-level system (power broadening)

The early theories[28] on optical bistability were based on the resonant nonlinearity of (homogeneously broadened) two-level atoms, with an energy difference $\hbar\omega_0 = E_2 - E_1$ between the two eigenstates $|1\rangle$ and $|2\rangle$ as it is sketched in Fig. 1.2. A solution for the dielectric susceptibility $\tilde{\chi}$ is[29]

$$\tilde{\chi} = \chi_0\, \tilde{g}(\Delta\omega)\, \Delta N(I); \qquad \chi_0 = \frac{N_0\, d_{21}^2}{\varepsilon_0\, \hbar}, \tag{2-41}$$

$$\tilde{g}(\Delta\omega) = \frac{-\Delta\omega + i\gamma}{\Delta\omega^2 + \gamma^2}, \qquad \Delta N(I) = \frac{\Delta\omega^2 + \gamma^2}{\Delta\omega^2 + \gamma^2\,(1 + I/I_s)},$$

$$\frac{I}{I_s} \equiv \left(\frac{\omega_R}{\gamma} \right)^2, \qquad \omega_R \equiv \frac{d_{21} E_\omega}{\hbar}.$$

The amplitude χ_0 is characterized by the quantum-mechanical dipole matrix element $d_{21} = \langle 2|ex|1\rangle$ which is closely related to the plasma frequency of a classical electronic oscillator. The term $\tilde{g}(\Delta\omega)$ describes the same resonant frequency dependence (Fig. 2.12) as the oscillator model (Eq. 2-40). Indeed, the

two solutions are formally identical in the linear case (I=0), where all two-level atoms are in the lower state (population difference, or inversion $\Delta N=1$).

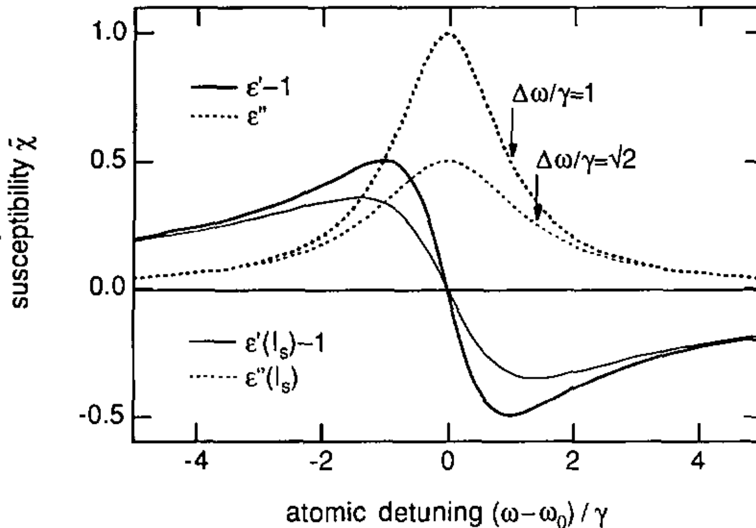

Fig. 2.12: Solid and dashed lines show the reactive ($\varepsilon'-1$,) and the dissipative part (ε'') of the electrical susceptibility χ of a two-level atom ($\varepsilon''_{max} = \chi_0/\gamma$) vs the detuning from the resonance (ω_0). The same spectral dependence is found for the linear oscillator model ($\varepsilon''_{max} = \omega_{pl}^2/[2\omega_0\gamma]$). Thin lines show the effect of power broadening at $I = I_s$; the FWHM increases by $\sqrt{2}$.

In the presence of a stronger resonant field however, the occupation probability of the two states begins to oscillate with the frequency $\sqrt{\Delta\omega^2+\omega_R^2}$ (ω_R is the Rabi frequency). This coherent effect is called optical- or AC-Stark effect. At resonance ($\Delta\omega=0$), it leads to a splitting of the energy states by $\pm\hbar\omega_R/2$, proportional to the field strength E_ω. Experimentally, the splitting is generally not observed, because it is comparable to the lifetime broadening of the states. The above intensity dependent inversion $\Delta N(I)$ is obtained by averaging the time-dependent quantum-mechanical population probabilities over an ensemble with exponential lifetime distribution ($p(t) \propto \gamma\ e^{-\gamma t}$). The frequency dependence of the resulting susceptibility is still Lorentzian, but the width increases with the intensity I, which is called "power broadening". More general results (including polarization relaxation) can be obtained by using the dressed atom picture, or by solving the Maxwell-Bloch equations of motion for the density matrix of the two states[30].

This model is very appropriate for resonant atomic nonlinearities such as sodium vapor, where optical bistability has first been observed[7]. More complicated models are needed to accurately describe the nonlinearities in semiconductor crystals. Still, this simple model describes a resonant nonlinearity due to saturation effects of (incoherent) carrier populations similar to the nonlinear carrier density effects in semiconductors. It has therefore been used in phenomenological two-level saturation models like in Eq. 2-28, where the amplitude χ_0, the saturation intensity I_S and the decay rate γ are used as phenomenological fitting parameters. Furthermore, it gives some indications on the frequency dependence of the linear and nonlinear susceptibility. At a large atomic detuning ($\Delta\omega \gg \gamma$), the real and the imaginary part of $\chi(\omega)$, which describe the resonant refraction and absorption fall of as $\Delta\omega^{-1}$ and $\Delta\omega^{-2}$, respectively. Similarly, the derivative $\partial\chi(\omega)/\partial I$ at $I = 0$ predicts a decrease proportional to $\Delta\omega^{-3}$ and $\Delta\omega^{-4}$ for the nonlinear refraction (Kerr coefficient n_2 in Eq. 2-21) and nonlinear absorption terms, respectively.

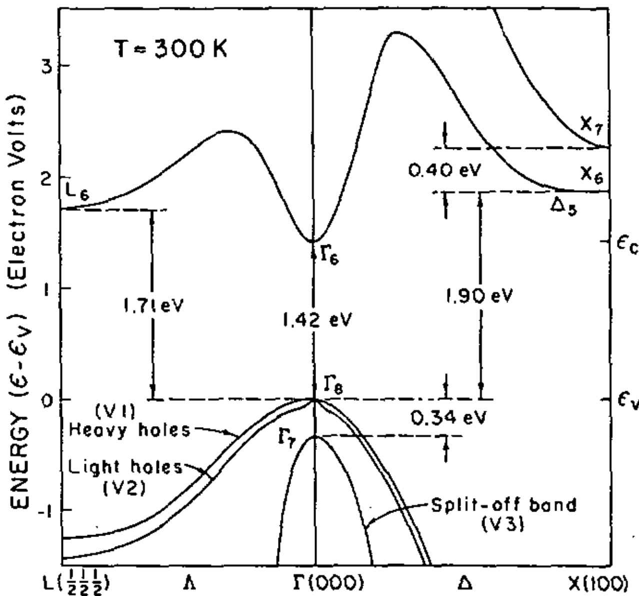

Fig. 2.13: Band structure of GaAs as a function of the reduced wave vector[31].

2.2.2 Semiconductor material (GaAs)

The potential for more compact switching devices based on direct gap semiconductor materials, where the large, abrupt absorption edge promises short interaction lengths and large resonant nonlinearities, has been recognized early and lead to observation of refractive optical bistability in ZnS[10] and GaAs[12].

Bandgap

In direct gap semiconductors, the minimum of the conduction band and the maximum of the valence band are separated by a vertical ($\Delta k = 0$) energy gap which thus couples to optical fields resonantly. Figure 2.13 shows the band structure[31] of the III–V semiconductor gallium-arsenide (GaAs). At room-temperature the gap is in the near infrared ($\lambda_g = 871$ nm)[32]

$$E_g = 1.424\ \mathrm{eV}\,, \qquad \frac{\partial E_g}{\partial T} = 0.40\ \frac{\mathrm{meV}}{\mathrm{K}}\,. \tag{2-42}$$

The linear absorption spectrum of GaAs is dominated by direct band to band transitions, proportional to the available densities of states. An important additional contribution comes from attractive Coulomb forces between carriers. At low temperatures they lead to excitonic resonances. However, at room-temperature in bulk GaAs these hydrogen-like bound states ($E_b = -4.2$ meV) of electrons and holes are mostly ionized. Still, the Coulomb interaction between continuum states has a strong impact on the absorption spectrum close to the gap (cf Fig. 2.16), summarized as Coulomb enhancement.

Most important for NLFP devices is the off-resonant region of low absorption. This bandtail can be approximated by an exponential decrease for $\hbar\omega < E_g$, with empirical parameters α_g and δE_g

$$\alpha(\hbar\omega) \approx \alpha_g \exp\left(\frac{\hbar\omega - E_g}{\delta E_g}\right); \tag{2-43}$$

$$\alpha_g \approx 10^4\ \mathrm{cm}^{-1}\,, \qquad \delta E_g \approx 6\ \mathrm{meV}\,.$$

The dispersion of the linear refractive index of GaAs[33] is shown in Fig. 2.14. Over a broad region around (below) the bandgap, the normal dispersion can be approximated by an average value $E/n\ \partial n/\partial E \approx 0.2$ which indicates an average group velocity ($d\omega(k)/dk$) of 0.8 times the phase velocity ($\omega(k)/k=c$). Near the bandgap of pure materials however, the refractive index exhibits a cusp of typically $\Delta n \approx 0.05$ height which leads to strong dispersive effects below the bandgap (cf. Sect. 3.3.3). Changes of this resonant feature due to optically generated carriers (cf Fig. 2.16) are used in the NLFP device.

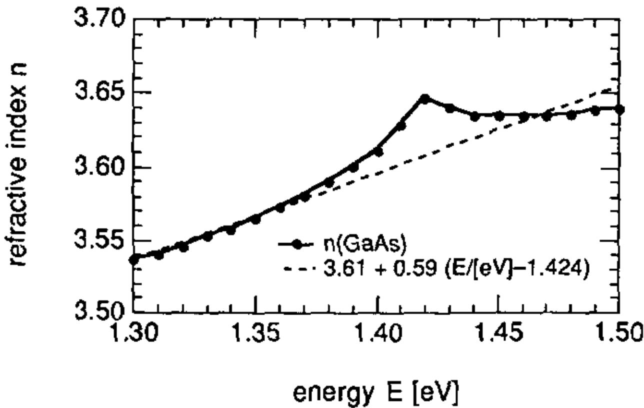

Fig. 2.14 *Refractive index of GaAs versus energy, in the vicinity of the bandgap* $E_g = 1.425$ *eV.*

AlGaAs alloy

Due to the excellent lattice matching (cf X-ray diffraction, Sect. 3.1.1) of GaAs and aluminium-arsenide (AlAs), alloys of $Al_xGa_{1-x}As$ with arbitrary Al-mole fractions x can be grown epitaxially on top of each other. This property is one of the foundations for the present integrated devices, where distinct dielectric properties of active layers and dielectric mirrors are obtained by varying the composition x during growth (Fig. 2.15). The following approximations have been used to estimate the bandgap energy[34] at 300 K (direct up to $x \leq 0.45$), and the refractive index[35] as a function of the aluminium concentration x:

$$E_g(x) = 1.423 + 1.36x + 0.22x^2 \text{ [eV]}, \tag{2-44}$$

$$n^2(x,\omega) = n^2_{GaAs}(\omega) + x\,[n^2_{GaAs}(\omega) - n^2_{AlAs}(\omega)].$$

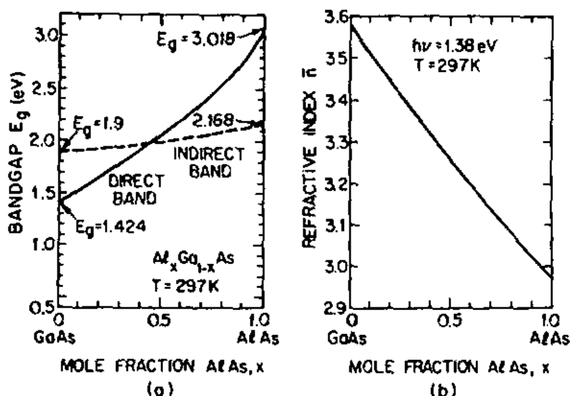

Fig. 2.15: Compositional dependence of the $Al_xGa_{1-x}As$ energy gap (a), and the refractive index at 1.38 eV.[32]

Resonant nonlinearities

If electron-hole pairs are generated by optical absorption, the carriers in the two bands thermalize within ps to quasi-thermal momentum and energy distributions. Due to these fast intraband relaxation mechanisms which are mediated by carrier collision and phonon interaction, coherent processes like Rabi oscillations (cf Sect. 2.2.1) can be observed only with ultrashort pulses. The resonant nonlinearities of interest are thus due to incoherent many-body effects which depend on the quasi-thermal density N of electron-hole pairs. There are three principal effects which determine the carrier induced nonlinearity of GaAs:

Band-filling due to the Pauli exclusion principle leads to a broadening and a blue shift of the absorption edge. It is the main contribution at large carrier densities. An opposite effect arises from the screening of the crystal potential by the excited carrier plasma. This is known as bandgap renormalization and causes a red-shift of the absorption spectrum. Saturation effects related to the screening and the ionization of excitons (at the Mott density of about 10^{17} cm^{-3}), which are the dominant contribution in low dimensional and large gap semiconductors, are less important in bulk GaAs.

Quantitative theories for the nonlinear optical properties of direct gap semiconductors have been elaborated only in the last decade, in close collaboration with experimentalists. Compared to the phenomenological two-level model (Eq. 2-41), they account for the bandstructure and the above mentioned many-body effects. Accurate results are obtained from a numerical matrix-inversion method[36],

proposed by Löwenau, Schmitt-Rink and Haug in 1982, which allows the direct calculation of the frequency and carrier-dependent susceptibility. An approximation of this model, the so-called plasma theory[37] suggested by Banyai and Koch, yields analytical expression for the density-dependent absorption spectrum $\alpha(\omega,N)$ of bulk GaAs at low excitation, and is therefore widely used to simulate nonlinear devices[38].

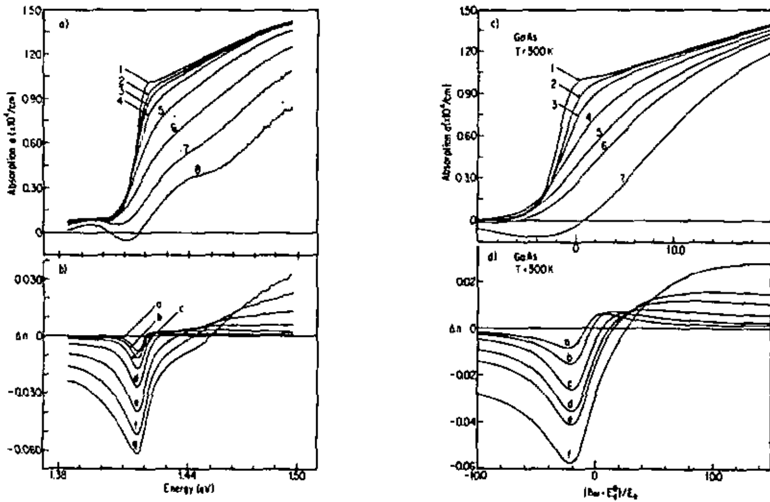

Fig. 2.16: Comparison of experimental (left) and theoretical (right) optical nonlinearities of bulk GaAs at room-temperature [39]*:*
a) curves 1–8 show the absorption measured at 0, 0.2, 0.5, 1.3, 3.2, 8, 20, 50 mW power on a 15 μm spot size,
c) curves 1–7 show the absorption calculated (plasma theory) at pair densities N = 0.001, 0.08, 0.2, 0.5, 0.8, 1.0, and $1.5 \cdot 10^{18}$ cm^{-3}.
b) and d) are the refractive index changes corresponding to a) and c), respectively, obtained by a Kramers-Kronig transform.

Lee et al. published measurements[39] which compare well with the plasma theory (Fig. 2.16). Their absorption spectra $\alpha(\omega,I)$ stem from pump and probe measurements of a GaAs sample, where carriers were created with pump pulses of variable intensity at 1.51 eV and the transmission of a broad-band probe was detected with an optical multichannel analyzer. The corresponding refractive index changes $\Delta n(\omega,N)$ and $\Delta n(\omega,I)$ were derived by numerical Kramers-Kronig transformation for both cases. Of special interest for the optimization of devices (cf Sect. 2.6) is the region below the gap energy, where large index changes

coexist with reduced absorption. A peak change $\Delta n \approx -0.05$ is found at a carrier density close to 10^{18} cm^{-3} about 10 meV below the initial bandgap.

Bulk material vs multiple quantum well

Modern epitaxial growth techniques allow the growth of multiple-quantum well heterostructures (MQW), where the electrons are confined to wells of typically 100 Å width. This one-dimensional confinement enhances the excitonic features at room-temperature.

Initially, the observation of room-temperature optical bistability was attributed to exciton saturation[40], which encouraged the use of MQW material. Recent results[41] however, indicate that bistability even in MQW samples relies on nonlinear effects related to the continuum states, because the large excitonic features saturate below the critical intensities. The reported nonlinear cross-section $\eta = 8 \cdot 10^{-20}$ cm^3, together with an assumed absorption of 1000 cm^{-1}, indicates a critical carrier density of $N^c = 2 \cdot 10^{-17}$ cm^{-3} (Eq. 2-25), which is larger than the Mott density. An independent confirmation comes from the thresholds measured for the present NLFP with bulk GaAs spacers (cf Sect. 3.5.3) which compare favorably to thresholds reported for NLFP with similar finesse which use MQW spacers[42].

Saturation effects

The index change related to the continuum states tends to saturate also, but the corresponding intensities are at least an order of magnitude higher than for excitonic nonlinearities[43]. The maximum index changes observed on NLFP with MQW[42] and bulk GaAs spacers (cf Fig. 3.14) are $|\Delta n| \leq 0.010$ and 0.025, respectively, at carrier densities of about 10^{18} cm^{-3}, using single wavelength measurements, as opposed to the pump and probe measurements mentioned above.

Unlike the excitonic nonlinearity, the many-body effects do not saturate as a function of carrier density (at densities of 10^{18} cm^{-3}). The observed saturation is rather due to indirect mechanisms related to the optical carrier generation, such as changes in absorption, recombination rate and temperature.

For single wavelength measurements, band filling reduces the absorption coefficient and therefore the number of generated carriers. Stimulated emission and density dependent processes like bimolecular and Auger recombination reduce the carrier life time τ at high excitation[44]. Strong pumping may lead to a temperature rise in the absorbing layer, and cause a positive refractive index change opposed to the electronic effect.

2.2.3 Carrier rate equation

The relation between the optical intensity I and the ambipolar carrier density N in the semiconductor can be described by a simple carrier rate equation[45]

$$\frac{dN}{dt} = \frac{\alpha(\omega,N)\,I}{\hbar\omega} - \frac{N-N_{th}}{\tau} - \nabla(\mathcal{D}\nabla N)\,. \qquad (2\text{-}45)$$

At thermal equilibrium, the density of electron-hole pairs is $N = N_{th}$. Additional carriers are generated by absorption of the power density αI (photon energy $\hbar\omega$). Two loss terms account for carrier recombination and diffusion which are characterized by the carrier recombination time τ and the ambipolar diffusivity $\mathcal{D}$, respectively. Some assumptions and implications of this phenomenological model are discussed below (for a review on models cf ref. [46]):

Time scale

The time scale is given by the interband carrier recombination time τ which is typically a few ns. Inside the conduction and valence band the optically created electron and hole distributions thermalize within ps. Thus, one can adiabatically eliminate this fast intraband relaxation and assume an electron-hole pair density with quasi-thermal polarization and energy distributions of the carriers.

In passive devices the stimulated emission is small compared to spontaneous emission and nonradiative recombination processes. Under normal conditions in GaAs, a constant bulk recombination term τ_b dominates. Other contributions come from density dependent processes[47] like bimolecular ($\mathcal{B}$) and Auger recombination ($\mathcal{A}$)[35] and surface recombination[48] ($\mathcal{S}$) becomes important for thin layers (thickness L)

$$\frac{1}{\tau} = \frac{1}{\tau_b} + \frac{2\mathcal{S}}{L} + \mathcal{B}N + \mathcal{A}N^2\,. \qquad (2\text{-}46)$$

One is often interested in steady state properties, like threshold intensities, rather than in the dynamics of the model. The steady state approximation $\partial N/\partial t = 0$ is valid for times which are long compared to the recombination time τ. In the simplest approximation of constant $\tau \approx \tau_b$ one expects a quasi-equilibrium carrier density N_s proportional to the intensity I and to the material parameters τ and α.

Switching energy

If one considers pulses shorter than τ, the effects of carrier recombination and diffusion can be neglected in Eq. 2-45. Assuming a high finesse cavity (Eq. 2-18) and a constant nonlinear cross-section η (Eq. 2-19), the nonlinear phase change created by the cavity intensity $I(\varphi)$, or by the incident intensity I_i, is

$$\frac{d\varphi}{dt} = Lk\eta \frac{dN}{dt} = \frac{I(\varphi)}{\iota\tau\sqrt{F}} = \frac{I_i}{\iota\tau} T_{FP}(\varphi) ; \qquad \iota\tau = \frac{\hbar c}{\eta} . \qquad (2\text{-}47)$$

From the finite carrier density change ΔN (or the corresponding phase change $\Delta\varphi = \varphi_2 - \varphi_1$) involved in a bistable switching transition (Fig. 2.7) one can then calculate the total energies per unit surface which are absorbed (e_a), respectively incident (e_i), during the switching process (for $t_2 - t_1 \leq \tau$)

$$e_a = \int_{t_1}^{t_2} dt\, I(\varphi)\alpha L = \int_{\varphi_1}^{\varphi_2} \frac{d\varphi}{\dot{\varphi}} \frac{I(\varphi)}{\sqrt{F}} = \iota\tau(\varphi_2 - \varphi_1) , \qquad (2\text{-}48)$$

$$e_i = \int_{t_1}^{t_2} dt\, I_i = \int_{\varphi_1}^{\varphi_2} \frac{d\varphi}{\dot{\varphi}} I_i = \iota\tau(\varphi_2 - \varphi_1)\left[1 + \frac{F}{3}(\varphi_2^2 + \varphi_2\varphi_1 + \varphi_1^2)\right].$$

Thus, for short pulses, the switching energy is determined by the finite phase interval $\varphi_2 - \varphi_1$; it is independent of pulse duration. The expression in square brackets gives the relation between the total energy dissipated (e_i) an the energy absorbed in the spacer (e_a). For instance, to reach the critical switching point φ^c from φ_0^c (Eq. 2-23), the energy $e_a^c = \iota\tau\, 2/\sqrt{3F}$ is absorbed, compared to $e_i^c = 22/9\, e_a^c$ incident (per surface). For a typical bistable transition, assuming $\varphi_1 \approx 2/\sqrt{F}$ and $\varphi_2 \approx 0$ indicates $e_a \approx \iota\tau\, 2/\sqrt{F}$ and a ratio of $e_i/e_a \approx 7/3$.

Critical slowing down

Indeed, this switching energy requirement is not restricted to short pulses. The following dynamic considerations indicate, that it remains valid (at least for the switching increment), for times much larger than the carrier relaxation time τ.

The intensity inside the cavity $I(I_i,\varphi)$ depends nonlinearly on the incident intensity I_i. Using again the high finesse approximation (Eq. 2-18), neglecting diffusion (plane wave excitation) and the thermal density N_{th} (« N), the carrier rate equation (Eq. 2-45) can be rewritten with normalized variables

$$\frac{d\tilde{N}}{dt} = -\frac{\tilde{N}}{\tau} + \frac{\tilde{I}_i}{1 + (\tilde{\varphi}_0 - \tilde{N})^2}; \qquad (2\text{-}49)$$

$$\tilde{N} \equiv \sqrt{F}kL\eta\, N, \qquad \tilde{I}_i \equiv \sqrt{F}\,\frac{I_i}{\iota\tau}, \qquad \tilde{\varphi}_0 \equiv \sqrt{F}\,\varphi_0 .$$

The carrier density is expressed by the corresponding (proportional) nonlinear phase shift $\tilde{N} = \Delta\varphi(N)$. For a given incident intensity $\tilde{I}_i$ and initial detuning $\tilde{\varphi}_0$ there are (one or three) stationary densities $\tilde{N}_s$, corresponding to intersections in Fig. 2.7, which satisfy

$$\tilde{I}_i = \tilde{N}_s\,[1 + (\tilde{\varphi}_0 - \tilde{N}_s)^2]/\tau . \qquad (2\text{-}50)$$

The linearized differential equation for a perturbation $\Delta\tilde{N}(\Delta\tilde{I}_i)$ of the stationary state $\tilde{N}_s$ can be written similar to Eq. 2-49, but with a new damping constant $\hat{\tau}$

$$\frac{d\Delta\tilde{N}}{dt} = -\frac{\Delta\tilde{N}}{\hat{\tau}} + \frac{\Delta\tilde{I}_i}{1 + (\tilde{\varphi}_0 - \tilde{N}_s)^2}; \qquad (2\text{-}51)$$

$$\hat{\tau} \equiv \tau\,\frac{1 + (\tilde{\varphi}_0 - \tilde{N}_s)^2}{1 + (\tilde{\varphi}_0 - \tilde{N}_s)(\tilde{\varphi}_0 - 3\tilde{N}_s)},$$

which depends on the phase $\tilde{\varphi}_0 - \tilde{N}_s$ of the stationary state only. $\hat{\tau}$ diverges at the critical transition points and becomes negative in the (unstable) transition region.

If the constant intensity perturbation $\Delta\tilde{I}_i$ does not exceed the critical switching point, the phase will, after $\Delta t > \hat{\tau}$, tend towards a new stationary state $\tilde{N}_s + \Delta\tilde{N}_s$

$$\frac{\Delta\tilde{N}_s}{\tilde{N}_s} = \frac{\Delta\tilde{I}_i\,\hat{\tau}}{\tilde{I}_i\,\tau} . \qquad (2\text{-}52)$$

Thus, the relative carrier density change $\Delta\tilde{N}_s$ is proportional to the incident perturbation energy $\Delta\tilde{I}_i \cdot \hat{\tau}$. Close to a critical point ($\tilde{N}_s \geq 2/\sqrt{3}$) $\hat{\tau}$ diverges, and $\Delta\tilde{N}_s$ may become large even for small perturbations $\Delta\tilde{I}_i$. This switching energy conservation corresponds to the pulse area scaling law which has been derived[49] more generally for optical bistability.

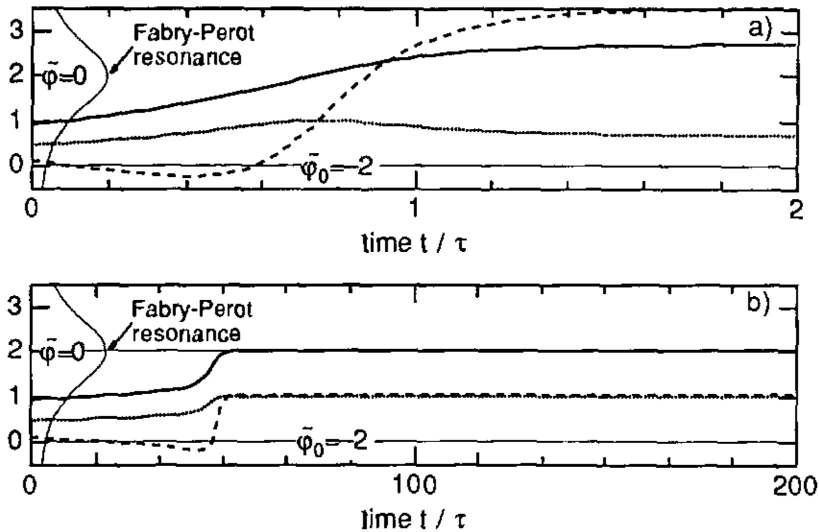

Fig. 2.17 *Bistable transition, following an abrupt increase of the incident intensity at t=0 from the stationary state $\tilde{\varphi}_0=-2$, $\tilde{I}_i=2$, $\tilde{N}_s=0.9$: The evolution of the normalized carrier density $\tilde{N}$ (solid line), of the relative cavity intensity $I/I_i\sqrt{F}$ (dotted) and of the inverse damping constant $\tilde{\tau}/\tau$ (dashed) are shown for a) $\Delta\tilde{I}_i=2$, and b) $\Delta\tilde{I}_i=0.02$.*

Numerically integrated solutions of Eq. 2-47 show that a similar time-power tradeoff is valid not only close to a critical point, but throughout the unstable transition region. Fig. 2.17 shows the dynamic response of a stationary system to a sudden increase of incident intensity above threshold. The evolution of the normalized carrier density $\tilde{N}$, of the relative cavity intensity $I/[I_i\sqrt{F}]$ and of the inverse damping constant $(\tilde{\tau}/\tau)^{-1}$ are shown. Although the increment $\Delta\tilde{I}_i$ differs by two orders of magnitude in the two simulations the dynamic evolution is similar, and the product of transition time and increment $\Delta\tilde{I}_i$ is about constant.

Therefore, in a NLFP the energy of the switching pulse $\Delta e_i=\int\Delta I_i\cdot dt$ (and Δe_a), but not the total energy $e_i=\int(I_i+\Delta I_i)\cdot dt$ (and e_a), is independent of the switching intensity increment. Small increments ΔI_i are possible at the expense of increasing transition times much longer than the carrier relaxation time τ. This behavior is a consequence of critical slowing down[50] at phase transitions; its experimental observation on bistable NLFP will be described in Section 3.5.4.

Carrier diffusion effects

Diffusion effects are associated to spatial variations of the carrier density N(**x**). Their size is governed by the ambipolar diffusivity $\mathcal{D}$ (= $2\mathcal{D}_p\mathcal{D}_n/[\mathcal{D}_p+\mathcal{D}_n]$) which is related to the mobilities of holes and electrons by the Einstein relation ($\mathcal{D}_x = \mu_x kT/e$). For simplicity, the weak dependence of $\mathcal{D}$ on the carrier density N is ignored here, and a constant $\mathcal{D} \approx 13\ \mathrm{cm}^{-1}$ (corresponding to $N \approx 10^{17}\ \mathrm{cm}^{-3}$) is assumed. On short time scales ($\Delta t \ll \tau$), the effect of carrier diffusion can be neglected. For time intervals Δt larger than the relaxation time τ, the carriers move an average length $L_D = \sqrt{\mathcal{D}\tau} \approx 3\ \mu\mathrm{m}$ before they recombine. From the geometry of integrated nonlinear Fabry-Perot devices, one can distinguish longitudinal and the lateral (transverse) effects.

Close to a Fabry-Perot resonance, the counterpropagating waves create a standing wave pattern in the spacer. The period of this longitudinal intensity variation $\lambda/2n \approx 120$ nm ($\lambda g = 870$ nm, $n_{GaAs} \approx 3.6$) is much smaller than the diffusion length L_D. Therefore, on the time scale imposed by the carrier relaxation time τ, standing wave effects in the carrier density are washed out by diffusion. However, they may play a role in the case of a fast switching ON transition induced by a large incident pulse.

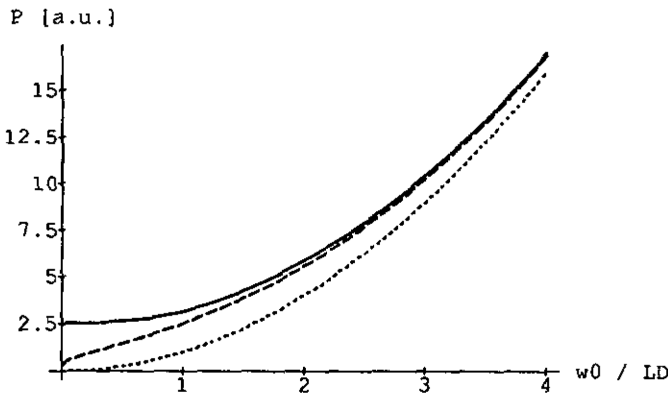

Fig. 2.18: Influence of transverse carrier diffusion: The power which is required to generate a given carrier density N^c at the spot center (dashed line), or as an average in an area πL_D^2 determined by the diffusion length L_D (solid line) is plotted as a function of the relative spotsize w_0/L_D (assuming constant intensity in a spot of radius w_0). For comparison, the dotted line shows the case without diffusion.

The *transverse diffusion* vanishes in the limit of plane wave excitation (cf numerical tool described in Section 2.3.2). In the experiment however, the incident intensity is limited to a finite spot which is typically described by a Gaussian intensity dependence $I(r) \propto \exp(-2[r/w_0]^2)$, where w_0 is the beam waist. Transverse diffusion becomes increasingly important as the spot size approaches the diffusion length L_D. Assuming a constant intensity within a circular spot, the carrier density can be described analytically by Bessel functions: Fig. 2.18 shows the power required to generate a critical carrier density N^c (Eq. 2-25) at the spot center, or as an average in a spot of radius L_D, for different ratios w_0/L_D. For a small beam waist w_0 the power levels are increased considerably compared to the case without diffusion. This indicates that the minimal threshold power in a NLFP the is determined by the diffusivity $\mathcal{D}$ (Interestingly, this minimal power seems independent of the recombination time τ, as the dependence of intensity $I^c \propto N^c / \tau^{-1}$ and spotsize $L_D^2 \propto \mathcal{D}\tau$ cancel). Similar results are obtained with analytical diffusion models[51,52] which assume Gaussian beams and include diffraction effects (cf Sect. 4.1.3).

If the spotsize is large compared to the diffusion length, the influence of transverse diffusion on the threshold is small. However, it has been shown that in this case a switching wave effect reduces the width of the expected hysteresis loops[53]. Another effect of carrier diffusion is transverse crosstalk between neighboring devices[54]. Corresponding studies[55] have estimated that a separation of at least 3 diffusion lengths between elements in a linear array is required to guarantee their independent operation. If the device is operated with a holding beam close to a critical transition point, this minimum separation increases further, because of the critical slowing down effect. A method to reduce this crosstalk is pixellation[56], which may reduce thresholds, if it is possible to keep the surface recombination small.

Diffraction effects

The present rate equation does not explicitly account for diffraction effects, but implicitly assumes intensity distributions which satisfy diffraction. The numerical simulation model which has been developed (cf Sect 2.3.2) is based on plane wave illumination and is therefore appropriate for large spots only. (The influence of a limited spotsize on the linear properties can, however, be studied by superposing calculations for oblique angles of incidence).

As mentioned above, transverse effects in NLFP devices have been studied with several analytical and numerical methods[51,52,57]. These models lead to consistent intensity and carrier (and temperature[38]) distributions in a cylindrical geometry.

The common, principal result is that for a small spotsize the critical detuning and the switching intensities increase[58]. This may lead to a loss of bistability[59,52] if the detuning is kept constant. The increase of the critical detuning, and therefore of the threshold power, is due increasing diffraction losses which reduce the cavity finesse. In a FP diffraction losses become dominant, when the Rayleigh length $z_0 = n\pi w_0^2/\lambda$ (Gaussian beam with waist w_0) approaches the effective cavity length FL (cf Eq. 4-10).

The influence of diffusion and of diffraction is apparent in spotsize dependent measurements of the switching threshold which are presented in Sect. 3.5.7. The impact of transverse effects on device performance is discussed in Section 4.1.3.

Temperature effects

Nonradiative recombination of excited carriers causes a temperature rise in the active volume. This reduces the bandgap energy (Eq. 2-42) and therefore strongly effects the optical properties. Assuming a rigid shift (Eq. 2-42) of the bandtail (Eq. 2-43) indicates an absorption change $\partial \ln(\alpha)/\partial T = 7\%\ K^{-1}$. The corresponding positive refractive index change (cf Fig. 2.14, measurements in Sect. 3.3.3) is used as the nonlinear effect in nonlinear interference filters[60] (NLIF) and bistable etalons with absorbed transmission[61] (BEAT). In nonlinear Fabry-Perot (NLFP) devices however, thermal effects are undesired, because they reduce the negative electronic index change. This competition is the cause of thermal instabilities such as regenerative switching[62]. It can also lead to a saturation of the nonlinear index shift (Sect. 3.4.2). Therefore, heating effects are minimized in the experiment by heat sinking and by pulsed operation with a low duty cycle. Modelling of heat effects involves the additional solution of a heat diffusion equation to obtain the temperature distribution. A realistic simulation for a typical monolithic NLFP device[63] predicts a temperature rise of 2–3 K just after switch-ON at an assumed threshold of 7 mW (3 μm spotsize). In view of parallel devices it is important to maximize the longitudinal contribution (through the mirrors) to the heat dissipation.

2.3 Integrated layered structures

A nonlinear Fabry-Perot (NLFP) is composed of two dielectric mirrors which enclose a nonlinear spacer layer. By varying the composition of the $Al_xGa_{1-x}As$ compound these functional parts can be integrated in a single multilayer stack. The control of thickness and composition offered by modern epitaxial technologies (MBE, MOCVD) allows the fabrication of integrated NLFP in one growth process. To design and optimize such nonlinear layered structures one has to know their optical properties.

This section introduces a rigorous matrix calculus[64,65] which describes the propagation of (inhomogeneous) harmonic plane waves in dissipative layered media. This is the basis of a numerical tool, which allows to calculate arbitrary nonlinear stacks by iterating a selfconsistent carrier rate equation in each layer.

2.3.1 Light propagation in planar dielectrics

The optical properties of Fabry-Perot resonators and Bragg reflectors arise from multiple beam interference phenomena in thin 2-dimensional layers. They can be studied by considering two counterpropagating waves which are coupled coherently by Fresnel refraction at the interfaces between adjacent layers, and by absorption in a dissipative layer.

Harmonic plane waves

The propagation of electromagnetic fields in homogeneous, isotropic media is described by the wave equation and the material parameters $\tilde{\varepsilon}$ and μ introduced in Section 2.2.1. In the presence of spectral dispersion and planar interfaces, complex harmonic plane waves are suitable solutions to the Helmholtz equation (Eq. 2-35)

$$\tilde{\mathbf{E}} = \tilde{\mathbf{E}}_0\, e^{i(\tilde{\mathbf{k}}\mathbf{x}-\omega t)} = -\tilde{Z}\,[\hat{\mathbf{n}}\wedge\tilde{\mathbf{H}}], \qquad (2\text{-}53)$$

$$\tilde{\mathbf{H}} = \frac{1}{\tilde{Z}}\,[\hat{\mathbf{n}}\wedge\tilde{\mathbf{E}}]\,.$$

The complex wave vector $\tilde{\mathbf{k}}$ describes the spatial dependence of the electrical and magnetic fields $\mathbf{E}(\mathbf{x},t) = \mathrm{Re}\{\tilde{\mathbf{E}}\}$ and $\mathbf{H}(\mathbf{x},t) = \mathrm{Re}\{\tilde{\mathbf{H}}\}$. The relative magnitude of the fields is given by the (complex) wave impedance $\tilde{Z}$. The parameters $\tilde{\mathbf{k}}$ and $\tilde{Z}$ are determined by the dielectric function $\tilde{\varepsilon}$ and the magnetic permeability μ:

$$\tilde{\mathbf{k}}\cdot\tilde{\mathbf{k}} - k^2\,\mu\tilde{\varepsilon} = 0\,; \qquad\qquad k = \frac{\omega}{c}\,, \tag{2-54}$$
$$\tilde{Z} = \sqrt{\frac{\mu}{\tilde{\varepsilon}}}\,Z_0\,.$$

The vacuum wave number k is defined by the frequency ω and the light velocity c. The relation between the magnetic and electric units (MKSA system) is given by the vacuum impedance Z_0

$$c \equiv \frac{1}{\sqrt{\varepsilon_0\mu_0}} \equiv 299\,792\,458\,\frac{\mathrm{m}}{\mathrm{s}}\,, \tag{2-55}$$
$$Z_0 \equiv c\mu_0 = c\cdot 4\pi\cdot 10^{-7}\,\frac{\mathrm{Vs}}{\mathrm{Am}} \approx 376.73\ \Omega\,.$$

The real and the imaginary part of the wave vector $\tilde{\mathbf{k}}$ determine the attenuation and the phase velocity of a wave. They are commonly expressed by the intensity absorption coefficient α and the refractive index n, respectively

$$\tilde{\mathbf{k}} = \left(n\,k + i\,\frac{\alpha}{2}\right)\hat{\mathbf{n}}\,, \tag{2-56}$$

where the unit vector $\hat{\mathbf{n}}$ (satisfying $\hat{\mathbf{n}}\cdot\hat{\mathbf{n}} = 1$) specifies the direction of propagation. From Eqs. 2-54 and 2-56 follow the relations $n(\tilde{\varepsilon})$ and $\alpha(\tilde{\varepsilon})$ given in Eq. 2-38.

Laws of Descartes and Snell

Consider one plane wave with wave vector $\tilde{\mathbf{k}}^+$ incident on a plane layered structure, oriented perpendicular to the $\hat{\mathbf{z}}$ direction. Momentum conservation at an interface demands the continuity of the tangential components of the reflected and the transmitted wave vectors $\tilde{\mathbf{k}}^-$ and $\tilde{\mathbf{k}}'^+$, respectively

$$\tilde{\mathbf{k}}^-\wedge\hat{\mathbf{z}} = \tilde{\mathbf{k}}^+\wedge\hat{\mathbf{z}}\,, \qquad\qquad \tilde{\mathbf{k}}'^+\wedge\hat{\mathbf{z}} = \tilde{\mathbf{k}}^+\wedge\hat{\mathbf{z}}\,. \tag{2-57}$$

Because these tangential components are constant throughout the stack, the perpendicular components $\tilde{\beta}$ of the forward and a backward waves in different layers are related by Eq. 2-54

$$\tilde{\beta} \equiv \tilde{\mathbf{k}}^+\cdot\hat{\mathbf{z}} = \tilde{k}^+_z = -\,\tilde{k}^-_z\,, \tag{2-58}$$
$$\tilde{\beta}' = \sqrt{\mu k^2(\tilde{\varepsilon}' - \tilde{\varepsilon}) + \tilde{\beta}^2}\,.$$

Fresnel laws

Due to the orthogonality condition Eq. 2-53, the field can be decomposed into a transverse electric field $\tilde{E}_{TE}$ and a transverse magnetic field $\tilde{H}_{TM}$. Because these two polarizations are orthogonal, they do not interfere throughout the stack and can be calculated independently

$$\tilde{E}_0 = \tilde{E}_{TE}\,\hat{q}_1 - \tilde{Z}\,\tilde{H}_{TM}\,\hat{q}_2 ; \tag{2-59}$$

$$\hat{q}_1 \equiv \frac{\hat{z}\wedge\hat{n}}{\sqrt{(\hat{z}\wedge\hat{n})^2}}, \qquad \hat{q}_2 \equiv \hat{n}\wedge\hat{q}_1 .$$

The relationships between incident, reflected and transmitted field amplitudes originate from continuity conditions for the fields. The Fresnel reflection and transmission coefficients for $\tilde{E}_{TE}$ and $\tilde{H}_{TM}$ amplitudes are formally equal, when $\hat{\beta}$ is replaced by $\tilde{\beta}/\mu$ and $\tilde{\beta}/\tilde{\varepsilon}$, respectively

$$\tilde{r}^+ = \frac{\hat{\beta} - \hat{\beta}'}{\hat{\beta} + \hat{\beta}'}, \qquad \tilde{r}^- = -\tilde{r}^+, \tag{2-60}$$

$$\tilde{t}^+ = \frac{2\,\hat{\beta}}{\hat{\beta} + \hat{\beta}'}, \qquad \tilde{t}^- = \frac{\hat{\beta}'}{\hat{\beta}}\,\tilde{t}^+ .$$

The coefficients $\tilde{r}^-$ and $\tilde{t}'^-$ for the backward direction follow from symmetry arguments.

Matrix calculus

The evolution of the two counterpropagating waves through one layer can thus be described by a four-pole[64] (Fig. 2.19).

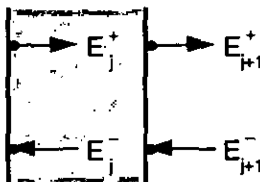

Fig. 2.19: Four-pole representation of the fields in adjacent layers.

The four-pole is determined by the product of two matrices, the first describing the field propagation through a layer j of width d_j, according to Eq. 2-53

$$\mathbb{P}_j = \begin{bmatrix} e^{i\tilde{\beta}_j d_j} & 0 \\ 0 & e^{-i\tilde{\beta}_j d_j} \end{bmatrix}, \tag{2-61}$$

and the second describing the (polarization dependent) coupling at interface j, j+1 by the Fresnel formulae (Eq. 2-60)

$$\mathbb{F}_j = \frac{1}{\tilde{t}_j^-} \begin{bmatrix} 1 & \tilde{r}_j^- \\ \tilde{r}_j^- & 1 \end{bmatrix}. \tag{2-62}$$

An arbitrary stack of m dielectric layers can be calculated for each polarization by successive multiplication of corresponding matrix-pairs.

$$\begin{pmatrix} \tilde{E}^+_{TE;m} \\ \tilde{E}^-_{TE;m} \end{pmatrix} = \mathbb{M}_m^{TE} \begin{pmatrix} \tilde{E}^+_{TE;0} \\ \tilde{E}^-_{TE;0} \end{pmatrix}; \qquad \mathbb{M}_m^{TE} \equiv \prod_{j=0}^{m} \mathbb{F}_j^{TE} \mathbb{P}_j, \tag{2-63}$$
$$\begin{pmatrix} \tilde{H}^+_{TM;m} \\ \tilde{H}^-_{TM;m} \end{pmatrix} = \mathbb{M}_m^{TM} \begin{pmatrix} \tilde{H}^+_{TM;0} \\ \tilde{H}^-_{TM;0} \end{pmatrix}; \qquad \mathbb{M}_m^{TM} \equiv \prod_{j=0}^{m} \mathbb{F}_j^{TM} \mathbb{P}_j.$$

Properties of the stack, like reflection and transmission coefficients, are then evaluated from appropriate boundary conditions.

Inhomogeneous plane waves

For so-called harmonic inhomogeneous plane waves (HIPW) the amplitude and phase gradients are not parallel. These waves can be described by a wave vector $\mathbf{k} = k\sqrt{\mu\tilde{\varepsilon}}\,\hat{\mathbf{n}}$ with a complex unit propagation vector $\hat{\mathbf{n}}$ (with $\hat{\mathbf{n}}\cdot\hat{\mathbf{n}} = 1$, but $|\hat{\mathbf{n}}|^2 \neq 1$)

$$\hat{\mathbf{n}} = \cosh\varsigma\, \hat{\mathbf{n}}_{\parallel} + i \sinh\varsigma\, \hat{\mathbf{n}}_{\perp}, \tag{2-64}$$

which is given by an inhomogeneity parameter ς and two perpendicular real unit vectors $\hat{\mathbf{n}}_{\parallel}\cdot\hat{\mathbf{n}}_{\perp} = 0$. Then, the above relationships remain valid. This formalism for HIPW[66,67] has been included in the simulation tool NLB (cf Sect. 2.3.2).

Poynting vector and dissipation

The intensity or time averaged energy flux I(x,t) of a harmonic wave can be expressed in terms of a complex Poynting vector $\tilde{S}$

$$I(x,t) = \int_0^{2\pi/\omega} dt\, Re\{\tilde{E}\} \wedge Re\{\tilde{H}\} = Re\{\tilde{S}\}\,, \tag{2-65}$$

$$\tilde{S} \equiv \frac{1}{2}\, \tilde{E} \wedge \tilde{H}^* = \frac{1}{2}\, (\tilde{E}_0 \wedge \tilde{H}_0^*)\, e^{-i(\tilde{k}-\tilde{k}^*)x}\,.$$

According to the local energy conservation which follows from Maxwell's equations, the dissipated power density is

$$Re\{\nabla\tilde{S}\} = -\frac{\sigma}{2}\, |\tilde{E}|^2 = -\frac{n\,\alpha}{2\mu Z_0}\, |\tilde{E}_0|^2\, e^{2Im\{\tilde{k}\}x}\,. \tag{2-66}$$

Here, the electric field $\tilde{E}_0$ *is the coherent sum the two polarizations* $\tilde{E}_{TE}\,\hat{q}_1$ *and* $\tilde{E}_{TM}\,\hat{q}_2$ which only interfere for inhomogeneous waves ($\varsigma \neq 0$ in Eq. 2-64).

If the dissipation is calculated in an absorbing layer with forward and backward propagating fields $\tilde{E}^+$ and $\tilde{E}^-$, there is one such term for each propagation direction $\tilde{k}^+$ and $\tilde{k}^-$, as well as a mixed term which describes standing wave interferences along the $\hat{z}$ direction ($\tilde{k}_z^+ = -\tilde{k}_z^- = \tilde{\beta}$).

2.3.2 Nonlinear simulation tool: NLB

A numerical tool named NLB has been implemented on VAX-FORTRAN to simulate the frequency and intensity dependent response of arbitrary nonlinear dielectric stacks to polarized fields incident at any angle. The linear wave propagation is based on the above matrix calculus. A carrier rate equation is iterated selfconsistently in each nonlinear layer to determine the intensity dependent nonlinear properties.

Band matrix

Rather than to evaluate the product matrix which corresponds to a stack with m layers (Eq. 2-63), the relations between the fields can be described by a 2m+2-dimensional band matrix which essentially contains the individual matrices $\mathbb{P}_j\mathbb{F}_j$ of the dielectric layers. This approach has the advantage that the fields in each layer

are available, as the components of a 2m+2-dimensional vector, to determine the intensity and associated nonlinear properties.

Rate equation

In a nonlinear layer j, an intensity dependent carrier density N_j is determined by applying the steady state rate equation (Eq. 2-45) to a longitudinal average[68] of the absorbed intensity $\alpha_j I_j$ described in Eq. 2-66

$$N_j = \frac{\tau}{\hbar\omega}\alpha_j I_j + N_{th}\,, \tag{2-67}$$

$$\alpha_j I_j \equiv -\frac{1}{d_j}\int_0^{d_j} dz\, \mathrm{Re}\{\nabla\tilde{S}\} = \frac{\alpha_j n_j}{2\mu Z_0}\frac{1}{d_j}\int_0^{d_j} dz\, |\tilde{E}_{(j)}|^2 .$$

The total complex field $\tilde{E}_{(j)}$ (Eq. 2-53) in layer j encompasses two polarizations and two propagation directions. The longitudinal average respects their phase dependent coherent superposition, but neglects longitudinal intensity variations (standing waves) within a layer. This is justified physically because carrier density fluctuations are washed out by diffusion. (Standing wave effects can nevertheless be studied by dividing a layer into sublayers which are thin compared to the period of the standing wave $d_j \leq \lambda/2n$.)

The carrier densities N_j yield the nonlinear changes of refraction and absorption coefficients $\Delta n_j(N_j)$ and $\alpha_j(N_j)$. These, through the propagation constant $\tilde{\beta}_j$, change the band matrix. Therefore, this process is iterated with the modified band matrix until a selfconsistent field and carrier distribution throughout the stack is reached.

Material properties

In the present model, the frequency and density dependent material parameters $\alpha(\omega,N)$ and $\Delta n(\omega,N)$ are interpolated from the experimental data (Fig. 2.16), where the carrier densities have been attributed from the corresponding theoretical curves. The large residual absorption ($\alpha \approx 1000\ \mathrm{cm}^{-1}$) below the gap is an experimental artifact and has been replaced by an exponential bandtail. This modification is in agreement with other measurements[69] and its influence on the nonlinear index data, which originate mainly from the large resonant absorption changes, is small.

Figure 2.20 shows the resulting density dependent $\alpha(N,\omega)$ and $n(N,\omega)$ used in the program. The almost linear decrease of the refractive index indicates a cross-

section $\eta \approx 4 \cdot 10^{-20}$ cm^3, and the absorption tends to saturate as the density approaches $N \approx 10^{18}$ cm^{-3}.

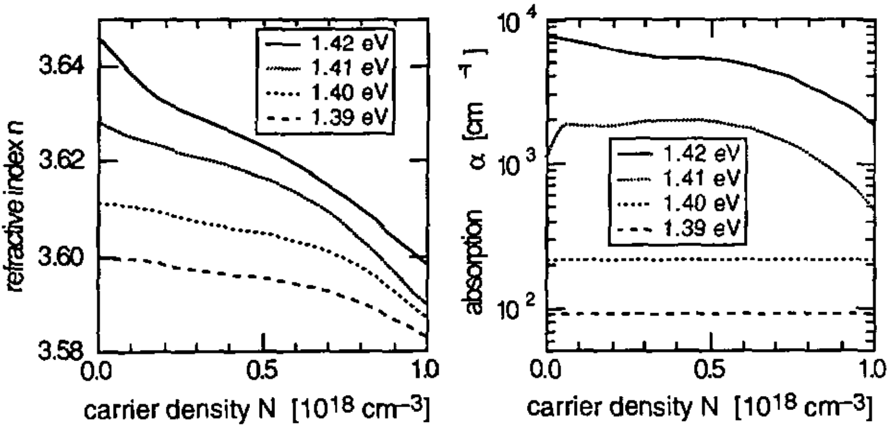

Fig. 2.20: Refractive index $n(N,\omega)$ and absorption $\alpha(N,\omega)$ as a function of carrier density, as used in the numerical model.

The following values have been assumed in the rate equation Eq. 2-67 for the thermal carrier density N_{th}, and the contributions to carrier relaxation from bulk recombination τ_{RS}, bimolecular ($\mathcal{B}$) and Auger recombination ($\mathcal{A}$) as well as surface recombination ($\mathcal{S}$)[48]

$$N_{th} = 4.5 \cdot 10^{16}\ \text{cm}^{-3}\ , \tag{2-68}$$

$$\tau_{RS} = 4\ \text{ns}\ ,$$

$$\mathcal{S} = 5 \cdot 10^{2}\ \text{cm/s}\ ,$$

$$\mathcal{B} = 1.8 \cdot 10^{-11}\ \text{cm}^3/\text{s}\ ,$$

$$\mathcal{A} = 1.5 \cdot 10^{-30}\ \text{cm}^6/\text{s}\ .$$

For $Al_xGa_{1-x}As$ alloys, the linear refractive index $n(\omega,x)$ is interpolated from published data for pure GaAs[33] (Fig. 2.14) and AlAs[70], using the interpolation given in Eq. 2-44b. Similarly, the absorption is estimated from a rigid shift[71] of the absorption spectrum of GaAs by the difference in gap energy[35] (Eq. 2-44a)

$$\alpha(\hbar\omega,x) = \alpha_{GaAs}(\hbar\omega - [E_g(x) - E_g(0)]\,)\ . \tag{2-69}$$

Validity

The principal restrictions of this steady state plane wave model have been discussed in Sect. 2.2.3.

The steady state solutions of the carrier rate equation (Eq. 2-45) are valid for time scales longer than the relaxation time τ which determines the switching OFF transition and thus limits the device operating rate.

Transverse effects due to diffusion and diffraction cannot be studied. Carrier diffusion vanishes for the plane waves assumed, and diffraction cannot be treated properly because the superposition principle is not applicable in the nonlinear case. Experimental results on the spotsize dependence of thresholds are presented in Sect. 3.5.7.

Temperature is not explicitly included in the model. However, an eventual temperature rise created by the pump beam is implicitly included in the experimental material data. In the experiment, heating can be reduced by using pulsed excitation at low duty cycle.

2.4 Dielectric (Bragg) reflector

The propagation of light in a periodic dielectric structure such as a dielectric mirror (Bragg reflector) can be solved analytically. The first subsection uses a coupled wave approach[72,73] to derive spectral characteristics and lumped parameters for the periodic Bragg reflectors. The linear phase dispersion which corresponds to an equivalent optical thickness, and the influence of weak absorption, are of particular interest. The nonlinear Bragg reflector device (NLBR), which is based on the resonant feature at the stopband edge of a dielectric mirror, is discussed in the second subsection.

2.4.1 Coupled wave theory

The coupled wave approach is a first order perturbation theory which describes the effects of a periodic polarization variation on a set of orthogonal eigenfunctions of the unperturbed Maxwell equations. Originally it was introduced for the calculation of microwaves in waveguide structures[72]. Later it found application to the calculation of thick holographic phase gratings[73], but has since been applied to a wide range of static and dynamic perturbations of free-space and guided waves.

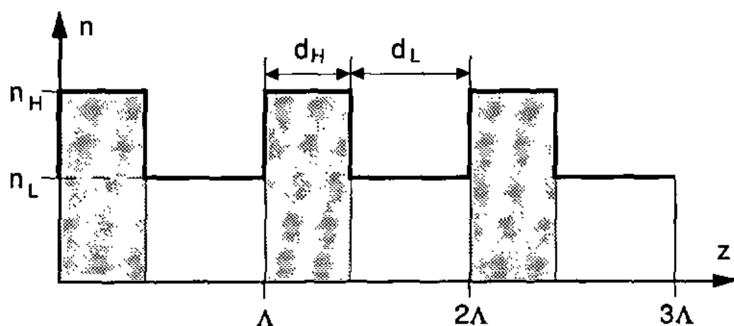

Fig. 2.21: Refractive index modulation in a Bragg reflector which consists of a periodic alternation of quarter wave layers ($n_H d_H = n_L d_L = \lambda_B/4$) along z.

A Bragg reflector consists of a periodic alternation (of quarter wave layers $n_H d_H = n_L d_L = \lambda_B/4$ with respect to the Bragg wavelength λ_B) of two dielectric materials with high and low indices n_H and n_L (Fig. 2.21). Here, a square index

modulation with a period $\Lambda = 2\pi/K$ ($= d_H + d_L$) along the $\hat{z}$ axis is assumed, together with a weak, constant absorption α (the influence of an inhomogeneous α is negligible: $\alpha/2k \ll \delta\bar{n}$). Retaining only the first harmonic, the perturbation $\Delta\varepsilon(z)$ of the average dielectric constant ε can be approximated by

$$\Delta\bar{\varepsilon}(z) \approx 2\bar{n}\left(\delta\bar{n}\,\frac{2}{\pi}\sin Kz - i\,\frac{\alpha}{k}\right), \qquad (2\text{-}70)$$

where the average index $\bar{n}$ and the index step $\delta\bar{n}$ are defined as

$$\bar{n} \equiv \frac{n_H + n_L}{2}, \qquad \delta\bar{n} \equiv n_H - n_L. \qquad (2\text{-}71)$$

(For asymmetric stacks, where $\bar{\varepsilon} = n_H n_L$, this choice is more appropriate than for instance[65] $\varepsilon = [n_H{}^2 + n_L{}^2]/2$, $\delta\varepsilon = n_H{}^2 - n_L{}^2$). The basic equation of coupled wave theory is a wave equation, where the inhomogeneous term accounts for a polarization perturbation; in this case a scalar Helmholtz equation (Eq. 2-35) is used

$$\nabla^2 E_\omega + k^2 \varepsilon\, E_\omega = -k^2 \Delta\bar{\varepsilon}(z)\, E_\omega\,; \qquad k = \frac{\omega}{c} \qquad (2\text{-}72)$$

The trial solution is a linear combination of solutions of the homogeneous equation with z-dependent amplitudes $C(z)$. Two scalar plane waves (Eq. 2-47) which propagate in opposite directions normal to the reflector are appropriate in this case:

$$E = C^+(z)\, e^{i(\beta z - \omega t)} + C^-(z)\, e^{i(-\beta z - \omega t)}\,; \qquad \beta \equiv k\bar{n}\,. \qquad (2\text{-}73)$$

Inserting this into Eq. 2-72, and assuming weak coupling conditions ($|\beta \partial C/\partial z| \ll |\partial^2 C/\partial z^2|$, fulfilled in AlGaAs) leads to two coupled linear differential equations. For a stack extending from $z = 0$ to $z = d$, and assuming light incident from one side only ($C^-(d) = 0$), the solutions are proportional to

$$C^+(z) = e^{+i\Delta\beta z/2}\left\{v \cosh v\kappa(z-d) - i\delta \sinh v\kappa(z-d)\right\}, \qquad (2\text{-}74)$$
$$C^-(z) = e^{-i\Delta\beta z/2}\left\{\sinh v\kappa(z-d)\right\}.$$

The two principal parameters in these expressions are the phase mismatch $\Delta\beta$, which is the (double) deviation of the propagation constant β from the Bragg condition $2\beta_B \equiv K$, and the coupling constant κ proportional to the refractive index step $\delta\bar{n}$

$$\Delta\beta = 2\beta - K = 2(\beta - \beta_B), \qquad \kappa = \frac{1}{\Lambda}\frac{\delta\bar{n}}{\bar{n}} = \frac{2\delta\bar{n}}{\lambda_B}, \tag{2-75}$$

$$\delta = \frac{\Delta\beta - i\alpha}{2\kappa}, \qquad \nu = \sqrt{1-\delta^2}.$$

For oblique incidence $\theta \neq 0$, the propagation constant becomes $\beta = k\bar{n}\cos\theta$ (Eq. 2-73). The Bragg condition shifts to shorter wavelengths and κ increases for TE ($\kappa \sim \cos\theta^{-1}$) and decreases for TM ($\kappa \sim \cos 2\theta/\cos\theta$) polarization.

Reflection characteristics

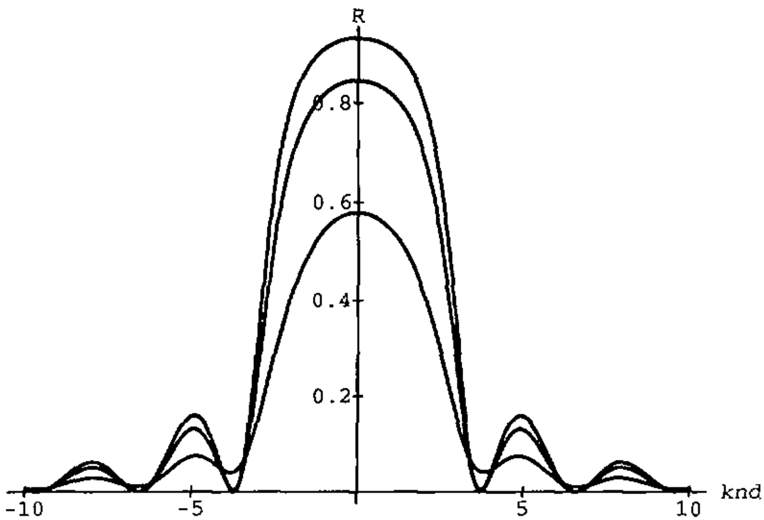

Fig. 2.22: Bragg reflector (kNL = 2) with absorption (a/k = 0, 0.1, 0.5): reflectivity spectrum vs. phase mismatch $\Delta\beta d/2 = \Delta knd$.

The complex reflection and transmission coefficients of a dielectric stack of N layers ($d = N\Lambda$) are therefore

$$r_N = \frac{C^-(0)}{C^+(0)} = \frac{-\sinh \nu\kappa N\Lambda}{\nu \cosh \nu\kappa N\Lambda + i\delta \sinh \nu\kappa N\Lambda}, \tag{2-76}$$

$$t_N = \frac{C^+(N\Lambda)}{C^+(0)} = e^{i\Delta\beta N\Lambda/2} \frac{\nu}{\nu \cosh \nu\kappa N\Lambda + i\delta \sinh \nu\kappa N\Lambda}.$$

Fig. 2.22 shows the reflectivity vs the mismatch $\Delta\beta$ at different absorptions α.

The presence of absorption in the reflector reduces the reflectivity at the Bragg peak ($\Delta\beta = 0$) and increases the reflectivity at the side minima. For thick reflectors ($\kappa d \gg 1$) the ratio between absorbed ($A \approx 1-R$) and reflected ($R = |r|^2$) intensity at Bragg condition is

$$\lim_{d\to\infty} \frac{A}{R}\Big|_{\Delta\beta=0} = |\nu + i\delta|^2 - 1 \approx \frac{\alpha}{\kappa} . \tag{2-77}$$

In the absence of absorption, the peak intensity reflectivity $R_N(\beta_B)$ of a stack is simply

$$R_N(\beta_B) = \tanh^2 N\kappa\Lambda . \tag{2-78}$$

A marked drop of the reflectivity occurs at the edges of the stopband $\Delta\beta = \pm\delta\beta$, where, for $\alpha = 0$, the forward solution C^+ changes from an exponentially damped wave into a traveling wave

$$\frac{\delta\beta}{2} = \kappa = \frac{\beta_B}{\pi} \frac{\delta\bar{n}}{\bar{n}} , \tag{2-79}$$

$$R_N(\Delta\beta{=}\pm\delta\beta) = \frac{|N\kappa\Lambda|^2}{1 + |N\kappa\Lambda|^2} .$$

The relative spectral width of the so determined stopband is $\Delta\omega/\omega = \delta\beta/\beta_B$.

Outside the stopband the reflection passes N–1 minima (zero reflection if $\alpha = 0$) at phase mismatches

$$\frac{\Delta\beta_N^m}{2} \approx \pm\kappa \sqrt{1 + \left(\frac{m\pi}{N\kappa\Lambda}\right)^2} ; \qquad m = 1, N . \tag{2-80}$$

before $\Delta\beta_N^N$ which would correspond to the next harmonic Bragg peak.

Equivalent optical thickness

In the vicinity of the Bragg condition the phase of the complex reflection coefficient is linear up to terms in $\Delta\beta^3$. Therefore the phase dispersion within the stopband can be interpreted as an equivalent thickness L_N (assuming an average index $\bar{n}$). For a thick reflector, L_N approaches half of the reciprocal coupling length (cf Fig. 2.23)

$$L_N \equiv \frac{1}{2\bar{n}} \frac{\partial \arg(r_N)}{\partial k}\bigg|_{\Delta\beta=0} \approx \frac{1}{2\kappa} \tanh N\kappa\Lambda \,. \tag{2-81}$$

Accuracy of coupled mode results

The periodic stack with N periods can be solved exactly, using the matrix theory of Sect. 2.3.1, by calculating the Nth power of the (diagonalized) matrix of a dielectric period $\mathbb{F}_H\mathbb{P}_H\mathbb{F}_L\mathbb{P}_L$. The coupled wave result in Eq. 2-78 has a very similar form to the exact solution at the Bragg condition

$$R_N(\beta_B) = \tanh^2\left(N \log \frac{n_H}{n_L}\right). \tag{2-82}$$

The perturbation theory approximates the logarithm of n_H/n_L by a linear expression $\kappa\Lambda = \delta\bar{n}/\bar{n}$. In typical AlGaAs reflectors an average index of $\bar{n} \approx 3.3$ and an index steps of $\delta\bar{n} \le 0.6$ yield $\kappa\Lambda \le 0.18$. Thus, the error of a coupled wave approach with the above choice $\delta\bar{n}$ and $\bar{n}$ is less than 0.3% for a single period and decreases further with N. This is about the precision of the available index data, and small compared to spectral dispersion effects.

Another indication for the accuracy of the coupled wave model is the influence of the phase mismatch $\Delta\beta$. A reflector consisting of N periods with abrupt index steps has N–1 nodes of zero reflectivity ($\alpha = 0$) between two Bragg peaks which correspond to different harmonics ($\beta_m = mK/2$). The coupled wave approach considered only the first harmonic $j = 1$, and therefore describes only one Bragg peak. Still, the Nth node ($\Delta\beta_N$ in Eq. 2-80) coincides almost exactly with the next Bragg peak (up to 0.1% for the above $k\Lambda$) .

Therefore, coupled wave theory gives simple expressions with highly satisfying accuracy for AlGaAs reflectors with any number of layers.

Boundary interfaces

For a finite stack, the refractive indices of the adjacent media generally differ from n_H and n_L. In the matrix approach the interface from the incident (n_0) to the front layer (n_1) would be considered by an additional Fresnel matrix. For the reflection coefficient this is described by Airy's formula which changes the amplitude reflection r_N and the optical path L_N of a periodic stack to

$$r'_N = \frac{r_{01} + r_N}{1 + r_{01}\, r_N}; \qquad r_{01} = \frac{n_0 - n_1}{n_0 + n_1}, \qquad (2\text{-}83)$$
$$L'_N = \mathrm{Re}\left\{\frac{1 - r_{01}^2}{(1 + r_{01} r_N)(r_{01} + r_N)} r_N\right\} L_N \quad \rightarrow \frac{n_0}{n_1} L_N .$$

The symmetry between r_{01} and r_N expresses that the reflection is independent of the viewing direction. For thick stacks, where r_N tends to -1, the equivalent penetration length L'_N scales with the index ratio n_0/n_1.

The uncorrected and the corrected ($n_0 = 1$ for air) reflectivity R'_N and penetration length L'_N of a typical AlGaAs Bragg stack is depicted in Fig. 2.23. An equal correction for the rear interface, to the GaAs spacer or substrate can generally be neglected because $n_2 \approx n_{GaAs}$ (and because $\alpha d \gg 1$ for an absorbing substrate).

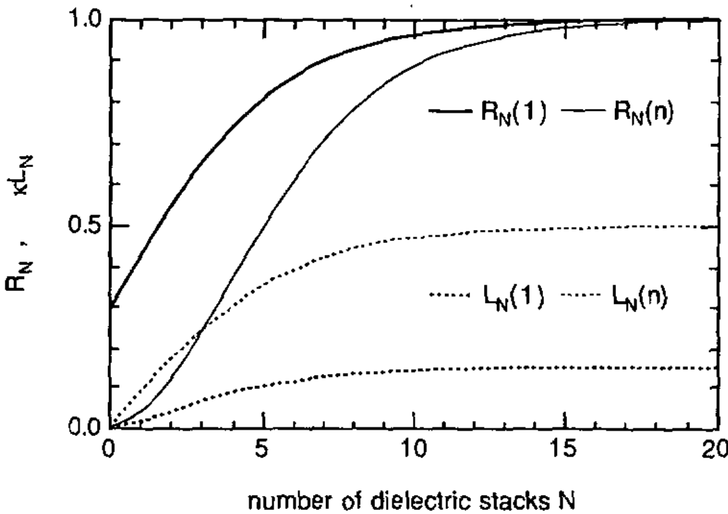

Fig. 2.23 *Peak reflectivity R_N ($\Delta\beta=0$) and equivalent thickness κL_N of an AlGaAs Bragg reflector ($0[HL]^N$), from air ($n_0=1$) and from $n_0=n_L$ ($1/\kappa = 0.77\ \mu m$, $\kappa\Lambda = 0.175$, $n_H = 3.57$, $n_L = 2.99$, $\lambda = 0.88\ \mu m$).*

2.4.2 Nonlinear Bragg reflector (NLBR)

The potential for optical bistability in a nonlinear distributed feedback structure has been pointed out early[74], but only recently a realization based on AlGaAs has been proposed[75]. Based on the analytic results of Section 2.4.1, this section introduces the operating principles and some design issues for a nonlinear Bragg reflector (NLBR) device. The numerical optimization of a NLBR for growth in AlGaAs will be described in Section 2.6.

Feedback

At the stopband edge of a Bragg reflector there is a transition from a damped to a transmitted wave, manifested by an abrupt descent of the reflectivity (cf Fig. 2.22). The phase mismatch $\delta\beta$ at the stopband edge is proportional to $\delta\bar{n}$, which may depend on the penetrating optical field. Thus, the penetrating optical intensity can shift this resonant feature to shorter wavelengths, similar to the shift of the resonance of a reflective nonlinear Fabry-Perot. A positive feedback, and therefore bistability, can occur on the long wavelength edge of the stopband for negative refractive index changes $\Delta n < 0$.

The theory[74] gives coupled wave solutions for a lossless Bragg reflector with a homogeneous Kerr-type nonlinearity. It postulates a minimum coupling length for bistability of about $N\kappa\Lambda \approx 2$. The expected thresholds are comparable to an equally thick NLFP.

Resonance

The relative spectral distance between the stopband edge (Eq. 2-79) and the first reflection minimum (Eq. 2-80) is a measure for the steepness of the transition, similar to a "finesse" $\mathcal{F}$

$$\frac{1}{\mathcal{F}} \equiv \frac{(\Delta\beta_N^1 - \delta\beta)}{2\beta_B} \approx \frac{\pi}{2\kappa\Lambda}\frac{1}{N^2}. \tag{2-84}$$

Large coupling lengths $N\kappa\Lambda$ are thus desired to reduce the nonlinear phase change.

In a Bragg reflector consisting of GaAs and AlAs layers, a maximum coupling constant $\kappa \leq 1.44\ \mu m^{-1}$ can be obtained ($n_{GaAs} = 3.62$, $n_{AlAs} = 2.98$ at 885 nm). This corresponds to a coupling length $N\kappa\Lambda = 5.8$ and a "finesse" $\mathcal{F} \approx 110$ for a 4 µm thick reflector ($\Lambda = 0.135\ \mu m$, $N = 30$).

The feasible thickness $N\Lambda$ of the reflector will be limited by the intensity penetration depth, which is given by the absorptive coupling length $1/\alpha$. For GaAs, at wavelengths above 880 nm, this would allow for $N\Lambda \geq 15\ \mu m$.

Nonlinearity

A homogeneous change of the average refractive index ($\Delta\bar{n} < 0$) shifts the Bragg peak (Eq. 2-75), and thus the stopband edge to shorter wavelengths.

$$\frac{\Delta\beta}{2\beta_B} = -\frac{\Delta\bar{n}}{\bar{n}} . \tag{2-85}$$

If only the high index layer n_H is nonlinear ($\Delta n_H < 0$), the reduction of the average refractive index $\bar{n}$, and therefore the shift of the Bragg peak is only half of the above. However, the index step $\delta\bar{n}$ is reduced in this case, so that the width of the stopband (Eq. 2-79) shrinks. The total shift on the long wavelength edge remains unaltered compared to Eq. 2-85.

To take advantage of the resonant refractive nonlinearity in GaAs, the operating wavelength at the stopband edge has to be positioned around 880 nm. A rough measure for the required phase change is the relative mismatch $1/\mathcal{F} \approx 1/110$ estimated from Eq. 2-84. It corresponds to a nonlinear refractive index change $\Delta n_H \approx 0.03$, which is realistic according to the data of Fig. 2.16.

Intensity

The intensity distribution (and thus the nonlinear index) in a NLBR varies not only over a period Λ, but also over a larger scale (Eq. 2-74) $(\nu\kappa)^{-1}$ ($> \kappa^{-1} \approx 6\Lambda$). This longitudinal dependence complicates the analytical understanding of the NLBR[76] and is the reason why the devices measured in Section 3.7 have been optimized numerically (cf Sect. 2.5.2).

An example for the possible resonant enhancement in Bragg structures is the impact of a reflection at the rear of a Bragg mirror. Replacing the rear boundary condition ($C^-[d] = 0$) by a complex reflection coefficient r ($C^-[d] = r \cdot C^+[d]$), the reflection and transmission coefficients of Eq. 2-76 are changed to

$$r_N = \frac{\eta\nu \cosh \nu\kappa N\Lambda - (1+ir\delta) \sinh \nu\kappa N\Lambda}{\nu \cosh \nu\kappa N\Lambda - (r-i\delta) \sinh \nu\kappa N\Lambda} , \tag{2-86}$$

$$t_N = e^{i\Delta\beta N\Lambda/2} \frac{\nu}{\nu \cosh \nu\kappa N\Lambda - (r-i\delta) \sinh \nu\kappa N\Lambda} .$$

For a wave incident at the stopband edge, the relative intensity at the rear of the Bragg reflector, given by the transmission coefficient T can become very large for $|r| \approx 1$ and is very sensitive to the phase of r

$$T_N = |1-(r-i)\kappa N\Lambda|^{-2} \leq |2\kappa N\Lambda|^2 . \qquad (2\text{-}87)$$

This enhancement by a linear rear mirror has been used in an improved NLBR design.

2.5 Numerical optimization

2.5.1 Integrated nonlinear Fabry-Perot

The principal design parameters of a NLFP are the operating wavelength λ and the thickness L of the spacer layer. For a given nonlinear material, they establish the material properties $\alpha(\lambda)$, $n(\lambda)$ and thus the loss parameter αL, which determines the front mirror reflectivity through the impedance matching condition (Eq. 2-13).

Such a set of lumped parameters allows one to design a first layout of the integrated structure. This preliminary layout can then be adjusted and optimized with the nonlinear simulation tool NLB (Sect. 2.3.2). Optimization issues with respect to the operating wavelength, the spacer width, and the mirror reflectivities, as well as hardware tolerancing are addressed.

Preliminary device design

The structure of the integrated NLFP for a selected resonance wavelength λ_r and an approximate spacer thickness L is established according to the following steps.

The approximate width L of the spacer layer is adjusted to a multiple of the half-wavelength $\lambda_r/2n(\lambda_r)$, which, for GaAs, is typically about 125 nm. Then, assuming a high reflectivity of the rear mirror $R_b \approx 1$, the impedance condition (Eq. 2-13) imposes a front mirror reflectivity equal to the round-trip attenuation $R_f = \exp[-2\alpha(\lambda_r)L]$.

The number of dielectric stacks corresponding to R_f can be derived from coupled wave theory (Fig. 2.23). The composition of the Bragg reflectors is selected to maximize the refractive index difference, and thus the width of the stopband (Eq. 2-79), while keeping the absorption loss low. The aluminium content of $x = 0.07$ in the high index layer puts the bandgap below 820 nm (Eq. 2-44a). The corresponding absorption of less than 10 cm^{-1} should allow for an attenuation of $\leq 0.1\%$ in a mirror with 20 stacks. The low index layer consists of AlAs in which a GaAs monolayer is included every 100 Å ($x = 0.97$) to enhance the interface quality. This gives (Eq. 2-44) refractive indices of 3.57 and 2.99, respectively for the high and low index layers. The high and low index layers are chosen to center the stopband at the selected Fabry-Perot resonance wavelength λ_r ($n_H L_H = n_L L_L = \lambda_r/4$), to avoid undesired phase contributions.

Effective cavity length

The principal difference between the distributed NLFP and the lumped model of Section 2.1.3 resides in the additional phase dispersion due to the dispersion of the refractive index (group index) and of the dielectric mirrors (equivalent thickness). Close to the Bragg condition the phase dispersion of a Bragg mirror is linear, and thus well approximated by the equivalent penetration length L_N in Eq. 2-81. The total phase dispersion in the cavity can therefore be expressed by an effective spacer length L_{eff} which is larger than L

$$L_{eff} \equiv \frac{1}{n}\frac{d\varphi}{dk} \approx \left(L + \frac{\partial\varphi_{lin}}{n\,\partial k}\right)\left(1 + \frac{k}{n}\frac{\partial n}{\partial k}\right) \approx (L + L_m)\frac{n_g}{n} \qquad (2\text{-}88)$$

The factor n_g/n describes the refractive index dispersion of the material. Around the gap of GaAs (cf Fig. 2.14) the average group index n_g is about 1.2 times the refractive index. L_m includes the equivalent thickness of the front and the rear mirrors. Based on L_{eff} one can define a so-called local free spectral range[24] which is smaller than the free spectral range $\Delta\varphi_{fsr}$ calculated in Eq. 2-8

$$\frac{\Delta\varphi_{fsr}^{loc}}{\varphi} = \frac{\Delta\lambda_{fsr}^{loc}}{\lambda} = \frac{\lambda}{2nL_{eff}}. \qquad (2\text{-}89)$$

Operating wavelength

The critical nonlinear refractive index change of a high finesse NLFP (Eq. 2-25) is proportional to the background absorption. In Fig. 2.24 the critical index change of a NLFP is compared to the nonlinear index change measured in GaAs (Fig. 2.16). Above the gap energy the large background absorption demands unfeasibly large index changes. Some 20 meV below the absorption edge however, the observed index change exceeds the required minimum value of $\Delta n \approx 0.02$.

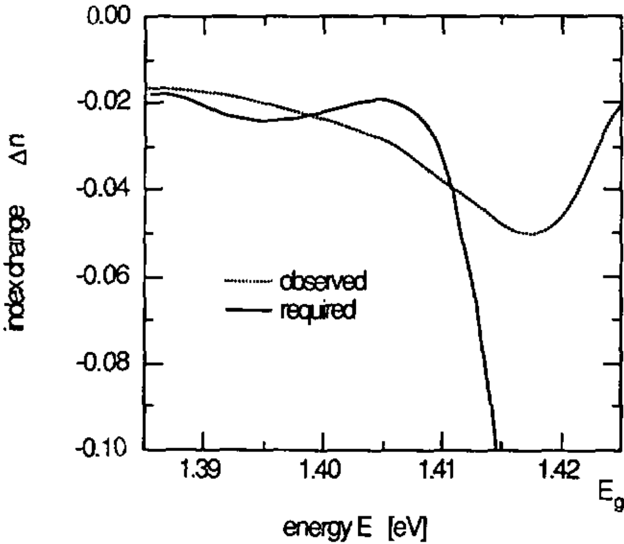

Fig. 2.24: Comparison between necessary and observed refractive index change based on experimental data[39] for GaAs ($N = 10^{18}$ cm^{-3}).

The exact resonance wavelength is controlled by varying the spacer width L. The relation between a change of the spacer ΔL and the corresponding resonance wavelength change Δλ and is determined by the effective thickness L_{eff}

$$\frac{\Delta\lambda}{\lambda} = \frac{\Delta L}{L_{eff}}. \tag{2-90}$$

Numerical simulations have been performed to determine the resonance wavelength which gives the lowest switching threshold. They indicate an optimum resonance wavelength of 882 to 885 nm, or, because of the necessary initial detuning φ_0^c (Eq. 2-23), an operation wavelength around 880 nm. A first cavity has been optimized for this wavelength range (Sect. 3.4.1), but a second, higher finesse cavity, operating at 885 nm, gave better results (Sect. 3.5.1).

As Fig. 2.22 illustrates, the ideal material has a region of low absorption close to the gap, where the resonant refractive nonlinearity is still large. Therefore, accurate absorption data is essential to optimize the cavity design.

Spacer thickness

According to Eq. 2-24, the threshold intensity drops monotonically with the spacer thickness L. This encourages the use of very short cavities. However, an ultimate minimum thickness (or maximum finesse) arises from an increasing sensitivity of the device to deviations of the operating and design parameters.

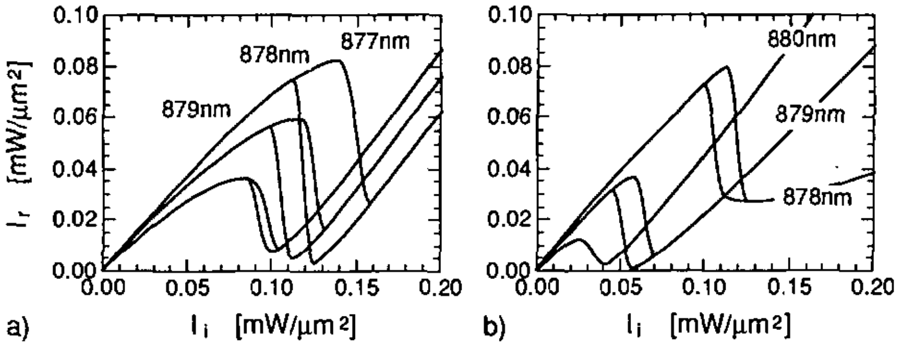

Fig. 2.25: Reflected vs incident intensity at different detuning wavelengths ($\lambda_{res} \approx 882$ nm) for two impedance matched cavities:
a) $L = 1.887\ \mu m$, $R_f = 0.75$, $R_b = 0.99$ ($N_f = 5$, $N_b = 20$),
b) $L = 0.548\ \mu m$, $R_f = 0.90$, $R_b = 0.99$ ($N_f = 9$, $N_b = 20$).

The simulated switching characteristics of two cavities with different spacer lengths are shown in Fig. 2.25. The threshold and the ON-state reflectivity of the short cavity (Fig. 2.25b, $\mathcal{F} \approx 30$) vary strongly within the bistable region which extends over about 1 nm. In comparison, for the long cavity (Fig. 2.25a, $\mathcal{F} \approx 10$), the threshold and contrast remain fairly constant in a bistable region of about 2 nm.

The increased wavelength sensitivity is due to a spectral narrowing of the FP-resonance for thin spacers. The finesse which is determined by the loss αL increases inversely to the spacer thickness L. The local free spectral range (Eq. 2-89), however, is proportional to $1/L_{eff}$, and therefore scales sublinearly due to the unchanged phase dispersion in the mirrors. Thus, any additional (linear) spacer layers should be avoided and the coupling constant κ of the reflectors should be maximized (Eq. 2-81) to reduce this wavelength sensitivity.

The ON-state reflectivity is determined by the impedance matching condition (Eq. 2-13). At higher finesse this condition becomes increasingly sensitive to deviations of the loss in the spacer $\Delta(\alpha L)$, or of the front mirror reflectivity ΔR_f from the impedance matched value: the reflectivity at resonance (Eq. 2-12a)

increases with the square of the finesse $\mathcal{F}$

$$R\,|_{\varphi=0}\,(\Delta R_f) = \frac{1}{R_f}\left(\frac{\mathcal{F}\Delta R_f}{\pi}\right)^2 . \tag{2-91}$$

The numerical simulations suggest a reasonable minimum thickness between 0.5 and 1.0 µm ($\mathcal{F} \leq 50$), if one requires similar switching characteristics over a wavelength range of about 1 nm. A threshold increase due to surface recombination is expected as the thickness approaches L ≤ 0.1 µm.

Experimental results obtained on a NLFP with a spacer of 0.6 µm thickness will be described in Section 3.6.

Dielectric stacks

The sensitivity of the switching characteristics of a NLFP to the front mirror reflectivity and to the operation wavelength is shown in Fig. 2.26:

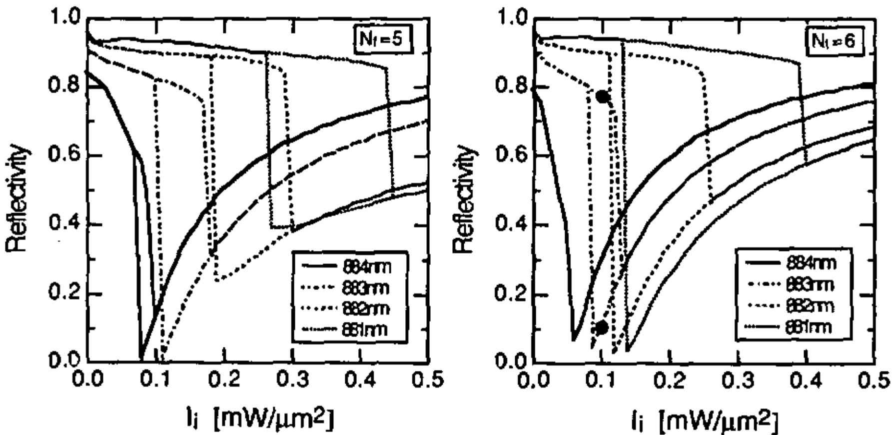

Fig. 2.26: Switching characteristics of a NLFP (L = 2 µm, λ_r = 885 nm) operated at different wavelengths. In the two simulations, the front mirror consists of N_f = 5 and 6 dielectric stacks, corresponding to R_f = 0.81 and 0.86, respectively.

The simulations for a 2 µm cavity with a resonance at 885 nm reflect the influence of several effects:

The threshold decreases monotonically with the finesse (Eq. 2-24), and thus with the number of stacks in the front mirror. For a fixed finesse it is minimal for a balanced (impedance matched) cavity (Eq. 2-15), in this case at $N_f = 5$.

The switching contrast becomes maximum if the impedance matching condition (Eq. 2-13) is achieved in the ON-state. Because of the wavelength dependence of the absorption this condition ($T_f = 2\alpha[\lambda]L$) is fulfilled at a single operating wavelength only. In Fig. 2.26 the wavelength corresponds to $\lambda \approx 884$ nm ($N_f = 5$) and $\lambda \approx 882$ nm ($N_f = 6$). The decreasing wavelength for an increasing mirror reflectivity in these simulations is due to absorption saturation.

This tradeoff between threshold and wavelength dependent contrast ratio favors a mirror reflectivity higher than according to the impedance matching condition.

Tolerances

Tolerances play a role at three levels, from the accuracy of physical data at the design stage, over the precision of thickness and composition during growth, to the device operating tolerances. The discrepancies between physical data and observed material properties can be eliminated by an optical calibration of the growing equipment. This leaves the growth reproducibility as a fabrication tolerance. Device operating tolerances will be addressed in Chapters 3 and 4. Deviations of thickness and composition contribute to an erroneous optical path length. Therefore, they influence the amplitude and the phase inside a NLFP:

The amplitude attenuation is governed by the impedance matching condition which determines the minimum reflectivity (contrast) of the Fabry-Perot. This reflectivity (Eq. 2-91) depends quadratically on deviations of the spacer absorption ($\alpha\Delta L$), or the mirror reflectivity (ΔR_f). Small deviations of the spacer length ΔL are thus not critical. Similarly, the broad reflection characteristic of Bragg mirrors (Eq. 2-79), allows for relative thickness errors $\Delta\Lambda/\Lambda$ up to about 5% without significant reflectivity change ΔR_f.

The phase condition leads to sharper requirements for the growth precision. To set the resonance wavelength within the desired range of about 3 nm, the relative error for a 2 μm spacer $\Delta L/L$ has to be less than 0.5% ($\Delta L \leq 10$ nm). Similarly, the deviation of the Bragg wavelength of a reflector gives an additional phase contribution (linear dispersion L_N in Eq. 2-81). As a consequence, the wavelength tolerance of 3 nm limits the relative error of the stack period $\Delta\Lambda/\Lambda$ to about 1.3%.

Experimentally there is some tuning capability, by changing the temperature or the position on the wafer, or by using a resonance of different order; the relative free spectral range (Eq. 2-89) of a 2 μm cavity ($L_{eff} \approx 3.3$ μm) is about 4%.

Intensity profile

For illustrative purposes, Fig. 2.27 shows a profile of the standing wave intensity in a NLFP before and after switching.

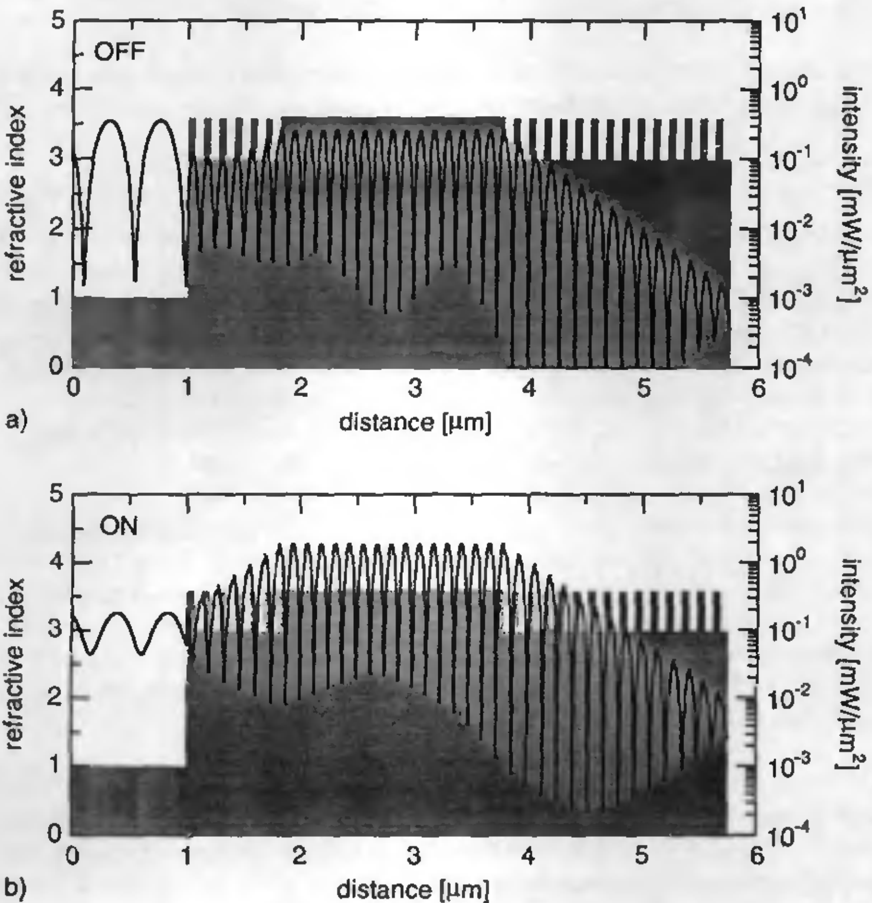

Fig. 2.27: Standing wave intensity and refractive index profile in a 2 μm cavity ($N_f = 6$, $\lambda = 883$ nm and $I_i = 0.1$ mW/μm² marked in Fig. 2.20) a) before, and b) after switching ON.

2.5.2 Nonlinear Bragg reflector

The numerical tool NLB allows the simulation of stacks with multiple nonlinear layers. Recently it has been used to design a nonlinear Bragg reflector (NLBR), as introduced in Section 2.4.2. No systematic optimization of parameters has been performed for the NLBR so far; the design originated rather from practical assumptions discussed in section 2.4.2, in particular the finding that the threshold is lowered by an additional reflection at the rear.

Device design

The composition of the stack is selected to maximize the coupling coefficient κ (cf Eq. 2-75): the nonlinear high index material is pure GaAs and the low index material is AlAs (with a monolayer GaAs about every 40 lattice periods to improve the growth quality). A stack with 30 periods ($L_H \approx 60$ nm) has been selected to allow comparison with the NLFP of 2 μm spacer thickness.

Operating wavelength

The nonlinear behavior of devices has been investigated at different operating wavelengths and different positions of the stopband edge (Eq. 2-73). Simulations of stacks with a reflection minimum at 885±3 nm showed bistable switching with thresholds of about 0.15 $\mu W/\mu m^2$. The similar wavelength range and thresholds are not surprising, because NLBR and NLFP rely on the same resonant material properties in a similar resonant optical structure.

Improvement by rear reflector

In simulations of NLBR without a substrate (rear refractive index 1), a significant threshold decrease was found as a consequence of the additional rear reflection. This is due to the transmitted light which, if reflected back into the structure, contributes a second time to the nonlinearity, as in the reflective NLFP.

A second NLBR structure was optimized with an additional linear reflector behind the nonlinear stack. The stop band of the linear stack is centered at the operating wavelength (885 nm), to maximize the back reflection. Its dielectric layers are therefore identical to those of the NLFP device.

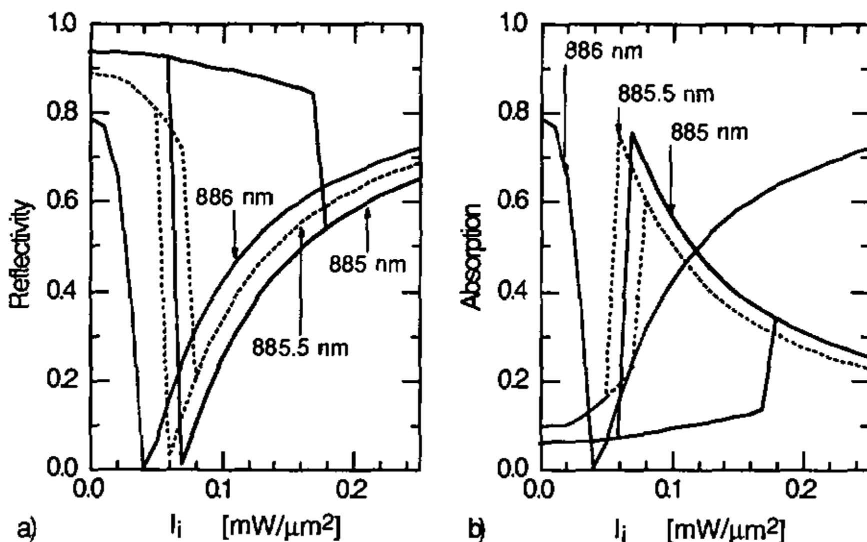

Fig. 2.28: Reflectivity (a) and absorption (b) vs intensity at different wavelengths incident on a NLBR with 30 nonlinear and 8 linear dielectric layers.

The minimum threshold is found to decrease monotonously with the reflectivity of the linear stack, namely I = 0.1 mW/μm^2 and 0.05 mW/μm^2 for R = 0.45 and 0.82, corresponding to 4 and 8 dielectric layers, respectively. Figure 2.28 shows the switching characteristics of a device, which depends strongly on the operating wavelength. The high fraction of absorbed power is an indication for the resonant enhancement in the NLBR.

The phase of the linear reflector determines the phase relation between forward and backward traveling waves, and thus the position of the standing wave with respect to the nonlinear layers. This phase can be adjusted through the thickness of the linear layer between the two mirrors. Fig. 2.29 shows its dramatic influence on the switching characteristics. Its optimization is complicated because the main (linear) impact is a shift of the reflectivity spectrum, and accordingly of the operating wavelength. A layer thickness of 5/16λ has been retained because it promises steeper characteristics, a 10% increase in the peak absorption, and a smaller wavelength dependence compared to the λ/4 layer in Fig. 2.28.

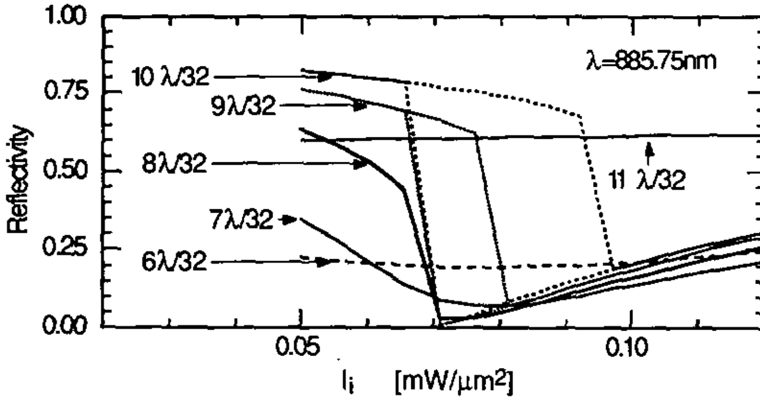

Fig. 2.29: Reflectivity vs. incident intensity for different widths of the intermediate AlAs layer (NLBR with 30 nonlinear and 5 linear dielectric layers, λ = 885.75 nm).

The phase of the linear reflector determines the phase relation between forward and backward traveling waves, and thus the position of the standing wave with respect to the nonlinear layers. This phase can be adjusted through the thickness of the linear layer between the two mirrors. Fig. 2.29 shows its dramatic influence on the switching characteristics. Its optimization is complicated because the main (linear) impact is a shift of the reflectivity spectrum, and accordingly of the operating wavelength. A layer thickness of 5/16λ has been retained because it promises steeper characteristics, a 10% increase in the peak absorption, and a smaller wavelength dependence compared to the λ/4 layer in Fig. 2.28.

Conclusion and outlook

The nonlinear Bragg mirror uses the same nonlinearity as the NLFP. For the feedback, it relies on the resonant feature at edge of the stop band, which is similar to the resonance of a NLFP. The difference is that the nonlinearity is distributed over the feedback structure which can no longer be described by lumped constant parameters. This complicates an analytical description, and thus the understanding, of the interaction between the optical field (intensity I, initial mismatch $\Delta\beta$) and the resonant Bragg structure (linear and nonlinear coupling κ, absorptive attenuation α), and calls for numerical optimization.

On the other hand, the simple structure of a NLBR may be easier to fabricate than a NLFP, because it demands repeatability rather than absolute growth precision. Also, the NLBR is potentially more tolerant than an NLFP. Its principal parameter is the separation of the stopband edge from the semiconductor gap which could be controlled by temperature.

The more complicated structure with an additional linear mirror enhances the nonlinear characteristics and reduces transmission losses. This design reduces the threshold to that of a 0.5 μm NLFP, but in exchange, suffers from a similar detuning sensitivity. Its high sensitivity to the phase of the rear reflector leads to a growth tolerance for the thickness of the intermediate phase layer ($\lambda/32n \approx 8$ nm) equal to that of the NLFP spacer. The similarity of the phase layer to the NLFP spacer becomes obvious if control of its optical length is attempted (electrically, optically or by temperature) for biasing or modulation purposes.

A further optimization of the NLBR device should elucidate the optimum thickness $N\Lambda$ which could be considerably longer ($\leq 1/\alpha \approx 15$ μm) according to the analytical considerations in Sect. 2.4.2. (An initial limitation of the number of layers by the numerical program has been overcome now.) Improvement can also be expected by introducing chirp in the periodicity and in the composition of the stack. In this way, the stopband edge could be made steeper, which would reduce the necessary nonlinear shift, and the absorption and intensity profile inside the stack could be optimized.

3 Experimental Work

The availability of appropriate epitaxial AlGaAs samples has been an essential issue for the progress of the experimental work. Table 3.1 gives an overview on the relevant samples which are described in more detail in the subsequent sections.

The standard characterization techniques used, as well as the experimental setup built for the nonlinear optical characterization, are introduced in Section 3.1. The importance of sample characterization is twofold: first to evaluate whether, and under what conditions, a sample is suited for nonlinear device studies and second, to improve the calibration of the growth process. Section 3.2 describes the calibration effort conducted to meet the demanding thickness requirements. Section 3.3 presents attempts to adjust the properties of non-ideal existing samples by processing and temperature tuning.

The last four sections discuss the experimental results which were obtained on four specific nonlinear device samples. Section 3.4 discusses nonlinear refractive index measurements based on nonlinear resonance shifts on a low finesse NLFP (#337). The principal part which deals with the characterization of optical bistability in a 2 µm thick NLFP (#360) is described in Sect. 3.5. Sect. 3.6 gives some comments on short cavity devices, based on measurements on a NLFP with a 0.6 µm thick spacer (#386), and finally, Sect. 3.7 presents some recent results on NLBR structures (#363, #388).

3.1 Characterization techniques

Sample characterization is important in verifying the properties of a fabricated device, and also in improving future devices via a rapid feedback of calibration data to crystal growers. The standard techniques that have been used to measure structural properties of a sample (thickness, composition, doping) are introduced in Section 3.1.1. Among these, spectral reflectivity measurements (SRM) are prominent, because they give access to optical device parameters such as Fabry-Perot resonance position, Bragg wavelength, etc. Section 3.1.2 describes the setup based on pulsed excitation with a coherent source, which has been built for the measurement of linear and nonlinear reflectivity and dynamic switching.

Sample	Structure	(Accuracy)	Characteriz.	Processing	Nl. measure.
	Nonlinear λ/4 layer (GaAs) High index λ/4 layer (AlGaAs) Low index λ/4 layer (AlAs)		TEM XRD PL CV/ IV/ PC SRM	Etching Sputtering Temp. tuning	NL-index Switching Bistability
Calibration					
#302 (various QW)	5 QWs, with/out rotation		P		
#380 (optical flat)	optical flat for calibration		S		
NLBR					
#212 (VCSEL)	20[LH]13[NN]20[LH]		S	E, T	S
#224 (VCSEL)	17[HL]12[NN]22[LH]		S	E, T	S
#320 (VCSEL)	4[HH]8[NN]8[HH]20[LH]		S	E, S, T	S
#337 (2 μm NLFP)	5[HL]16[NN]20[LH]	//-3%	S, X, C, T	T	N, S
#352 (2 μm NLFP)	7[HL]16[NN]20[LH]	//12%	S		
#360 (2 μm NLFP)	7[HL]16[NN]20[LH]	//5%	S, X, P, C, T		N, S, B
#386 (0.6 μm NLFP)	8[HL]5[NN]20[LH]	≤0.5%	S		S, B
NLBR					
#363 (NLBR)	30[NL]	+8%	S	T	S
#388 (mod. NLBR)	30[NL]8[HL]	−1%	S	T	S, B

Table 3.1: Calibration samples and nonlinear NLFP, and NLBR devices used: growth number, structure, accuracy and measurements conducted on them. The methods used for characterization, processing, and nonlinear measurements are described in sections 3.1 to 3.3.

3.1.1 Standard techniques

All the relevant samples (Table 3.1) are AlGaAs crystals grown by the molecular-beam-epitaxy facility (MBE, Varian) at the Institut de Micro- et Optoélectronique (IMO) at the Ecole Polytechnique Fédérale (EPFL) in Lausanne. The following standard characterization methods have been used at the same site.

Transmission electron microscopy (TEM)

TEM allows one to image the structure of a sample down to atomic resolution. Figure 3.1 shows the picture of a wedge (WTEM[77]) cleaved from a dielectric mirror (#337): the periodicity of the superlattice in the high index layer is 11 lattice periods. If it is used in the diffraction mode, TEM gives information on the lattice parameters (orientation). TEM is suited for a local inspection of samples, although it deteriorates the exposed surface (or edge for WTEM). The typical uncertainty of ± 5 % in the magnification factor proved insufficient for the thickness calibration of optical devices.

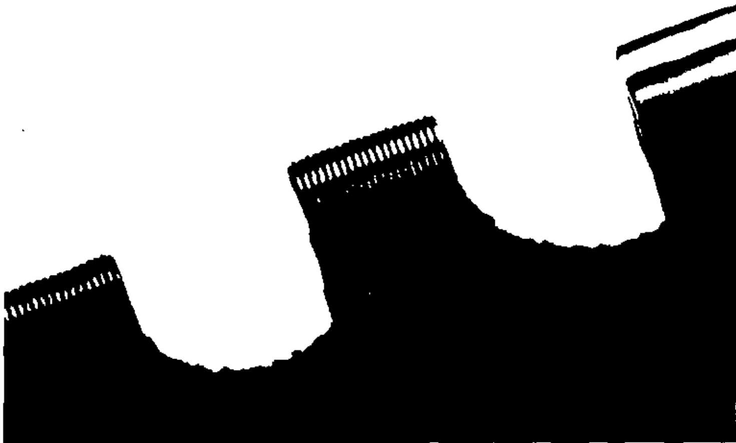

Fig. 3.1 *WTEM picture of the rear Bragg mirror of sample #337. The high index layer is a $(AlAs)_3(GaAs)_8$–superlattice of 64 nm thickness. (courtesy J.D. Ganière)*

X-ray diffraction (XRD)

XRD is a non-destructive tool to precisely determine the periodicity parameters of a crystalline structure. As opposed to TEM, XRD is a nonlocal method based on the angular diffraction of a monochromatic collimated X-ray beam ($\lambda[\mathrm{Cu}_{\mathrm{Ly}\,\alpha}] = 1.5406$ Å, $\delta\theta < 5\cdot10^{-6}$ rad). For the present heterostructures XRD reveals periodicity information over three orders of magnitude. This is apparent in the XRD spectrum of a rear dielectric mirror (#337) in Fig. 3.2: the central reference peak is the diffraction from the GaAs substrate ($2\theta = 31.7°$ for {200} planes). The two satellite peaks stem from the superlattice in the high index stack (with a period of 11/2 lattice constants a). The central sidelobes are related to the dielectric stack. Their spacing and relative amplitudes[78] give information on the period (≈490a/2) and the duty cycle of the stack. Finally, the offset of the diffraction peak center with respect to the reference peak is due to the elastic lattice deformations[79] and therefore gives information the average aluminium concentration in the superlattice and the dielectric mirrors. Periodicities can be determined with an accuracy better than 1 %. The determination of composition is less precise, due to the good lattice matching between GaAs and AlAs (lattice constants of $a_{GaAs} = 5.6533\pm0.0001$, and $a_{AlAs} = 5.6617\pm0.0005$ at room-temperature were assumed).

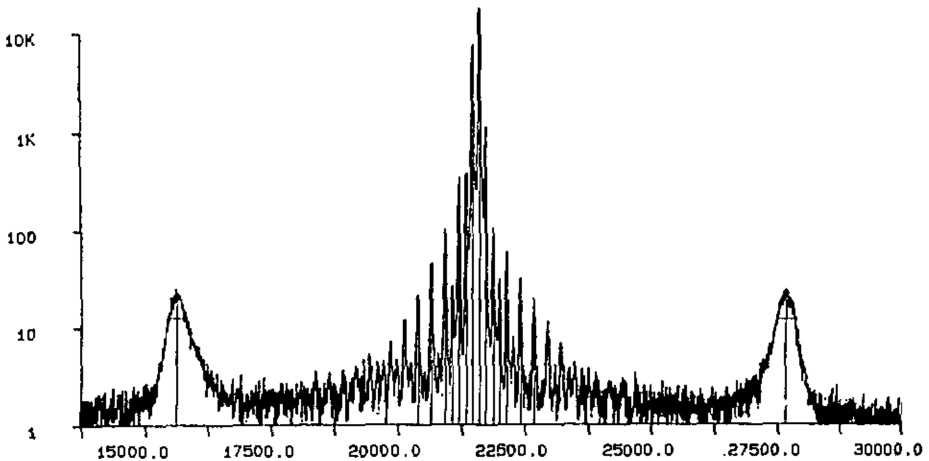

Fig. 3.2 *XRD spectrum of the rear mirror of NLFP #337: the satellites stem from the superlattice in the high index layer, while the central structure reveals the period and composition of the dielectric mirror.*

Photoluminescence (PL)

PL spectroscopy[80] is a non-destructive method, based on the detection of radiative recombination processes originating from optically generated electron-hole pairs. From the spectral position and the width of the PL peaks one can derive the composition (Al-content x) of a ternary semiconductor compound like AlGaAs, and obtain information on its quality (concentration of dopants and defects).

A PL setup has been built from a Nitrogen trap. The cryostat, which provides temperatures between 100 and 350 K with a 0.1 K stability, can be used as a sample holder for nonlinear reflectivity measurements (cf Section 3.1.2).

The use of PL to calibrate thickness variations across a wafer is described in Section 3.2.1. Figure 3.3 shows a PL spectrum of the quantum well sample, where the observed peak energies[81] were used to determine the well widths.

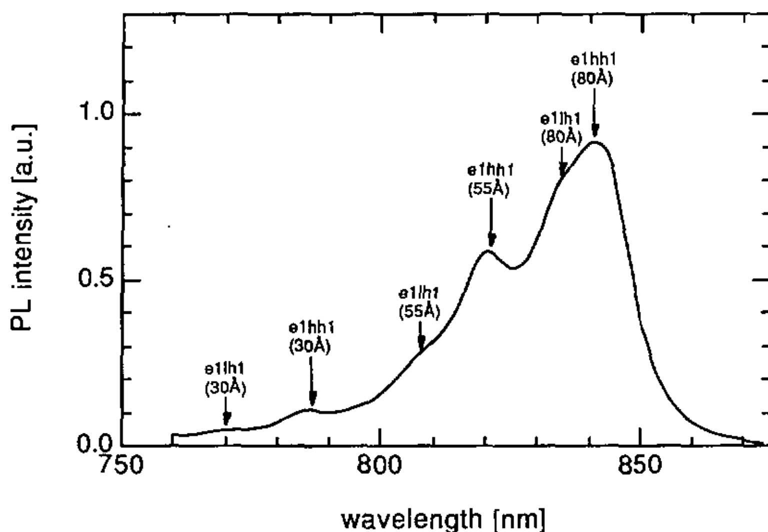

Fig. 3.3: Liquid nitrogen PL spectrum of sample #302: the three peaks correspond to the heavy hole transition (e1hh1) of 80, 55 and 30 Å thick GaAs wells (between $Al_{.35}Ga_{.65}As$ barriers). The corresponding bumps on the high energy sides mark the light hole transitions (e1lh1).

Electrical measurements (C-V, I-V, PC)

All Fabry-Perot structures were grown as pin-diodes to provide the possibility for electrical tuning by applying a reverse bias across the intrinsic spacer layer. The front and rear mirrors were doped with Be (p) and Si (n), respectively, with doping concentration increasing from 10^{17} cm^{-3} to 10^{18} cm^{-3} outwards.

To verify the doping concentrations and the electrical characteristics of the diode, electrical contacts have been evaporated on a part of sample #337 (AuGe on the n-type substrate and AuZn on the p-type front mirror). The current-voltage characteristic (I-V) of the diode indicate a series resistance of 1.6 Ωcm^2. Measurements of the diode capacity vs a bias voltage (C-V characteristic), interpreted with an abrupt junction model[82], suggest doping concentrations of $7 \cdot 10^{16}$ cm^{-3} and 10^{15} cm^{-3} for the mirrors and the spacer, respectively. Photocurrent measurements (PC) with a transparent p-contact (Indium-Tin-Oxide) indicate that the spacer is not completely depleted. A scan of the photocurrent collected by a Platinum contact for different spot positions (Fig. 3.4) indicates a good homogeneity of the intrinsic region.

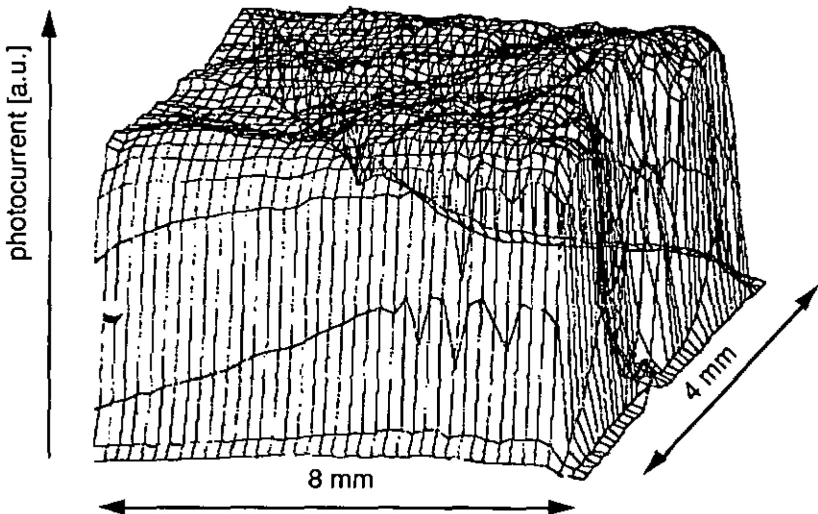

Fig. 3.4: Photocurrent as a function of the spot position on sample #360. The current is collected by a Pt contact which causes the dip on the right.

Spectral reflectivity measurements (SRM)

SRM are essential for the work with reflective nonlinear optical devices, because it allows one to determine the relevant optical properties, such as the wavelength and the reflectivity at the Fabry-Perot resonance. Two different setups have been used for the characterization of samples and devices:

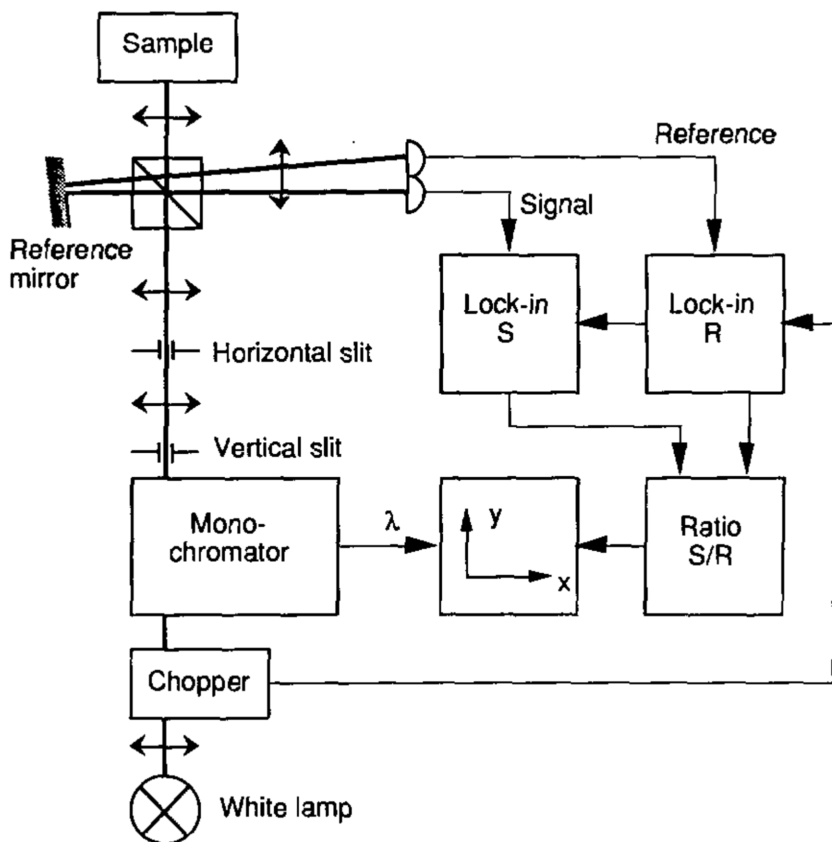

Fig. 3.5 *Incoherent, room temperature SRM system (EPFL): A chopped monochromator light source ($\lambda = 0.6$–$1.2\ \mu m$) is imaged onto the sample. Light reflected from the sample and from a reference mirror is detected synchronously by a double pin-diode which is connected to a two-channel lock-in amplifier.*

The incoherent SRM setup existing at EPFL sketched in Fig. 3.5 is equipped with a monochromator source. It therefore has a wide spectral range and a high absolute

wavelength accuracy. The resulting spectra are used to judge the overall spectral properties of grown samples, and to calibrate optical thicknesses. The spectral resolution is limited to about 1 nm by the low signal power and the large imaged spot of about 100 µm diameter. It is not sufficient to resolve high finesse FP resonances to verify the impedance matching condition.

The setup described below is a complementary tool, if its coherent source is used at weak power levels. It provides diffraction limited spots, a spectral resolution better than 0.1 nm together with a SNR of 25 dB, and the Peltier sample holder allows temperature control between 0° and 50° C, stable to less than 1 K. On the other hand, this setup has a narrower wavelength range (800–900 nm) and suffers from undesired interference effects.

3.1.2 Setup for nonlinear reflectivity measurements

The experimental setup described in the following has been developed by the author at the Institut de Microtechnique (IMT) in Neuchâtel.

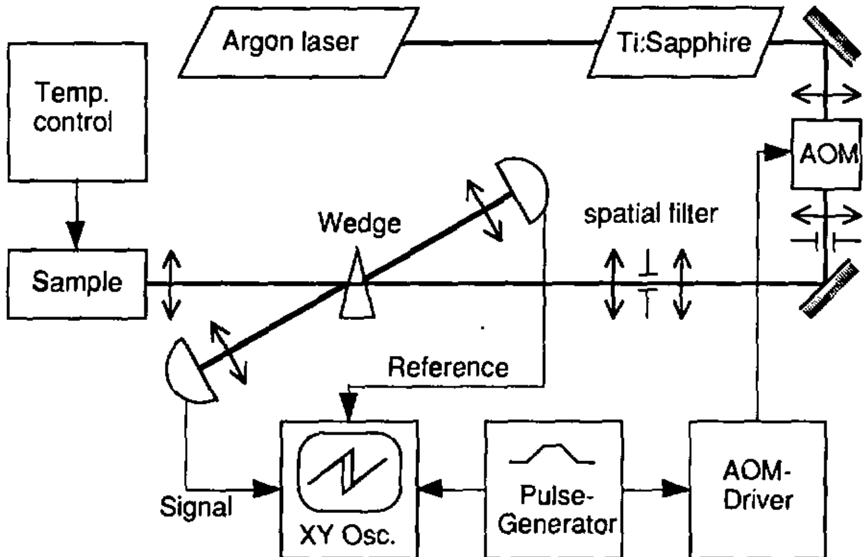

Fig. 3.6: Experimental setup for nonlinear reflectivity measurements (IMT).

To study nonlinear reflectivity changes on AlGaAs samples, one requires a setup for reflectivity measurements with variable optical intensities up to a few mW/μm^2. The wavelength should be adjustable in the vicinity of the gap of the nonlinear material used (870 nm for GaAs, Eq. 2-42). Pulses of μs duration and a low duty cycle (1:100) are recommended to avoid thermal effects in the sample[42]. The setup was built with these requirements and it is sketched in Fig. 3.6. Its principal parts are described below.

Light source

Initially the source was an Argon-pumped dye laser (Coherent CR-599) used with Styril 9M dye. When frequently adjusted it delivered a power of less than 100 mW at 880 nm. In addition, its broadband intensity noise (≈ 10%) restricted threshold measurements and made narrow band detection necessary. The recent acquisition of a Titanium-Sapphire laser (Coherent CR-899) represents a major improvement in power (≥ 0.5 W), wavelength range (780 to 950 nm), noise (≤ 3%) and low maintenance. The laser has been equipped with a stepper-motor to allow computer-controlled wavelength tuning in 0.2 Å steps.

Pulse generation

The optical pulses are generated by an acoustooptic modulator (Automates et Automatismes MP-10) with a carrier frequency of 200 MHz which is driven by a 50 MHz pulse generator (Phillips PM 5715) at a typical repetition rate of 10 kHz and a pulse duration of ≈ 1 μs. Used in a telescopic setup with two f = 60 mm lenses, the acoustooptic modulator provides rectangular pulses with less than 15 ns rise time. The efficiency in the first diffraction order is about 70% with a zero-order suppression of 30 dB.

Beam focusing and spectral resolution

A spatial filter unit is inserted after the modulator to produce a collimated Gaussian beam which is focused onto the sample by a 10x microscope objective. The Gaussian spot on the sample has a typical beam waist $w_0 \approx 3$ μm which has been determined by measuring the far field diffraction angle θ_i.

The sample is placed into the beam focus by a manual control of the sample holder along the optical axis. For bistable samples, this position is characterized by a minimum threshold power (cf Sect. 3.5.7), otherwise one has to observe the reflected beam.

The spectral resolution of the system is limited by the dependence of the FP-resonance wavelength on the angle of incidence. According to Eq. 2-10 the resolution for a diffraction limited Gaussian spot ($w_0 = \lambda/\pi\theta_i$) is $\Delta\lambda/\lambda \approx (\lambda/\pi w_0 n)^2/2$ (cf Eq. 4-9). This corresponds to $\Delta\lambda = 0.3$ nm for the typical spot diameter $2w_0 = 6$ µm used. The resolution can be improved to ≈ 0.05 nm by enlarging the spot diameter to ≈ 15 µm. For larger spot diameters the observed resolution is limited by the surface inhomogeneity.

Sample holder

The sample is placed on a 3 W Peltier cooler with which the sample temperature can be controlled between 0 and 55 °C with a stability better than 1 K. This Peltier support is fixed to a computer-controlled x-y table, to position the sample with respect to the spot with a repositioning accuracy ≤ 5 µm. A wider temperature range from −170 to +170 °C (stability 0.1 K) is available with a home built N_2-cryostat.

Signal detection

A reference and a signal beam are reflected off an uncoated 2° glass-wedge between the spatial filter and the microscope objective. These beams are focused on two fast pin-diodes equipped with AC transimpedance amplifiers (Analog Modules 712A-3-B) which have a sensitivity of 40 V/mW and a bandwidth of 40 MHz at a bias voltage of 60 V.

If not otherwise stated, the entire reflected beam profile, including the light defocused by the nonlinearity, is detected. By detecting only the central part of the reflected beam (vignetting) the switching contrast of nonlinear devices can be increased considerably (cf Fig. 3.27).

Power calibration

The reference detector is calibrated to the optical power incident on the sample. A sensitivity of 2.92±0.03 V/mW for the wavelength range of 880±10 nm has been determined by calibrating its response to a sinusoidal incident intensity with a photodiode (UDT 260) at the sample position. The reflectivity can be calibrated to ≈ 1% accuracy, by using an uncoated gold mirror as a reference (Balzers, R ≥ 98% at λ ≥ 870 nm).

Dynamic switching measurements

To study dynamic device properties, the incident and reflected signals are monitored on a digitizing sampling oscilloscope (HP 54504: 400 MHz, 200 MS/s). Trapezoidal incident pulses of 1 µs duration and 100 ns transition times are typically used at a repetition frequency of 10 kHz. Maximum intensities up to 10 mW/μm^2 can be achieved (300 mW peak power on a 6 µm spotsize).

Nonlinear reflectivity spectra

Spectral reflectivity measurements (SRM) at variable incident intensities can be measured by synchronous detection of the pulsed signal and reference. To this goal, the outputs of the AC-detectors are fed through two lock-in amplifiers (Stanford Research SR530) and digitized by a data acquisition card (Metrabyte DASH-16G). The laser wavelength and the data acquisition are controlled by an acquisition program on a personal computer.

To minimize heating, pulses of 1 µs duration at 10 kHz repetition rate are used[83]. The transient contributions in nonlinear devices (before and after switching) are reduced by using square pulses with 20 ns transitions. The detector signals have to be attenuated (by 20 to 30 dB) to avoid nonlinear distortions due to the limited slew rates of the lock-in amplifiers.

Linear reflectivity spectra are measured with the same synchronous technique at small incident intensity, using less than 50 µW peak power (spot: $2w_0 \approx 6$ µm). A typical SNR of 25 dB results from averaging (of signal/reference ratios to eliminate the correlated noise) over about 0.2 s.

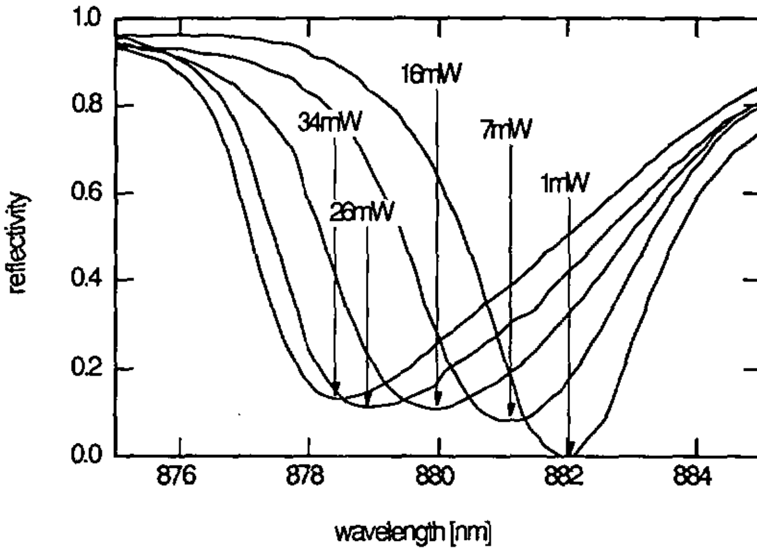

Fig. 3.7 *Reflectivity spectra (#337) measured at different levels of the incident peak power (cf Sect. 3.4).*

Limitations and improvements

The above method allows one to visualize the impact of the pump intensity on the reflectivity spectrum (Fig. 3.7). For bistable devices, only the upper part of the hysteresis loop is accessible with this method. However, the lower part could be measured with two-level pulse technique which has recently been proposed[83]. The noise in the reflectivity spectra is dominated by interference effects due to the coherent illumination.

Measurements close to the threshold of a nonlinear device are limited by the intensity noise in the laser source, which is below 3% with the Titanium-Sapphire laser without active stabilization. In particular, this noise limits the measurement of critical slowing down (cf Sect. 3.5.4) and of device gain (cf Sect. 3.5.8).

3.2 Thickness calibration for MBE growth

The precision requirements for the thickness of a NLFP spacer layer are very demanding (0.5%). This has stimulated a considerable effort to characterize and improve the thickness accuracy of epitaxial layers. The following two examples illustrate the progress achieved.

3.2.1 Thickness variations on the wafer surface

Initially, the accuracy of the MBE (1–2 %) was not sufficient to assure the precision required. The tolerance has, therefore, been increased by making use of the thickness variations across the wafer: the spacers of the first two NLFP samples (#337 and #360) were deliberately grown as wedges, by stopping the wafer rotation during a fraction of the growth process. To determine this fraction, the thickness variations were first measured on an unrotated wafer with three quantum wells (#302). Assuming a constant Al concentration, the thickness of a quantum well can be determined by photoluminescence measurements (Fig. 3.3), because the electronic levels depend strongly on the well width[81].

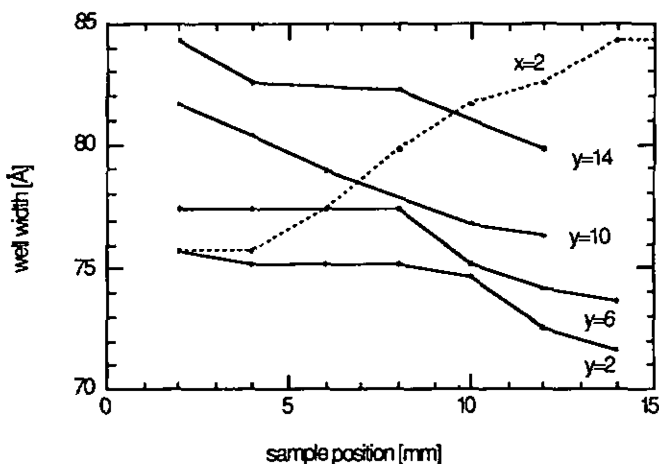

Fig. 3.8: *Thickness variations across the wafer #302 (solid lines correspond to constant abscissa values y = 2, 6,10, and 14 mm; the dotted line to an ordinate x = 2 mm). The well width has been determined from the photoluminescence of the e1hh1 transition in the 80 Å well.*

The thickness varied by about 10% over a distance of 12 mm along the wedge gradient of the sample (x=2 in Fig. 3.8). Thus, stopping the sample rotation during 10% of the growth time, would lead to the desired 1 to 2% variation of the NLFP spacer thickness.

For comparison, Fig. 3.9 shows two images of the surface of the wafer #386 taken at wavelengths of 885 nm and 880 nm. The dark fringes identify impedance matched resonances at a given wavelength. Their different locations on the wafer indicate a change of the spacer thickness by 0.7%. This sample was grown with sample rotation, after the optical calibration step described below. The thickness error at the wafer center is less than 0.5%, and the thickness varies less than 1% on a disk of 24 mm diameter.

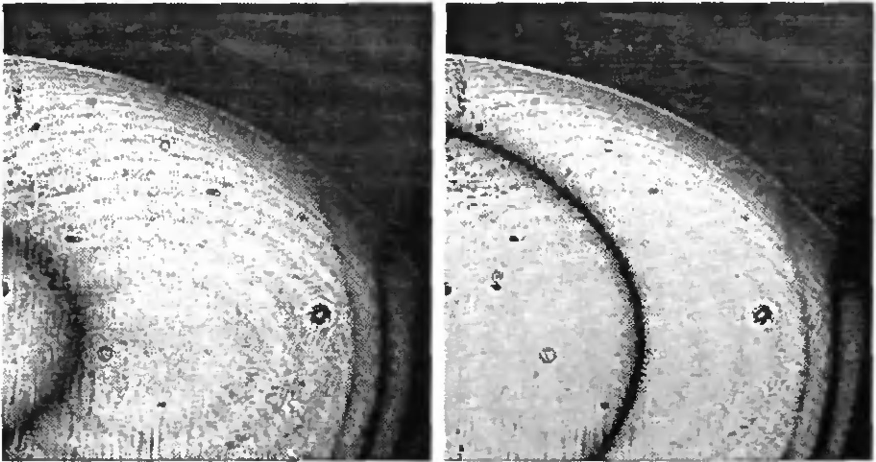

Fig. 3.9: Manochromatic images of the wafer surface (about 1x1 inch on #386) at two wavelengths, 885 nm (left) and 880 nm (right) show the FP resonance as dark lines.

3.2.2 Absolute thickness calibration

RHEED

During the molecular beam epitaxy process, growth rates are measured with RHEED (reflective high energy electron diffraction), which allows one to monitor the deposition of one monolayer. Slow flux variations however, have to be corrected by calibrating the effective growth rates with post-growth characterization methods. Clearly, the best results are obtained if the calibration data stems from a wafer of the same charge.

TEM

Transmission electron microscopy (TEM), which was initially used for this purpose turned out to be inappropriate for an absolute calibration, due to a typical uncertainty of about 5% in the magnification factor (which could be improved by a more precise calibration).

XRD

The accuracy and ready availability of the X-ray diffraction system (XRD), which is available at EPFL, suggests its use for calibration based on periodic structures like Bragg mirrors.

SRM

Two reasons favor the use of spectral reflectivity measurements (SRM) for the calibration of optical devices: the high accuracy ($\approx 10^{-4}$) inherent to optical wavelength measurements, and the possibility to directly measure optical path rather than physical distance, which eliminates inaccuracies in the refractive index data (typically $\leq 0.3\%$).

The success of an optical calibration step with a rapid feedback to the growth facility is manifested by the thickness accuracy of better than 0.5% which has been realized in sample #386. The samples #386 to #389 benefited from SRM characterization of sample #380, which consists of a 2 μm thick AlAs layer on a GaAs substrate. By identifying the order of the sinusoidal FP-interferences, the optical path (layer thickness times refractive index) could be derived with nanometer precision. The determination of the absolute layer thickness is thus limited only by the available refractive index data.

3.3 Post-growth device adjustments

The modification of existing samples by processing circumvents exacting precision requirements and the limited availability of samples. The first subsection describes a reactive ion etching technique which has been used to adjust the front mirror reflectivity to the impedance matching condition (samples #212, #224), and to reduce the spacer thickness in order to adjust the resonance wavelength (sample #320). On the latter sample, an impedance matched front mirror has been deposited, which is summarized in Sect. 3.3.2. The third subsection discusses the tuning capability provided by temperature control.

3.3.1 Adjustment by etching

Reactive ion etching (RIE) was used in the following experiments. This technique was preferred to wet etching or anodization for its superior surface quality. Ar and CCl_2F_2 at a pressure of 10 mTorr were used as reactive gases. The etching process was monitored by measuring the reflection of a He-Ne laser beam by the sample.

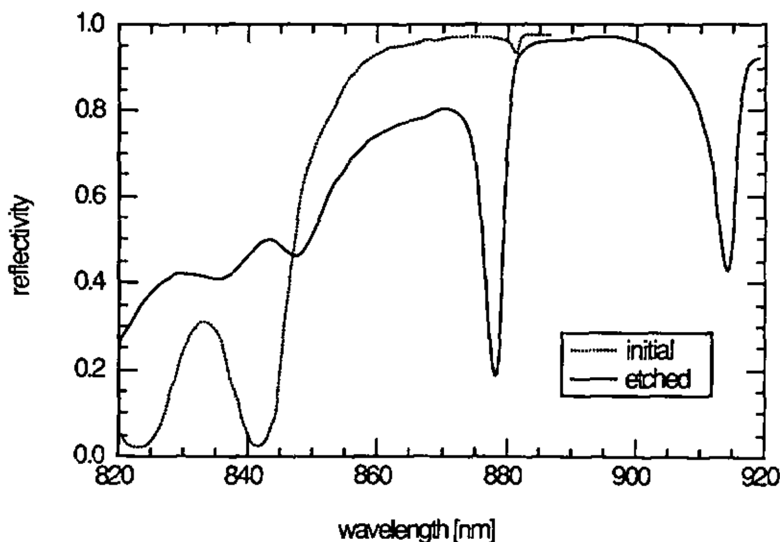

Fig. 3.10: Low intensity reflectivity spectrum of sample #212, before and after etching the front mirror from 20 to 5 layer pairs.

Reduction of mirror reflectivity

Sample #212 is a vertical cavity surface emitting laser (VCSEL) structure composed of a 1.5 μm spacer sandwiched between two dielectric mirrors with 20 layer pairs. The reflectivity spectrum (dotted in Fig. 3.10) shows the weak Fabry-Perot resonance, at 881 nm, in the center of the stopband of the front mirror.

To satisfy the impedance matching condition (Eq. 2-13) at this wavelength, the reflectivity of the front mirror has been reduced to 75% by etching it down to 5 dielectric layers. The dielectric interfaces appear clearly on the monitored reflection signal, which gives control over the progress of the etching process. The average etching speed through the dielectric stack was 40 nm/min. The etching was stopped towards the end of an AlAs layer. The remaining AlAs oxidizes in contact with the air and should, because of the low refractive index of the oxide, have a small impact on the mirror reflectivity.

After the etching process, the contrast ratio of the resonance has improved to 5:1 (solid line in Fig. 3.10). The shift to shorter wavelength is due to the reduced equivalent thickness (Eq. 2-81) of the etched front mirror. The resonance width of 2 nm is proof of the good quality of the etched surface.

Nonlinear measurements showed resonance shifts of −2 nm at intensities of 0.15 mW/μm^2. Bistability, however, was not achieved. Attempts to improve the low finesse ($\mathcal{F} \approx 10$) of the cavity by reducing the temperature (cf Sect. 3.2.3) did not succeed. Similar results were obtained on sample #224, where the front mirror has been etched from 17 to 5 layer pairs. In that case a resonance closer to the gap lead to an even smaller finesse. The failure to observe bistable operation in these samples is attributed to their low finesse. This is mainly due to the high absorption at operating wavelengths close to the bandgap. In addition, large scattering losses (≈2%) were measured in the Bragg mirrors[84], which may be related to the additional interfaces in the superlattice high-index layers.

Reduction of spacer thickness

Sample #320 is another VCSEL structure which had been grown without a front mirror. The spacer consists of a 0.9 μm GaAs layer between two $Al_{0.15}Ga_{0.85}As$ layers of 0.5 and 1.0 μm thickness. The broad FP-resonance originating from the 30% reflection at the front interface to air was originally located around 890 nm (dotted line in Fig. 3.11). By applying the above RIE technique to the spacer layer the resonance has been shifted to 885 nm. The necessary etching depth of 27 nm

was obtained from simulations. It corresponds to an etching time of 40 s according to the etching speed of 40 nm/min.

This method allows to adjust the resonance wavelength of a FP with nm precision, provided an appropriate mirror can be added subsequently.

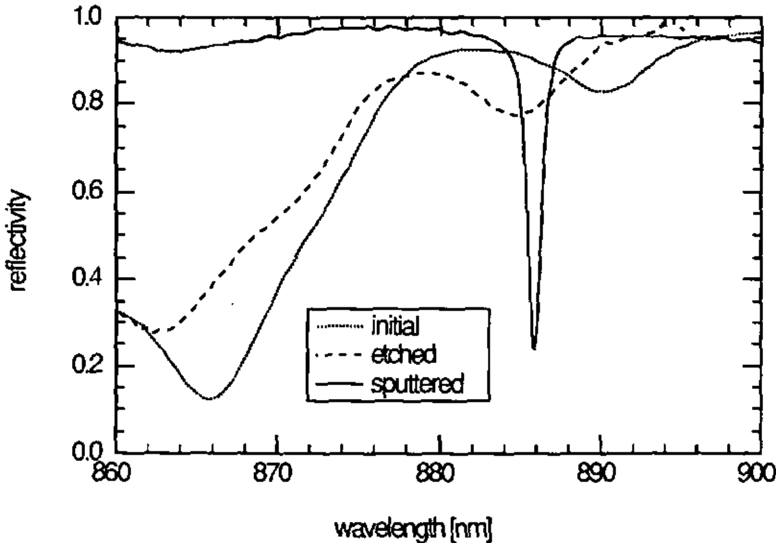

Fig. 3.11 : Low intensity reflectivity spectrum of sample #320 with a resonance at 890 nm (dotted line). After RIE-etching (dashed line) and sputtering (solid line) there is a high contrast resonance at 886 nm.

3.3.2 Sputtered mirror deposition

The reflectivity of the etched spacer (#320) had to be increased to 91% in order to satisfy the impedance matching condition. To this aim, a Bragg mirror consisting of 3 pairs of SiO_2 ($n_L = 1.5$) and TiO_2 ($n_H = 2.3$) layers has been deposited on the spacer by a sputtering technique[85]. The resulting sample showed a contrasted resonance at the appropriate wavelength (solid line in Fig. 3.11). Unfortunately, this mirror did not adhere well to the etched surface and came off before the nonlinear measurements were performed.

3.3.3 Tuning by temperature control

Absorption change

The temperature dependence of the band gap energy of GaAs (Eq. 2-42) gives control of the absorption coefficient. Roughly, the temperature induced change corresponds to a rigid shift of the absorption spectrum by $\partial\lambda_g/\partial T \approx 0.25$ nm/K. Within the bandtail (Eq. 2-43), this shift leads to an increase of the relative linear absorption with temperature

$$\frac{1}{\alpha}\frac{\partial\alpha}{\partial T} = \frac{1}{\alpha}\frac{\partial\alpha}{\partial E}\left(\frac{-\partial E_g}{\partial T}\right) \approx +\frac{7\%}{K}. \tag{3-1}$$

Refractive index change

Assuming that the temperature induced change of the bandgap energy $E_g(T)$ leads to the same shift of the refractive index spectrum in Fig. 2.14, one finds an average thermal index change

$$\frac{\partial n}{\partial T} = \frac{\partial n}{\partial E}\left(\frac{-\partial E_g}{\partial T}\right) \approx +\frac{2\cdot 10^{-4}}{K}, \tag{3-2}$$

based on the average dispersion $(E/n)\cdot\partial n/\partial E = 0.2$. Close to the bandgap energy however, the index dispersion is strongly enhanced ($E/n\partial n/\partial E \approx 0.8$), so that the thermal index change may approach 10^{-3} K^{-1}.

Resonance shift

A change of the refractive index Δn in the spacer causes a wavelength shift $\Delta\lambda_r$ of the Fabry-Perot resonance λ_r ($\varphi[n,\lambda_r] = q\pi$ constant)

$$\frac{\Delta\lambda_r}{\lambda_r} = \frac{L}{L_{eff}}\frac{\Delta n}{n}. \tag{3-3}$$

The proportionality factor accounts for the total phase dispersion in the cavity, which is described by the effective spacer thickness L_{eff} (Eq. 2-88).

The shift of the resonance wavelength λ_r, due to a temperature change, is parallel to the shift of the absorption spectrum, and therefore the effective absorption change at the resonance is reduced. A shift $\partial\lambda_r/\partial T = 0.17$ nm/K has been measured

on the etched sample #212. This compensates 70% of the bandgap shift, and suggests a thermal index change $\partial n/\partial T = 9.4 \cdot 10^{-4}\ K^{-1}$. (This sample exhibits thermal bistability at an incident power of 30 mW and a temperature rise of about 10 K was estimated from a critical detuning $\Delta\lambda \approx 2$ nm.)

Temperature tuning is thus appropriate to adjust the absorption in a nonlinear device. In resonant cavities however, the effective absorption change is reduced by a concomitant resonance shift due to the thermal index change. In the range of interest (bandtail), the wavelength shift due to this refractive effect may amount up to 70% of the absorptive shift.

3.3.4 Conclusion

If the precision requirements of NLFP devices cannot be satisfied with MBE grown integrated structures, a three step procedure could be used to fabricate devices with the correct resonance wavelength λ_r:

1) MBE growth of a highly reflecting mirror with a spacer layer on top.

2) Possibly RIE etching of the spacer to adjust the resonance wavelength.

3) Sputtered deposition of an impedance matched front mirror of TiO_2/SiO_2.

Two methods to adjust the dissipative cavity parameters to the impedance matching condition have been explored: the number of stacks in the front mirror, and thus its reflectivity, can be adjusted by RIE etching, without a penalty in the mirror quality. On the other hand, the absorption in the spacer can be adjusted with temperature control. However, this method is only suited for small adjustments, because the effective absorption change is canceled to a large extent by the thermal refractive effect.

3.4 Nonlinear refractive index measurements

The knowledge of the nonlinear material properties is a prerequisite for device optimization. Nonlinear refractive index measurements were undertaken to compare the nonlinear properties of the material grown at EPFL with the simulation data, and to estimate the influence of index saturation (Sect. 2.1.3).

3.4.1 NLFP sample #337

The first NLFP device (#337) was optimized for a resonance wavelength of 882 nm, based on an absorption coefficient $\alpha \approx 600\ cm^{-1}$ in the GaAs spacer of 2 µm thickness ($16\lambda/2n$). An additional 1% loss in each mirror was presumed from measurements on VCSEL structures[84]. The impedance matching condition (Eq. 2-14) then indicates an ideal front mirror reflectivity of about 75%.
The high index layers with an average Al-content $x_H \approx 18\%$ have been grown as a superlattice of AlAs/GaAs because only one Aluminium source was available in the MBE at that time. Five monolayers of GaAs were included in the low index AlAs layer to improve the surface quality and stability. The exact layout which resulted from numerical optimization is shown in Fig. 3.12.

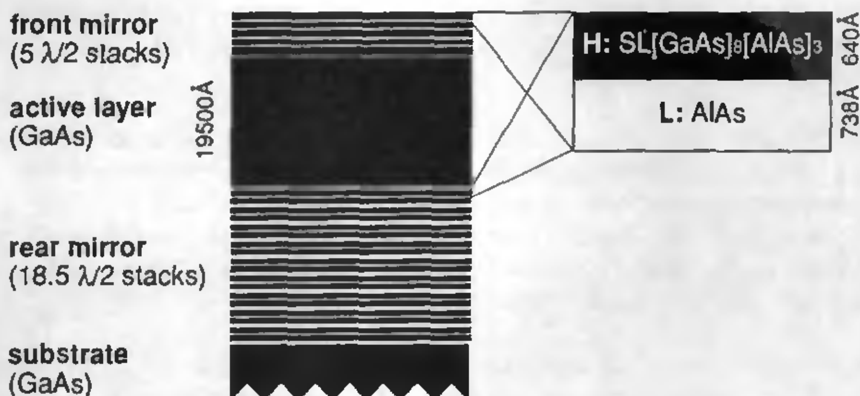

Fig. 3.12: Growth layout of sample #337: NLFP consisting of a 2 µm spacer ($16\lambda/2$ GaAs) between 5 and 19.5 dielectric stacks.

To characterize the rear mirror, the front mirror and the spacer layer were removed by wet etching. A reflectivity spectrum showed that the rear stop band is shifted by about –3% to short wavelengths. The high Al content determined from XRD measurements indicates that this was caused by a low GaAs flux during growth.

This flaw reduces the reflectivity at the FP-resonance to only 90%, and thus limits the achievable finesse of the NLFP to about 10. Typical resonance widths of 3 nm were observed, which could not be improved by cooling the sample to 0 °C. No bistability has been observed, but the device exhibited a strongly nonlinear characteristic with reflection changes of 5 to 1 at an incident power of 5 mW.

3.4.2 Nonlinear index change measurements

Nonlinear refractive index changes in the spacer of a NLFP can be derived directly from the shift of the resonance wavelength in the nonlinear reflectivity spectra[86]. In these measurements the carriers were generated with a pump beam of high energy (1.51 eV) which is pulsed to reduce undesired temperature effects. The resonance shifts was observed in the photoluminescence from the spacer. Recently, a method based on nonlinear reflectivity spectra such as Fig. 3.7 has been proposed[42]. This single wavelength method is closer to actual operating conditions, namely because nonlinear changes of the absorption α are considered in this way. Compared to the measurements which used a bistable MQW sample[42], the lack of hysteresis on sample #337 (Fig. 3.7) simplifies the interpretation of the spectra.

A refractive index change Δn in the spacer leads to a shift of the resonance wavelength $\Delta\lambda_r$ as described by Eq. 3-3. This relation permits the determination of nonlinear refractive index changes to better than 10% accuracy, limited by the knowledge of the local index dispersion. Fig. 3.13 shows the nonlinear index change as a function of the incident power, measured at three different positions on sample #337 with a spot of diameter $2w_0 = 5.2\ \mu m$.

The magnitude and the wavelength dependence of the observed index change agree well with the experimental data used in the simulations (Fig. 2.16). The maximum nonlinear shift $\Delta\lambda = 3.5$ nm observed for the resonance at 882 nm at an incident power of 35 mW corresponds to an index change $\Delta n = 2.5 \cdot 10^{-2}$. A comparison with the simulation data indicates that this change corresponds to a carrier density of about $10^{18}\ cm^{-3}$, or a nonlinear cross-section $\eta \approx 2.5 \cdot 10^{-20}\ cm^3$.

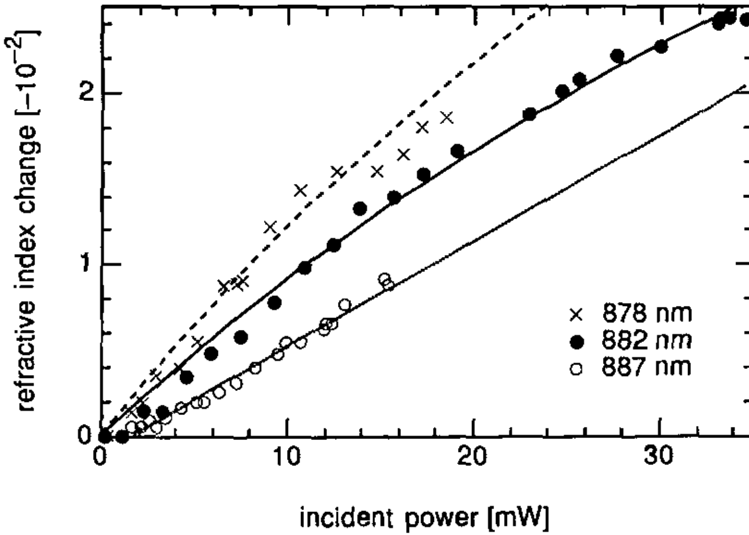

Fig. 3.13: Nonlinear refractive index change in GaAs as a function of the power incident on a spot of diameter $2w_0$ = 5.2 µm on sample #337. The marks correspond to measurements at three wafer positions with resonance wavelengths λ_r = 878, 882 and 887 nm. The lines are fitted according to a saturation model[23].

3.4.3 Evaluation of nonlinear material properties

At the resonance of a high finesse cavity, the average internal intensity I is related to the incident intensity I_i by the cavity finesse $\mathcal{F}$ (Eq. 2-18)

$$I = \frac{2\mathcal{F}}{\pi} I_i \, . \tag{3-4}$$

Phenomenological Kerr-coefficient

Using this relation, a Kerr-type coefficient $n_2 = \partial n/\partial I \approx 2\text{–}4 \cdot 10^{-5}$ cm²/kW has been derived initially[87], assuming an effective spot area πw_0^2. This value is about 10 times smaller than n_2 calculated in the same way from a nonlinear simulation. The discrepancy is due to carrier loss mechanisms: For small spot diameters ($2w_0$ = 5.2 µm) carrier diffusion becomes important (rate equation 2-45).

An investigation of the threshold intensity as a function of the spotsize (cf Sect. 3.5.7) suggests a 7-fold intensity increase for this spotsize, compared to plane wave excitation. Thus, the discrepancy in the Kerr coefficient can be explained by carrier diffusion alone, which indirectly supports the recombination time $\tau = 4$ ns assumed in the simulation. This result is confirmed by a recent measurement with a larger spotsize ($2w_0 = 12\,\mu m$, cf Table 3.2), where the estimated effect of diffusion is reduced to a factor of 3. Both measurements indicate a Kerr coefficient $n_2 = 2 \cdot 10^{-4}\ cm^2/kW$ in the plane wave limit.

material (at wavelength)	$\mathcal{E}-\mathcal{E}_g$ [meV]	α [cm^{-1}]	$\mathcal{F}$	πw_0^2 [μm^2]	$\lvert n_2 \rvert$ [cm^2/kW]	$\lvert n_2 \rvert/\alpha\lambda$ [cm^2/kW]	$\lvert \Delta n \rvert/P_i$ [W^{-1}]	$-\Delta n_s$	I_s [kW/cm^2]
GaAs (878 nm)	−13	1400	13	21	$3.5 \cdot 10^{-5}$	$0.3 \cdot 10^{-3}$	1.4	$7.3 \cdot 10^{-2}$	$2.1 \cdot 10^{3}$
GaAs (882 nm)	−19	490	9	21	$3.6 \cdot 10^{-5}$	$1.6 \cdot 10^{-3}$	1.0	$9.0 \cdot 10^{-2}$	$2.5 \cdot 10^{3}$
GaAs (882 nm, Ti:Al_2O_3)	−19	490	15	113	$7.4 \cdot 10^{-5}$	$3.2 \cdot 10^{-3}$	0.71	$3.9 \cdot 10^{-2}$	$0.60 \cdot 10^{3}$
GaAs (887 nm)	−27	130	11	21	$2.0 \cdot 10^{-5}$	$1.7 \cdot 10^{-3}$	0.62	-	-
GaAs MQW (838 nm)	−27	120	36	82	$8.6 \cdot 10^{-5}$	$8.6 \cdot 10^{-3}$	1.9	$2.4 \cdot 10^{-2}$	$0.25 \cdot 10^{3}$

Table 3.2: Comparison of nonlinear refractive index measurements at different wavelengths λ in GaAs (sample #337) and in GaAs-MQW[42]: $\mathcal{E}-\mathcal{E}_g$ is the detuning from the bandgap and α is the estimated absorption thereat. $\mathcal{F}$ is the finesse, and πw_0^2 the illuminated spot area. The phenomenological Kerr coefficient n_2 is given as such, and normalized to $\alpha\lambda$. The index change per incident power $\Delta n/P_i$ is related to the cross-section η, and Δn_s, I_s are fitted saturation values.

Because of this uncertainty in the diffusion (and recombination) mechanisms, this method is not suited to collect nonlinear index data $n(\omega,N)$ for simulations. The carrier recombination time and diffusion length of a material should be either determined by other means, or eliminated using short pulses and a large spotsize.

Nonlinear cross-section

The nonlinear cross-section η can be estimated directly from the incident power, because for an impedance matched resonance the reflected and the transmitted power (≤4%) can be neglected. The ratio $\Delta n/P_i$ is the index change created by an absorbed power P_i. If the effectively excited volume V_{eff} is estimated to be 7 times larger (cf Sect. 3.5.7) than the product of spot size and spacer length L, the nonlinear cross-section η is (at 882 nm)

$$\eta \approx V_{eff} \frac{\Delta n}{P_i} \frac{\hbar\omega}{\tau} \approx 2 \cdot 10^{-20}\ cm^3 . \qquad (3\text{-}5)$$

Considering the arbitrariness of the selected spotsize (πw_0^2), the agreement with $\eta \approx 2.5 \cdot 10^{-20}$ cm^3 estimated from the simulation data[39] is rather incidental.

3.4.4 Saturation behavior

The nonlinear index data obtained as a function of the cavity intensity has been fitted to the phenomenological saturation model of Eq. 2-28. Table 3.2 shows the saturation values Δn_s, I_s and the low intensity Kerr coefficient $n_2 = \Delta n_s / I_s$ obtained for GaAs at different energies, as well as a similarly obtained result for a quantum well sample[42], where the spacer consists of 130 GaAs wells of 10 nm thickness.

Due to the limited power of the dye laser, there is only small evidence for index saturation in the early measurements on GaAs (Fig. 3.13). However, a recent measurement (bold in Table 3.2), using the higher power of the Ti:Al_2O_3 laser and a larger spotsize ($2w_0$ = 12 μm), shows clear saturation with a realistic value Δn_s = 0.039 for the saturating index change at a wavelength of 882 nm. The saturation value, and also the largest observed index change in GaAs ($\Delta n \leq 0.024$), are about twice larger than in the MQW sample ($\Delta n \leq 0.011$). On the other hand, the low intensity Kerr coefficient $n_2/\alpha\lambda$ and $\Delta n / P_i$ favor the MQW material.

3.4.5 Conclusion

Nonlinear refractive index changes have been derived from the resonance shift observed in nonlinear spectra (Fig. 3.7). For the small spots used, the resulting Kerr coefficient n_2 and the nonlinear cross-section η are considerably reduced by transverse carrier diffusion. Asymptotic plane wave values $n_2 \approx 2 \cdot 10^4$ cm^2/kW and $\eta \approx 2 \cdot 10^{-20}$ cm^3 result, if spotsize dependent measurements (Sect. 3.5.7) are taken into account. These values agree with the simulation model, assuming a carrier recombination time of 4 ns. To determine nonlinear refractive index data with this method, the carrier loss mechanisms have to be determined by independent measurements or avoided by fast measurements (sub-ns) and large spotsizes.

The presence of refractive index saturation could only be confirmed recently, thanks to the higher power available with the Titanium-Sapphire laser. The obtained saturation value $|\Delta n_s| \approx 0.039$, as well as the maximum $|\Delta n| = 0.025$ measured, are larger than corresponding values $|\Delta n_s| \approx 0.024$, and $|\Delta n| \approx 0.011$ reported for MQW material[42]. On the other hand, the nonlinear coefficients n_2 and

$\Delta n/P_i \propto \eta\tau$ at low intensities are larger in MQW material. An estimation of critical intensities $I^c = \Delta n^c/n_2 \geq (1/\pi\sqrt{3})/(n_2/\alpha\lambda)$ according to Eq. 2-18 gives $I^c = 0.1$–$0.5\ I_s$, in agreement with the observed threshold intensities (≈ 100 kW/cm^2 in the cavity). Thus, the above observations do not favor one material clearly. Still, the larger achievable index change in bulk material is an advantage for operation close to saturation, as was the case in most of the investigated samples.

The saturation value Δn_s indicates a critical finesse $\mathcal{F}^c \approx 11$ which would be required for bistability in a 2 μm device (Eq. 2-30). This may explain why bistability was not observed in the early samples (#212–#337) with finesse values around 10.

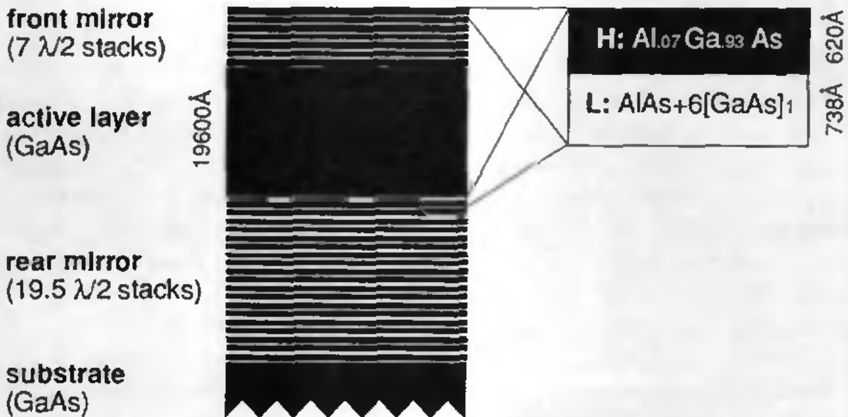

Fig. 3.14: Growth layout of samples #352 and 360: NLFP with 2 mm spacer (16l/2 GaAs) between 7 and 20 dielectric stacks.

3.5 Bistable switching

Optical bistability at a low threshold has been observed in the second NLFP design (#360). First, the modifications made in this design and the spectral properties of the sample are introduced. Then, the nonlinear switching properties of this device are described. In particular, the dependence of the threshold power and time characteristics on the operating parameters such as wavelength and spotsize, have been studied.

3.5.1 Layout of NLFP sample #360

The early NLFP samples (the modified #212, #224, and #337) have been optimized for a resonance wavelength around 882 nm, assuming a comparatively large absorption ($\alpha \approx 600\ cm^{-1}$) in the spacer and scattering losses ($\approx$1%) in the Bragg reflectors[84]. The resulting impedance matched cavities ($R_f \approx 0.75$) had a theoretical finesse of about 11, which was often further restricted by growth inaccuracies (Table 3.1). This corresponds to just about the critical finesse required from the saturating index change (Eq. 2-30, Sect. 3.4), which is a reason for the failure to observe bistability on these samples.

For the Bragg reflectors, the spectral position of the stopband is more problematic than initially expected. Also, the superlattice interfaces in the high index layers, may be the cause for the high scattering losses observed[84].

Improvements

The improved design is shown in Fig. 3.14. The high index layers of the Bragg reflectors consist of $Al_{0.07}Ga_{0.93}As$. The reduced aluminium concentration compared to the sample #337 increases the index step, and thus the width of the stopband and the mirror reflectivity.

The finesse of the NLFP with a 2 μm spacer was increased by choosing a longer resonance wavelength (885 nm). In addition, the 6 dielectric layers in the front mirror suggested by the simulations were increased to 7 in the final design. The front mirror reflectivity was increased to overcome index saturation effects, and to correct the too high absorption assumed in the model. The theoretical reflectivity is $R_f \approx 0.91$ corresponds to an absorption $\alpha = 240\ cm^{-1}$ at impedance matching and a theoretical finesse of 33.

Both samples have been grown as a wedge (Sect. 3.2.1) to improve the tolerance. Fig. 3.15 shows a contour map of the resonances on the wafer surface, obtained by superposing interferometric images (cf Fig. 3.9) at five different wavelengths. The resonance wavelength changes by several nm per mm along the thickness gradient, while perpendicular to the gradient the change is less than 1 nm per mm. The change is less than 2 nm in a disk of 10 mm diameter at the rotation center.

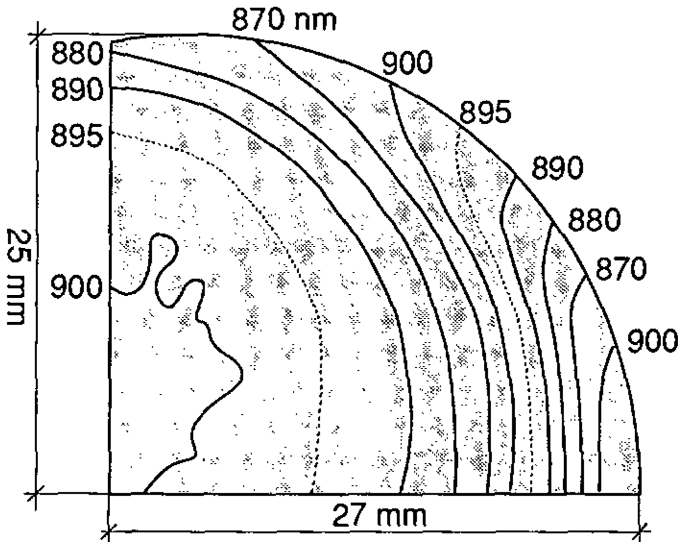

Fig. 3.15: Resonance contours on the wafer #360, at five distinct wavelengths.

3.5.2 Spectral reflectivity properties

Sample #352 had layers which were 10% too thick compared to the design. It also was full of oval defects due to a flux problem during the epitaxial growth. Sample #360 still deviated from the design by up to 5%. The stop band of the rear mirror was shifted so that only the outer parts of the wafer could be used.

Low intensity spectra measured at different positions on the wafer (Fig. 3.16a) show that the impedance matching condition is met at a wavelength of about 883 nm. The non-zero minima are due to the limited resolution ($\approx$ 0.1 nm). Resonances are about 1 nm wide. The free spectral range of 31 nm indicates a finesse in excess of 30.

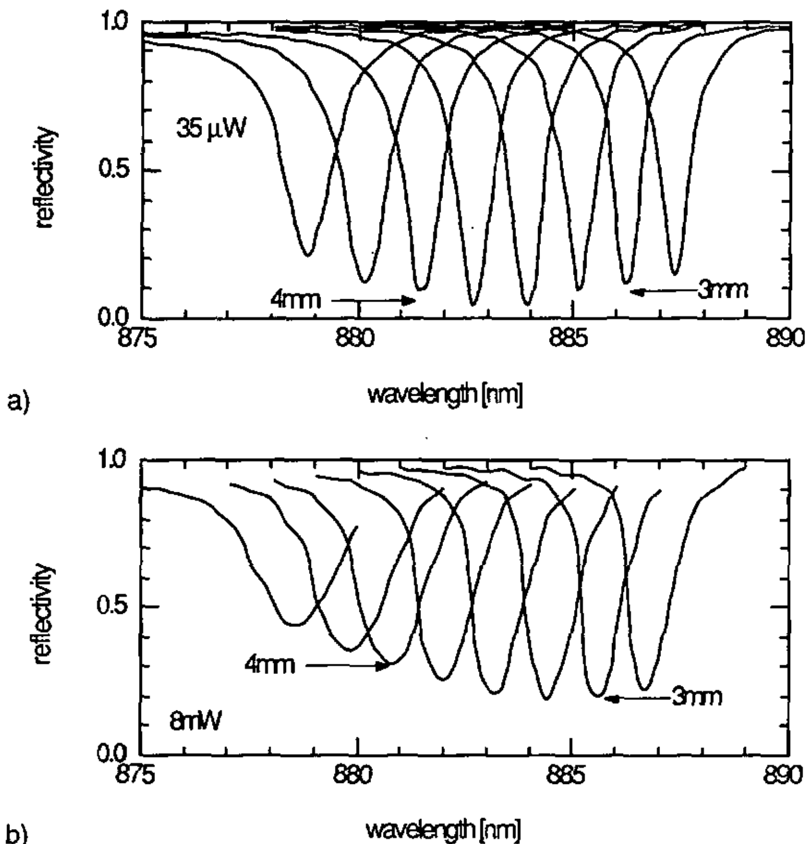

Fig. 3.16: FP-resonances on sample #360: Reflectivity spectra measured at an incident power of a) 35 μW and b) 8 mW with a 30 μm spot diameter at positions separated by 0.25 mm along the thickness gradient of the wafer.

3.5.3 Switching properties

Fig. 3.17 illustrates the bistable switching behavior observed in sample #360. The operating wavelength is about 1 nm shorter than the resonance (initial detuning in Eq. 2-23). A threshold power as low as 1 mW has been measured for a spot of 6 μm diameter. Both switching transitions are faster than 20 ns (detector limit ≈10 ns), if they are not limited by critical slowing down (cf Sect. 3.5.4)

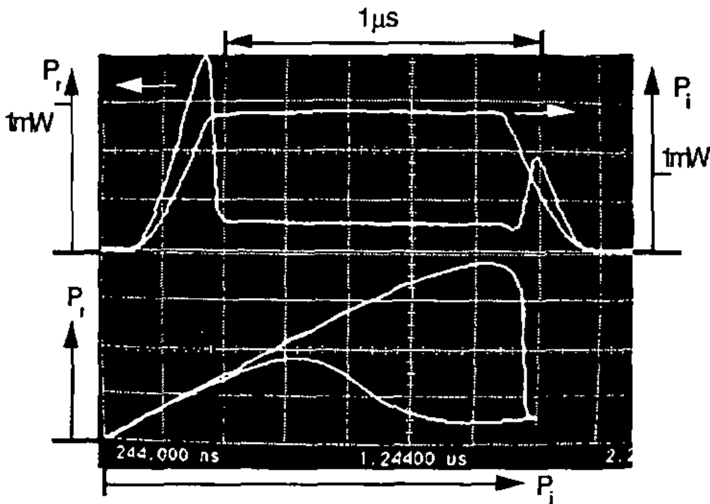

Fig. 3.17: Bistability on sample #360: Incident and reflected power vs. time, and corresponding hysteresis plot (reflected vs incident signal).

Switching contrast is defined as the ratio between the reflectivity before and after switch-ON, R_H^{ON}/R_L^{ON} (Fig. 2.8). Values of 8 have been measured without using spatial filtering.

Absorption increase

The highest contrast and the lowest thresholds are observed at operating wavelengths around 886 nm. This is consistent with the shift of the impedance matching condition to longer wavelengths at higher incident intensity which is observed in Figure 3.16b. The shift of ≈ 2 nm indicates an estimated absorption increase from $\alpha \approx 170\ cm^{-1}$ to $\alpha \approx 240\ cm^{-1}$ at 885 nm. This absorption increase (at carrier densities below $10^{18}\ cm^{-3}$) indicates a dominant contribution from bandgap renormalization, and appears consistent with theory[39]. According to Sect 2.1.3, an absorption increase at low intensities helps the dispersive bistability and thus may contribute to the observed low threshold power.

Threshold criterion

The minimum threshold is characterized by the transition from the nonlinear to the bistable regime (cf Fig. 2.8). However, the existence of two distinct thresholds for switch-OFF and switch-ON, $I_i^{OFF} < I_i^{ON}$ is not an appropriate criterion to classify the variety of hysteresis loops observed, because these are distorted by transient

effects. A more reproducible threshold criterion to determine the minimum threshold is based on the observation of a critically slowed transition between two distinct levels (cf Fig. 3.18).

3.5.4 Critical slowing down

According to theory (Sect. 2.2.3), the duration of a switching transition depends strongly on the amount by which the switching pulse exceeds the threshold power. Figure 3.18 shows the experimental observation of this critical slowing down phenomenon on a NLFP device. In these measurements, the product of transition time and excess pulse power is approximately constant at about 15 pJ. This confirms the predicted switching energy conservation, respectively the pulse area scaling law[49]. The incident switching energy of about 15 pJ indicates an energy of about 5 pJ which is absorbed in the spacer (Eq. 2-48) to generate the critical carrier density (Eq. 2-25). Within the available precision, no divergence of this energy at low excess powers[50,88] could be observed.

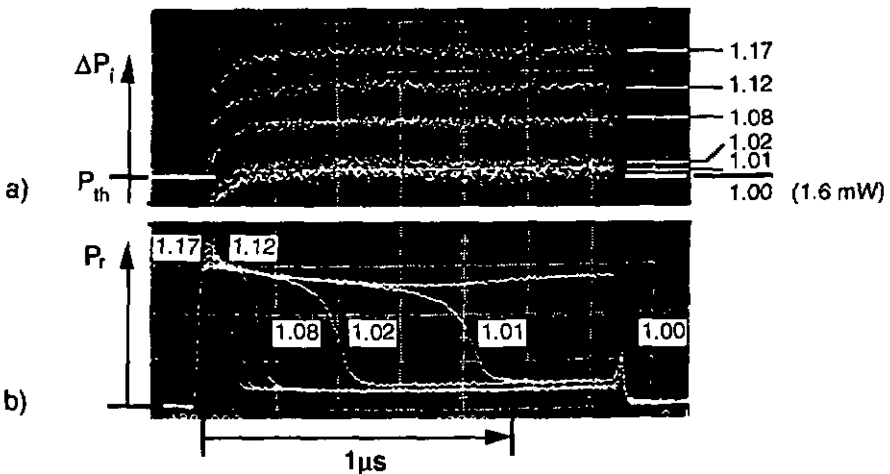

Fig. 3.18: Critical slowing down: a) incident pulses which exceed the threshold of 1.6 mW by 1, 2, 8, 12 and 17%. b) corresponding switching response of the reflected signals.

To provide gain, the device has to be biased close to the switching threshold with a holding beam (cf Sect. 3.5.8). The fraction of this holding power which is dissipated depends on whether the NLFP is in the ON- or OFF-state. Biasing does not, however, reduce the switching energy significantly, because the major nonlinear phase shift occurs during the switching transition (Fig. 2.7). The possibility to lower of the switching energy by reducing the excited spacer volume will be discussed in Sect. 4.1. The switching energy requirement increases the dynamic stability towards fluctuations in the holding beam[89] and thus allows one to operate the device close to threshold. However, in this case critical slowing down at the OFF transition becomes important and limits the operating speed.

3.5.5 Thermally stable switching

The switching in this sample is thermally stable. Fig. 3.19 shows stable, latched switching for more than half a second. No heat sinking other than the 0.5 mm thick GaAs substrate was used. Thermally stable switching has been reported before[90,91]. However, in these demonstrations the substrate of the sample had to be removed to improve the heat sinking.

Several effects may contribute to this improvement. The principal reason is the low threshold power. A simulation for a similar device[63] predicted a temperature rise of 2–3 K for a threshold power of 7 mW, thus a rise less than 1 K is estimated in this device (6 µm spot). In addition, the heat dissipation is favored by the material quality. A relatively low nonradiative recombination rate enhances the radiative recombination. In addition, the operating wavelength far from the bandgap reduces the reabsorption probability.

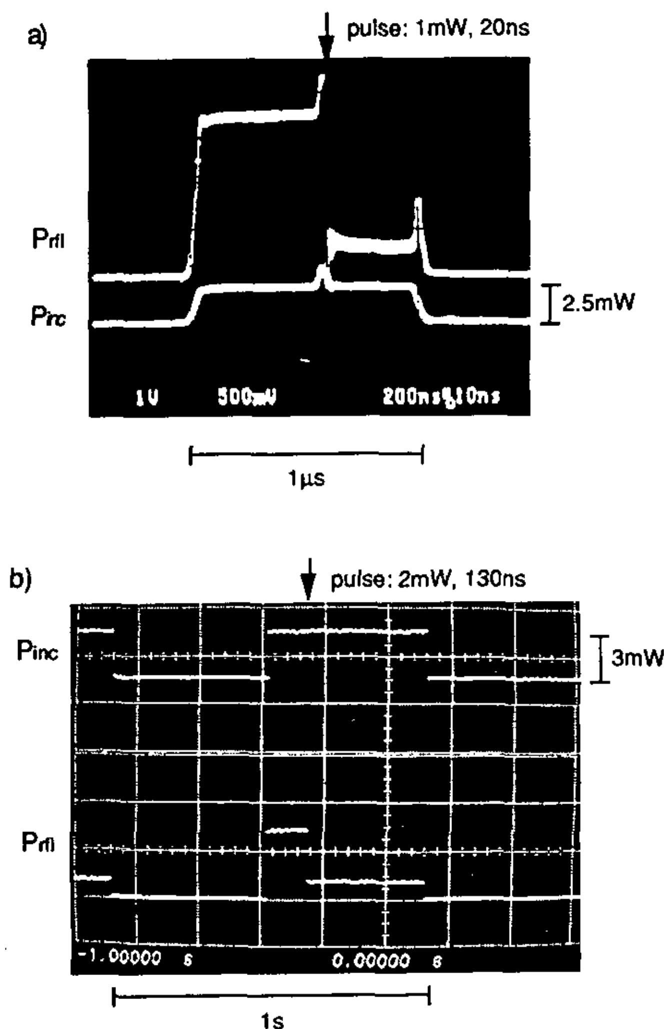

Fig. 3.19: Thermally stable latched operation of a NLFP: incident (P_{inc}) and reflected (P_{rfl}) power vs time:
a) The incident power is composed of a bias pulse (2.5 mW) of 1 µs duration and a short signal pulse (1 mW, 20 ns) which switches the reflected power from high to low.
b) The incident power is composed of a bias pulse (3 mW) of 0.5 s duration and a short signal pulse (2 mW, 130 ns, not visible on this time scale) which switches the output.

3.5.6 Detuning dependence

The device characteristics depend on the wavelength detuning between the operating and the resonance wavelength (Sect. 2.1.3). This dependence is important for the tolerancing of light sources and device reproducibility in arrays where the resonance wavelength changes due to thickness gradients (Sect. 3.5.2). The change of the threshold power and the contrast with operating wavelength has therefore been measured for different resonances (Fig. 3.20).

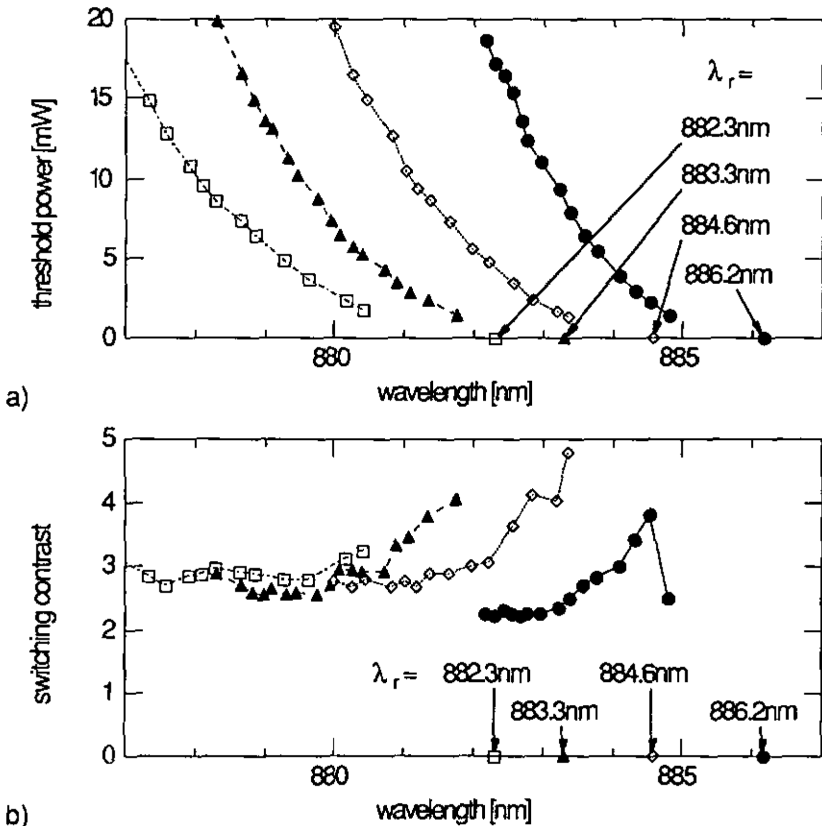

Fig. 3.20: Dependence of the switching properties on the detuning between the operating and the resonance wavelength λ_r, for four resonances: a) threshold power, b) switching contrast vs operating wavelength.

The observed dependence of the threshold corresponds remarkably well to the predictions of the high finesse approximation (Fig. 2.9a). A critical detuning of

about a resonance width is required for the onset of bistability (Eq. 2-23). A detailed measurement close to the critical point shows an almost linear threshold increase of about 1 mW/nm ($\lambda_r = 883.3$ nm). The detuning sensitivity increases towards longer wavelengths, that is, with finesse. The contrast ratio (Fig. 3.20b) decreases with detuning. This is due to the increase of the ON-state reflectivity with hysteresis width (Fig. 2.9b). The impedance matching condition causes the general maximum around 884 nm. The low contrast values observed in this measurement (half the typical ones) are due to objective imperfections.

3.5.7 Spotsize dependence

The nonlinear refractive index measurements (Sect. 3.3) have revealed the importance of transverse carrier diffusion. The following measurements show the dependence of the switching threshold on the size of the illuminated spot.

Setup

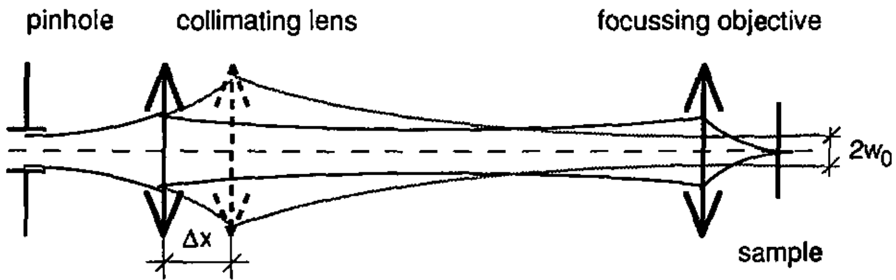

Fig. 3.21: Setup using a spatial filter with a movable collimator to change the spot size on the sample.

For this purpose, the spatial filter in the nonlinear setup (Fig. 3.6) has been modified. With a movable collimator the numerical aperture of the focusing objective, and thus the beam waist on the sample, can be varied between 2 and 20 µm. (The small longitudinal variation requires repositioning of the sample.) The waist of the Gaussian spot ($w_0 = \lambda/\pi\theta$) has been calibrated with respect to the collimator position (Δx in Fig. 3.21) by measuring the far-field diffraction angle θ.

Observations

Figure 3.22 shows the measured dependence of the minimum threshold power, and of the corresponding threshold intensity, on the beam waist. For a decreasing spotsize, the power drops approximately with the spot area, as expected from Fig. 2.18. For beam waists below $w_0 \approx 3\ \mu m$ there is a clear saturation behavior, and below $w_0 \approx 2\ \mu m$ a threshold increase is observed.

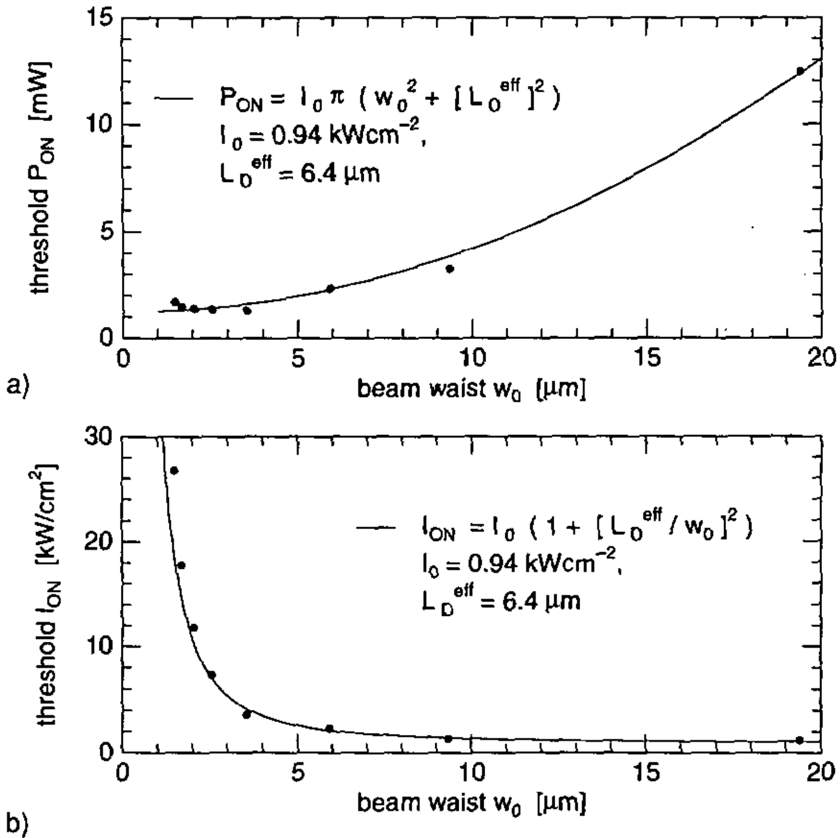

Fig. 3.22: Dependence of the minimum threshold on the beam waist: a) power, and b) intensity (λ_r = 882.8 nm). Dots represent experimental data, and lines correspond to the phenomenological fit given in the figure.

The experimental data of the threshold dependence has been fitted to a simple model, which assumes an asymptotic saturation towards an effective spot area

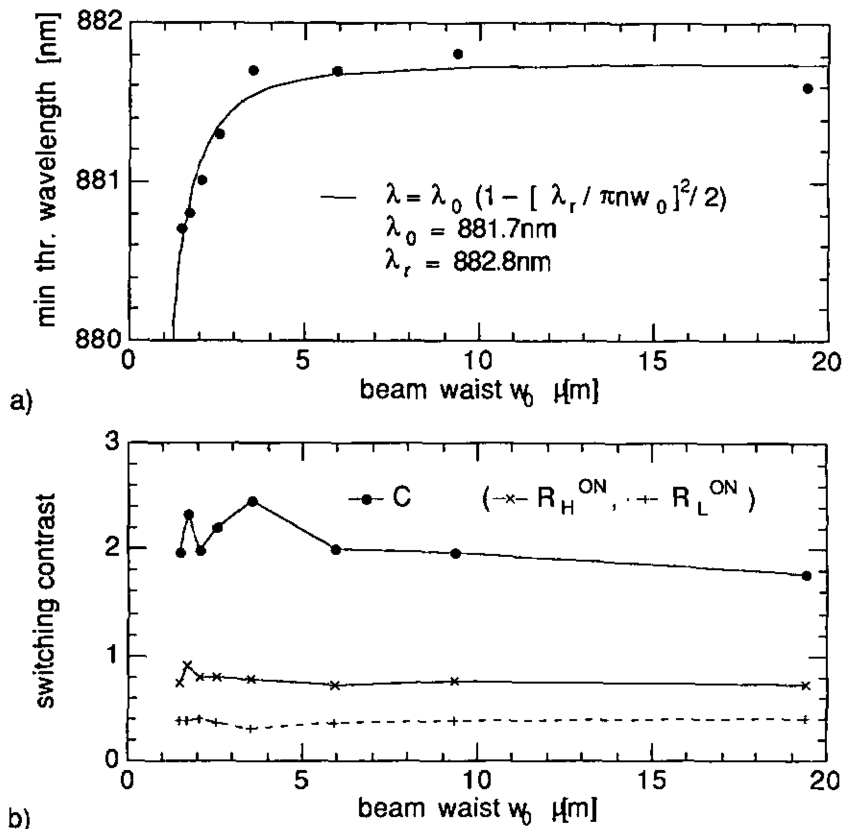

Fig. 3.23: Dependence of a) the operating wavelength, and b) the switching contrast on the beam waist. (λ_r=882.8 nm).

$\pi(L_D^{eff})^2$ for small spots. Fits for two different resonances suggest an effective spot radius $L_D^{eff} \approx 6$ μm, about two times larger than the expected diffusion length L_D (Sect. 2.2.3). This is because diffraction effects, which are responsible for the threshold power increase at very small spots, also contribute to L_D^{eff}. For the large spot limit, a threshold intensity $I_0 \approx$ 1–2 kW/cm^2 is derived, less than estimated from plane wave simulations ($I_0 \approx$ 5 kW/cm^2 in Fig. 2.25). The discrepancy may indicate a recombination time slightly longer than assumed (4 ns) for this sample.

The threshold power increase below about 2 μm beam waist can be explained by a broadening of the resonance due to increasing diffraction losses (cf Sect. 4.1.3).

Based on the numerical aperture ($\theta = \lambda/[\pi w_0]$) of a Gaussian beam, Fig. 3.23a shows the observed increase of the critical detuning to agree well with the wavelength shift calculated for oblique incidence (Eq. 2-10).

The contrast ratios in Fig. 3.23b show that the spotsize dependence of the contrast ratio is small, in agreement with theoretical predictions[92]. (The values are again deteriorated by the microscope objective used.)

Conclusions

The spotsize dependent measurements show that the switching power takes a minimum at an optimum beam diameter of $2w_0 \approx 6$ µm for this sample. At this spotsize, the switching intensity is about 5 times larger than in the plane wave limit, due to transverse diffusion and diffraction effects. This leaves a large potential for power reduction by using transverse carrier confinement, and optical waveguiding[93] which would allow spotsizes of less than $2w_0 \approx 4$ µm.

3.5.8 Critical biasing with on-axis dc-beam

Due to its stable thermal properties, the device can be biased close to threshold with a dc holding beam. Figure 3.24 shows single beam switching, where pulses of different power are superposed to a dc hold power of 1 mW, which corresponds to 97% of the threshold. The output power changes from close to 1 mW to about 0.3 mW, indicating a contrast ratio of 3:1. The power gain is 5 and 8 for signal powers of 0.13 mW and 0.07 mW, respectively.

Critical slowing down determines the duration of the OFF transition in all three cases. For a pulse height of 0.07 mW it also limits the achievable contrast ratio. The estimated (incident) switching energy is about 10 pJ. This switching energy requirement, together with the threshold power of ≈ 1 mW, gives rise to a gain-bandwidth product (cf Sect. 4.2.2) which is about 100 MHz in the present case.

The large differential reflectivities r_H and r_L, illustrated in Fig. 3.24b, are inherent to the single beam switching characteristic of a passive reflective device. Their detrimental effect for logic gate applications can be reduced by using the NLFP as a three-port rather than a two-port device (cf Sect. 4.2.1).

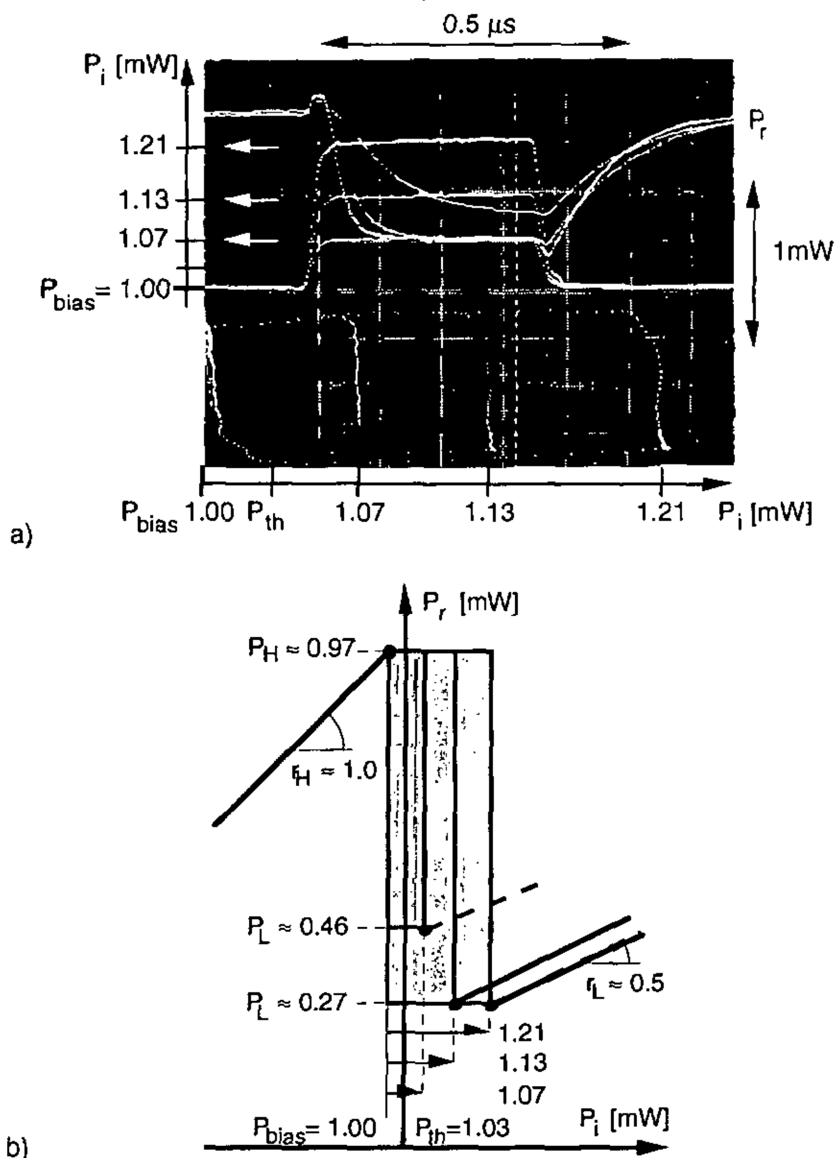

Fig. 3.24: Operation of sample #360 with a dc bias P_{bias} = 1 mW (97% P_{th}):
a) reflection response to power increments of 0.07, 0.13, and 0.21 mW, and the corresponding hysteresis loop.
b) sketch of the hysteresis loops with the power levels P_H and P_L, and the differential reflectivities r_H, r_L.

3.6 Ultrashort cavity NLFP

According to the analytic theory in Sect. 2.1.3, the threshold can be reduced arbitrarily by increasing the cavity finesse. This can be achieved by reducing the thickness D of the spacer, or by operating at a longer wavelength with smaller background absorption α. Simulations of a short cavity in Sect. 2.5.1 indeed show a lower threshold, but the enhanced wavelength sensitivity is expected to ultimately limit the device operation[94]. A short cavity has been grown and investigated (Fig. 3.25) to verify these predictions.

3.6.1 NLFP sample #386

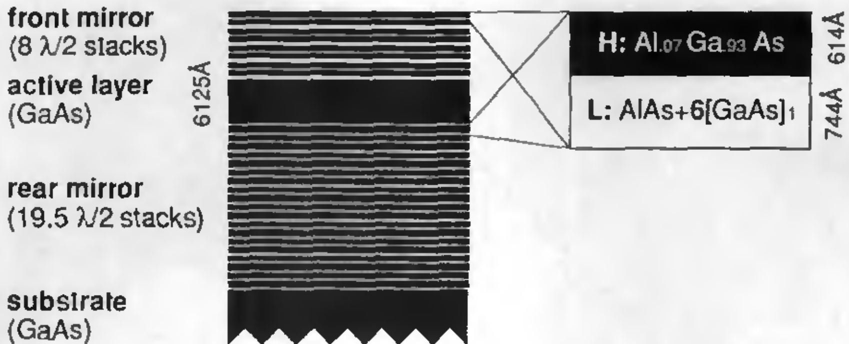

Fig. 3.25: Growth layout for sample #386: 0.6 µm spacer (5λ/2n) between 8 and 20 dielectric stacks.

The short NLFP consists of a 0.613 µm thick GaAs spacer (5λ/2n), between mirrors with 8 and 20 dielectric stacks. The dielectric stacks are essentially the same as in sample #360 (Fig. 3.14).

From the theoretical front mirror reflectivity of 0.94 we derive a finesse of about 50 at impedance matching condition (Eqs. 2-13,2-78). This is only 1.5 times the finesse of the 2 µm cavity (sample #360), while the spacer is 3 times thinner. Thus, the device operates at higher absorption ($\alpha \approx 500\ cm^{-1}$), 3 to 4 nm closer to the bandgap. The expected resonance width is slightly larger than in #360, because the free spectral range scales only by a factor of 2, due to the important dispersion contribution from the mirrors ($L_{eff} \approx 1.3\ \mu m$).

The sample (#386) was grown after the optical calibration step described in Sect. 3.2.2 and shows a thickness accuracy better than 0.5% within a distance of 13 mm from the rotation center (cf Fig. 3.15). A comparison of simulated and measured spectra in Fig. 3.26 shows a good agreement, and confirms that the measured absorption is smaller than that assumed in the model. The impedance matched resonance with a typical width of 1 nm occurs at about 881 nm, instead of the one predicted at 884 nm.

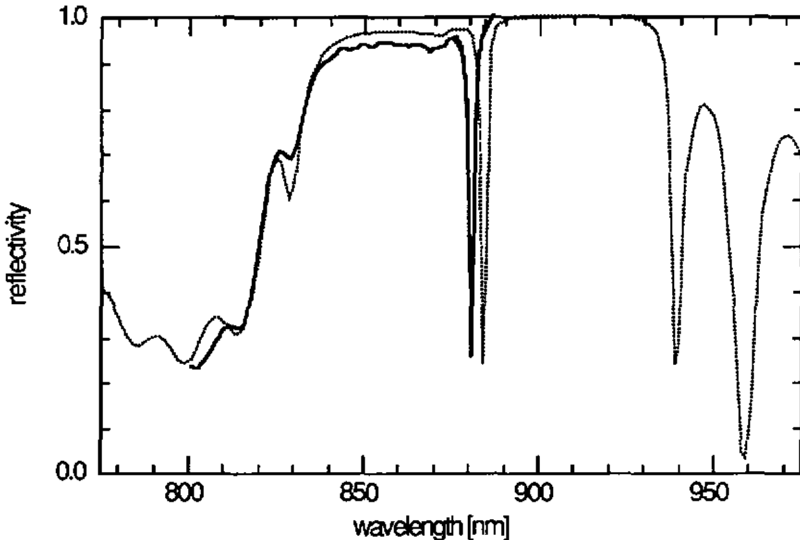

Fig. 3.26: Comparison of the linear spectra measured on sample #386 (solid line) with a simulation of the layout (dotted line).

3.6.2 Bistability

Bistable switching is observed in a range between 879 nm and 883 nm. However, the thresholds are at least twice as large as in sample #360. The hysteresis loops are less pronounced with respect to threshold and contrast ratio.

A dramatic increase of switching contrast (almost without any loss of power in the OFF-state) is obtained if a diaphragm is used to eliminate the defocused light from the reflected beam (Fig. 3.27). A characteristic property of this spatially filtered switching characteristic is a decrease of the reflected signal after switching ON,

while simulations and the high finesse approximation (Fig. 2.8) predict a positive differential reflectivity.

The similarity of the phenomenon to earlier observations[95] confirms that it is due to the self-defocusing property of the nonlinear material. The visibility of the effect, which is hardly observable in sample #360, indicates large spatially inhomogeneous index changes within the illuminated spot, probably related to the more important saturation effects[96] in this sample.

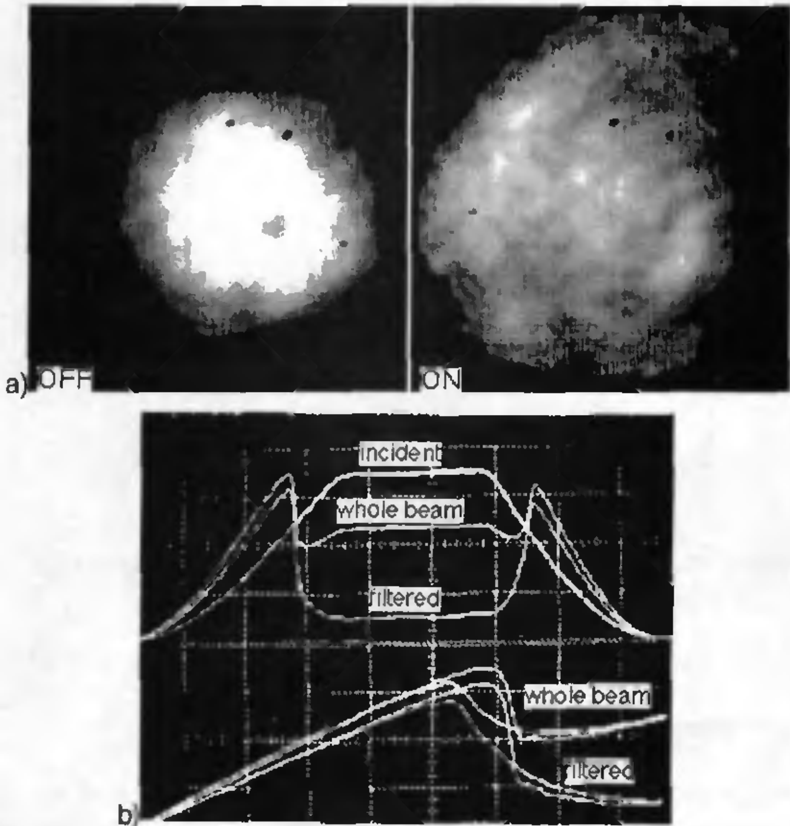

Fig. 3.27: Transverse switching effects in #386:
a) intensity profile of the reflected beam before (OFF) and after (ON) switching.
b) response to a trapezoidal incident pulse with and without transversal filtering.

3.6.3 Discussion

This short cavity device is not suited to studying the effect of a shorter spacer, because its finesse is similar to that of sample #360. Instead, a cavity with a higher finesse, operating at the same wavelength and absorption, should be grown.

However, the comparison of the two cavities with similar finesse but different operating wavelength clearly favors the device which operates further from the gap. This is probably related to saturation of the nonlinear refractive index change in the short device. At threshold, the nonlinear index changes have to be two times higher in the short sample compared to the 2 μm sample (#360). The critical saturating index change $\Delta n_S^c = 0.028$ estimated for this cavity is indeed close to the measured limit $\Delta n_S = 0.039$ (Sect. 3.4.4).

Still, the observed bistable characteristics with negative differential reflectivity in the ON-state may be of interest for system applications.

3.7 Nonlinear Bragg reflector devices

The nonlinear Bragg reflector device (NLBR) which is based on the same nonlinear material properties as the nonlinear Fabry-Perot device (NLFP) has been introduced in Section 2.4. The distributed nonlinearity and feedback complicate the analytical description and optimization of the NLBR, compared to the NLFP where lumped parameters can be used for the reflectors and for the nonlinear spacer. The optimization of two NLBR devices, a NLBR with 30 nonlinear dielectric stacks and an improved version with an additional linear rear mirror, therefore relied mainly on numerical simulations (Sect. 2.5.2). This section describes some preliminary experimental results obtained on the corresponding samples #363 and #388.

3.7.1 NLBR sample #363

The first NLBR sample consisted of 30 dielectric layer pairs with a nonlinear high index stack of GaAs and a linear low index stack of AlAs (Fig. 3.28).

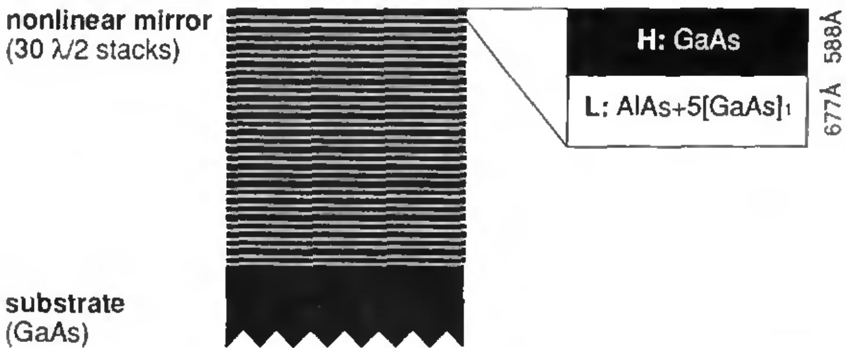

Fig. 3.28: Growth layout of sample #363: NLBR consisting of 30 dielectric stacks with a nonlinear (GaAs) high index layer.

Although the layers were grown about 8% too thick in the center, the wafer can be investigated close to the border, where the layers are thinner. This is because the only critical design parameter of this simple structure is the period of the Bragg mirror, which determines the position of the reflection minimum with respect to the bandgap. Spectra measured at low intensity (Fig. 3.29) show the reflection minimum at the desired wavelength. The spectral width of the minimum, 2–3 nm, is in good agreement with numerical simulations.

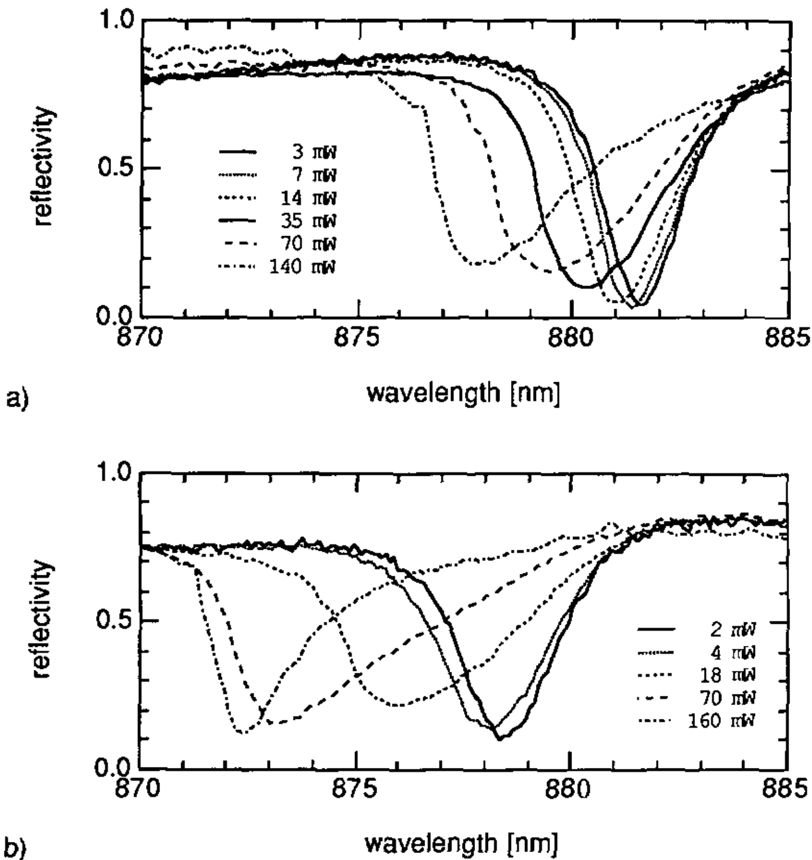

Fig. 3.29: Nonlinear spectra measured on NLBR #363 for reflection minima at a) 882 nm and b) 878 nm (spotsize 6.5 μm).

The nonlinear spectra reveal large shifts of the reflection minimum (up to 6 nm). Still, they are inferior to the estimated wavelength separation of about 8 nm between the reflection minimum and the stopband edge (Eq. 2-84).

According to Eq. 2-85 the wavelength changes of 4 nm and 6 nm in Fig. 3.29 correspond to refractive index changes of 0.016 and 0.025, respectively. The nonlinear index change is larger closer to the gap, but clearly saturates at high pump power. Also, the decreasing minimum reflectivity at high power indicates absorption saturation. These saturation effects are most likely responsible for the

absence of bistable switching in this sample. Nevertheless, the pronounced nonlinear characteristic could be used to demonstrate several logic functions[97].

3.7.2 NLBR sample #388

Numerical simulations predict a lower threshold for the NLBR, if the transmitted light, rather than being absorbed by the substrate, was reflected back into the mirror. Therefore, an improved NLBR, with a linear reflector behind the 30 nonlinear layer pairs, has been designed (Sect. 2.5.2). The simulations showed a strong dependence of the nonlinear characteristic on the relative phase between the two mirrors. This phase determines the position of the standing wave with respect to the nonlinear layers and can be adjusted via the thickness of the low index layer between the two mirrors (Fig. 2.27). In the layout of sample #388, which is sketched in Fig. 3.30, a thickness of $5\lambda/16$ has been selected.

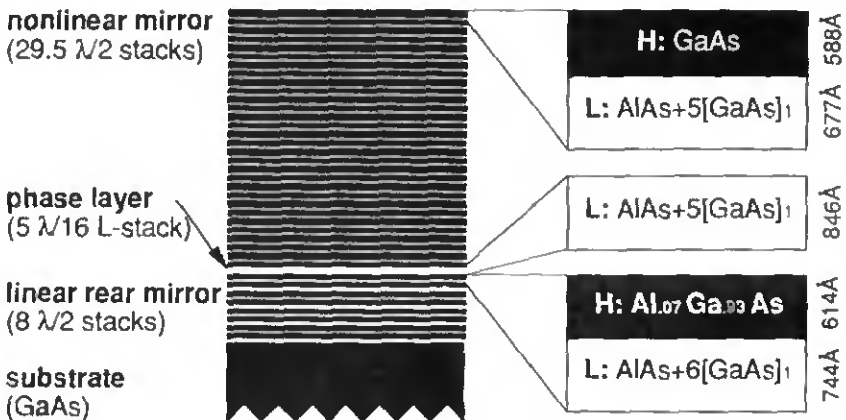

Fig. 3.30: Growth layout of sample #388: NLBR consisting of 30 nonlinear dielectric stacks in front of a linear rear mirror.

The actual thickness of the layers in the NLBR sample #388, which was part of the same MBE charge as the NLFP #386, is very close to specification. Nevertheless, a deviation of −1% (in the center of the wafer) displaced the reflection minima to 877 nm, compared to an optimum around 885 nm. To increase the separation from the bandgap to the desired 15 nm, the sample had to be cooled by almost 100 K.

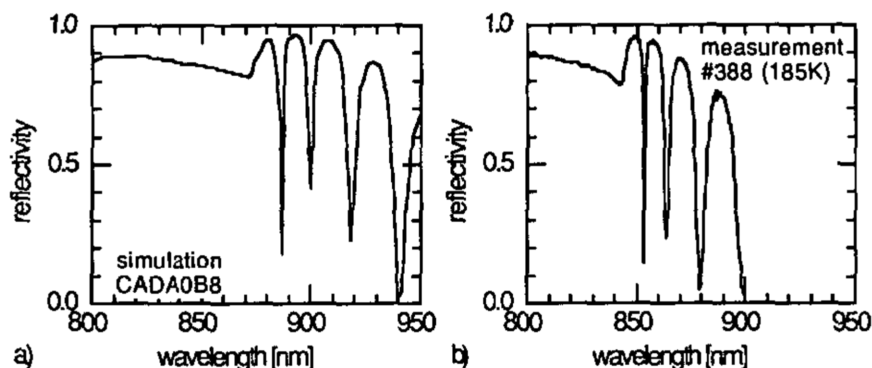

Fig. 3.31: Low intensity reflectivity spectra of NLBR sample #388, according to a) simulation, and b) measurement at 185 K.

At a temperature of 185 K, the reflectivity minimum (R ≈ 0.1) is located at 853 nm and has a width of 0.7 nm (Fig. 3.31). Nonlinear spectra show a wavelength shift of 3.2 nm at an incident power of 13 mW. Optical bistability has been observed in a ±10 K temperature range (λ_r = 853±1 nm) around this point. However, the threshold of about 4 mW as well as the contrast ratio of 3:1 (Fig. 3.32) are poor compared to the performance of the NLFP device (Sect. 3.5). The switching is not stable in the ON position; due to heating the reflectivity switches back OFF after about 1 μs.

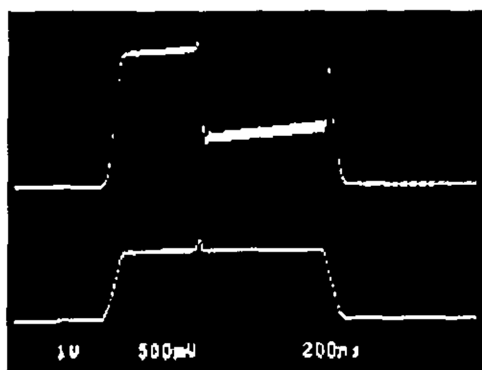

Fig. 3.32: Latched bistable switching of the NLBR sample #388.

3.7.3 Comparison of NLBR and NLFP

The nonlinear Bragg reflector is an alternative device for optical bistability. It is based on the same refractive nonlinearity as the nonlinear Fabry-Perot, but uses a distributed feedback structure. So far, the slightly lower thresholds predicted by simulations could not be verified experimentally. The cause is probably related to saturation of the nonlinear properties. Therefore, the necessary nonlinear index change should be reduced in future improved structures. This could be achieved by increasing the number of dielectric pairs. According to the analytical considerations in Sect. 2.4.2, about 100 pairs ($N\Lambda \approx 15$ µm) are feasible before absorption becomes important. Another possibility to improve the steepness of the stopband edge is the design of stacks with a chirped periodicity.

Two different NLBR structures have been realized so far: a plain Bragg reflector with nonlinear high index layers, and an improved design which includes a phase layer and a linear rear reflector. Compared to the NLFP, the plain NLBR has the advantage of a simple design: The only critical growth parameter is the mirror periodicity Λ which determines the position of the reflection minimum with respect to the bandgap. This parameter could be tuned with temperature (Sect. 3.3.3) or electrical fields (Franz-Keldysh effect). Because of the limited effect of temperature tuning however (Sect. 3.3.3), the growth tolerance would still be restricted to about 1%. In the "improved" NLBR design, the advantage of simpler design is lost. Indeed, the additional linear rear mirror introduces phase and intensity conditions, very similar to those of an impedance matched NLFP.

3.8 Conclusions

A setup with a coherent source has been built for nonlinear spectral reflectivity measurements. In addition, this setup proved very valuable for a precise optical calibration of MBE samples.

The feasibility of processing techniques such as etching, and sputtered deposition of dielectric mirrors for post-growth adjustments has been demonstrated. The limitations of temperature tuning have been explored.

A maximum refractive index change of 0.025 in GaAs at 882 nm has been measured with a single wavelength setup. This corresponds to an estimated carrier density of about 10^{18} cm^{-3}, or a nonlinear cross-section $\eta \approx 2 \cdot 10^{-20}$ cm^3. The measured nonlinear index changes, and the estimated saturation value $|\Delta n_s| \approx 0.04$ are about twice as high in bulk than in MQW material[42]. A red-shift of the impedance matching condition indicates an absorption increase from $\approx$ 100 cm^{-1} to $\approx$ 240 cm^{-1} (dominant bandgap renormalization contribution) at moderate carrier densities in GaAs. Both observations favors bulk material for use in nonlinear devices based on plasma effects.

Optical bistability has been demonstrated at 1 mW threshold power in a NLFP with a 2 µm spacer. The device has been operated thermally stable for more than 0.5 s, in a biased and in a latched mode, with an on-axis hold beam close below, respectively slightly above the threshold. Measurements of critical slowing down have shown that the absorbed switching energy is less than 5 pJ, independent of the switching increment. By operating the device with a bias beam, a differential signal gain of 8 has been demonstrated. The achievable gain is limited by a gain-bandwidth product of about 100 MHz, which is determined by the minimum threshold power and the switching energy requirement.

Operating tolerances have been investigated on this sample. They indicate that a deviation of the operating wavelength by 0.1 nm implies a 10% threshold change. The thickness gradients measured on the present wafers ($\partial\lambda/\partial x \approx 1$ nm/mm) would therefore limit the size of arrays to less than 1 mm extension.

Measurements with variable spotsize demonstrate the importance of transverse effects related to carrier diffusion and diffraction, which limit the achievable threshold power (at a spotsize of 6 µm in this NLFP), unless pixellation and waveguiding can be used.

A NLFP grown with a spacer of only 0.6 μm thickness was not suited to study the limits of high finesse. It shows that saturation and transverse effects become more important closer to the bandgap.

Two nonlinear Bragg reflector (NLBR) devices have been investigated. Theoretically, the simpler structure of a Bragg reflector compared to the impedance matched NLFP device represents an advantage with respect to fabrication tolerance and tuning capability, and the simulations predict slightly lower switching thresholds. Optical bistability in a NLBR has been demonstrated, although so far at higher thresholds ($\approx$ 3 mW) than for the NLFP device. Also, the bistable NLBR device includes a phase layer and a rear linear mirror and therefore has a structure of similar complexity to that of the impedance matched NLFP. It is thus doubtful if NLBR represent a conceptual advantage over NLFP.

4 ASPECTS OF OPTICAL LOGIC DEVICES

In the field of optical computing there is a gap between device people trying to identify and optimize the relevant parameters of a nonlinear optical device, and systems people looking for the optical device which is best suited for a given task. This gap arises because the criteria to assess devices for use in parallel systems have not yet been identified.

The performance of a nonlinear device in a parallel system strongly depends on three aspects. Firstly, the physical characteristics of a single device, such as dimensions, switching energy, speed, and input/output characteristics. Secondly, its mode of operation, namely which nonlinear function is implemented and how the addressing of the input and output signals is accomplished. Thirdly, the performance of the system depends on tolerance parameters related to the parallel operation of multiple devices, including imperfections of the sources and the optics. This third aspect, called "tolerancing", is the key to the design of parallel systems[98].

The first section presents some issues of physical device optimization, based on the existence of a small effective volume of nonlinear material which has to be excited. The second section deals with the optimal use of the emergent device properties. Different addressing schemes, and the possibilities of signal fan-in are discussed. The third section is concerned with the wavelength sensitivity, which is the main tolerancing aspect for devices with a resonant cavity, such as the nonlinear Fabry-Perot (NLFP). Finally, in the fourth section, the NLFP is compared to three alternative optical computing devices.

4.1 Device scaling

An optimized, integrated NLFP device can be characterized by two principal parameters: the nonlinear spacer material with given absorptive and refractive properties at an optimum operating wavelength, and the active device volume determined by the resonant cavity. Correspondingly, efforts to improve devices concentrate on the search for better nonlinear materials and cavities with smaller active volume (eg a single quantum well in a pixellated device). This section introduces a material figure of merit, and discusses how the switching energy and intensity scale with the active device length (or inverse finesse) and area.

4.1.1 Nonlinear material

According to Section 2.13, a minimum nonlinear phase change $\Delta\varphi^c$ of about one resonance width $\delta\varphi$ is required to switch a balanced high finesse NLFP. This requirement corresponds to a critical refractive index change Δn^c (Eq. 2-25), or a corresponding critical carrier density N^c, in the nonlinear spacer

$$N^c \geq \frac{2}{\sqrt{3}} \frac{1}{\eta} \frac{\alpha}{k}. \qquad (4\text{-}1)$$

From a nonlinear cross-section $\eta \approx 2 \cdot 10^{-20}$ cm^3, typical for bulk GaAs (Sect. 3.4), and an absorption coefficient $\alpha \approx 250$ cm^{-1} (as in the NLFP #360, Sect. 3.5) one finds a critical carrier density $N^c \approx 2 \cdot 10^{17}$ cm^{-3}.

This relation confirms the experimental observation that NLFP devices should be operated at an energy difference $\Delta\mathcal{E} \approx 25$ meV below the bandgap energy. At this detuning, the background absorption is small, while the nonlinear refraction is still large. Closer to the bandgap ($\Delta\mathcal{E} < 15$ meV), the large background absorption demands carrier densities approaching 10^{18} cm^{-3}, and saturation phenomena become important. (cf samples #337 and #386 in Sects. 3.4, 3.6, respectively).

Considerably larger cross-sections, up to $\eta = 37 \cdot 10^{-20}$ cm^3, have been reported[99] for GaAs/AlGaAs multiple quantum well material (MQW). Because of the larger background absorption however, the expected critical carrier densities are not much smaller than in bulk GaAs. Indeed, at room-temperature, NLFP devices based on MQW material also rely on carrier plasma effects, because the enhanced excitonic features saturate before the critical densities are reached[41]. The low thresholds observed in bulk GaAs (Sect. 3.5) confirm this argument.

Although the research on integrated Fabry-Perot devices, so far, has been centered on the AlGaAs compound, resonant optical nonlinearities are being investigated in a large variety of materials[100,101], including organic compounds[102]. Of interest in the field of semiconductors are recent attempts to improve the nonlinear material based on further quantum confinement in quantum wires and dots[103], on internal electrical fields in coupled well structures[104,105,106], and on doping in degenerate semiconductors[107].

Figure of merit

The nonlinear cross-section η is an appropriate material figure of merit (fom) to compare the dispersive nonlinearities of resonant electronic transitions:

$$\mathrm{fom}_{\mathrm{material}} \equiv \frac{\sqrt{3}}{2}\,\eta \qquad\qquad = \frac{\sqrt{3}}{2}\,\frac{hc}{\tau}\left(\frac{n_2}{\alpha\lambda}\right)\Bigg|_{\substack{\text{steady}\\ \text{state}}} . \tag{4-2}$$

This fom represents the volume in which one photon generates the critical carrier density N^c. As will be shown below, this volume is relevant because the achievable optical confinement is limited. In comparison to a previous figure[22] $n_2/\alpha\lambda$, based on the Kerr coefficient n_2 (Eq. 2-21), which minimizes the steady state switching intensity, the extra factor $1/\tau$, containing the recombination time, accounts for the speed of the switching device.

4.1.2 Shorter cavities with higher finesse

The scaling of the switching intensity with finesse $\mathcal{F}$, or alternatively, with spacer thickness L, is derived from the critical energy density and the cavity response.

Critical energy density

In order to generate the critical carrier density N^c, a minimal energy per unit area, $e_a{}^c$ (Eq. 2-48), has to be absorbed in the nonlinear spacer of thickness L

$$e_a{}^c = \hbar\omega\, N^c\, L = \frac{2}{\sqrt{3}}\,\frac{\hbar c}{\eta}\,\alpha L = \frac{\pi}{\sqrt{3}}\,\frac{\hbar c}{\eta}\,\frac{1}{\mathcal{F}} \tag{4-3}$$

This minimal energy density decreases proportionally with spacer thickness L, or inversely to the finesse $\mathcal{F} = \pi/(2\alpha L)$ of an optimized cavity. The cross-section $\eta = 2\cdot 10^{-20}\ \mathrm{cm}^3$ suggests an approximate energy density $e_a{}^c = 2\ \mathrm{pJ}/\mu\mathrm{m}^2/\mathcal{F}$.

Photon lifetime

Two time constants determine the time evolution of the carrier density (carrier rate equation 2-45). The carrier loss is described by the recombination time τ (which may be the enhanced $\tilde{\tau}$ in the case of critical slowing down; Eq. 2-51). The carrier generation follows the evolution of the cavity intensity, which is governed by the cavity build-up time τ_{cav}, or photon lifetime ($1/\delta\nu_{cav}$, Eqs. 2-8,9)

$$\tau_{cav} = \frac{2nL_{eff}}{c}\mathcal{F} = \tau_{cav}^{\infty}\left(1+\frac{L_m}{L}\right) = \tau_{cav}^{\infty}\left(1+\frac{\mathcal{F}}{\mathcal{F}_m}\right); \qquad (4\text{-}4)$$

$$\tau_{cav}^{\infty} = \left(\frac{4\pi}{\omega}\right)\frac{\pi n_g}{2\alpha\lambda}, \qquad L_m \equiv \frac{\pi}{2\alpha\mathcal{F}_m} \approx \kappa^{-1}.$$

The path L_m describes the retardation in the distributed dielectric mirrors (Eq. 2-88). L_m is approximately the inverse coupling constant $\kappa^{-1} = \lambda/(2\delta\bar{n})$, which is about 0.74 µm for an index step $\delta\bar{n} = 0.6$, L_m (Eq. 2-81,75).

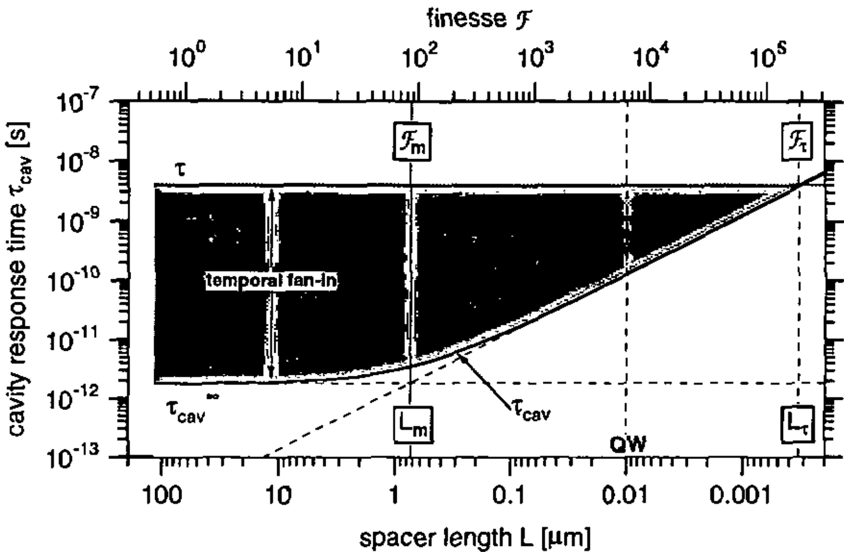

Fig. 4.1: Scaling of the cavity build-up time τ_{cav} with spacer thickness L (or with cavity finesse $\mathcal{F} = \pi/[2\alpha L]$).

If the spacer is thick compared to the equivalent optical path L_m, the cavity build-up time is about constant, $\tau_{cav} = \tau_{cav}^{\infty} \approx 1.8$ ps. As L becomes smaller than L_m, or alternatively when the finesse $\mathcal{F}$ exceeds $\mathcal{F}_m$ (≈ 85 for $\alpha \approx 250$ cm^{-1}), the build-up

time τ_{cav} begins to increase proportionally with the finesse (Fig. 4.1). Ultimately, at a hypothetical finesse $\mathcal{F}_\tau$ determined by

$$\frac{L_m}{L_\tau} = \frac{\mathcal{F}_\tau}{\mathcal{F}_m} = \left(\frac{\tau}{\tau_{cav}^{\infty}} - 1\right) \approx \frac{\tau}{\tau_{cav}^{\infty}}, \tag{4-5}$$

the photon lifetime would exceed the carrier recombination time τ. This situation corresponds to a device that accepts a single temporal mode within the integration time given by τ and is thus relevant to the temporal fan-in studied in Sect. 4.2.3. However, this limit is only of theoretical importance, because it corresponds to a finesse $\mathcal{F}_\tau \approx \omega\tau/(2\pi)\cdot\overline{\delta n}/n_g \approx 2\cdot 10^5$, or a thickness $L_\tau \approx 0.3$ nm for the assumed values. A realistic upper limit for integrated NLFP devices is the thickness of a single quantum well, or about 10 nm.

Switching intensity

In typical integrated NLFP devices ($L \approx 2$ µm), the build-up time τ_{cav} is small compared to the recombination time ($\tau_{cav} \ll \tau$). Because it takes τ_{cav} to absorb the energy of an incident pulse, the intensity e_a^c/τ_{cav} is the maximal (constant) intensity which efficiently switches the device. On the other hand, the generated carriers are integrated over the recombination time τ before they start recombining. Therefore, the lowest incident intensity which produces the critical carrier density, the threshold intensity, is approximately

$$I_i^c = \frac{e_a^c}{\tau} = \frac{\pi}{\sqrt{3}} \frac{\hbar c}{\eta\tau} \frac{1}{\mathcal{F}} . \tag{4-6}$$

The intensity decreases proportionally to the finesse $\mathcal{F}$ (Fig. 4.2), in agreement with Eq. 2-24. For a carrier recombination time $\tau = 4$ ns and a cross-section $\eta = 2\cdot 10^{-20}$ cm^3, one finds a critical threshold $I_i^c = 70$ kW/cm^2 / $\mathcal{F}$. Comparing this to the asymptotic threshold $I_i^c = 1$ kW/cm^2 derived from the spotsize dependent measurements on sample #360 ($\mathcal{F} = 35$, Sect. 3.5.7), the factor of two difference can be explained by a longer recombination time $\tau \approx 8$ ns in that sample.

In the hypothetical situation described by $\mathcal{F}_\tau$, carrier recombination ($\tau \leq \tau_{cav}$) would lead to a theoretical threshold limit at about 0.5 W/cm^2. In practice, however, structural imperfections of the crystal will restrict the achievable finesse to smaller values. A more realistic value[24] of $\mathcal{F} \approx 10^3$ would allow for threshold intensities down to 70 W/cm^2 ($e_a^c \approx 2$ fJ/µm^2).

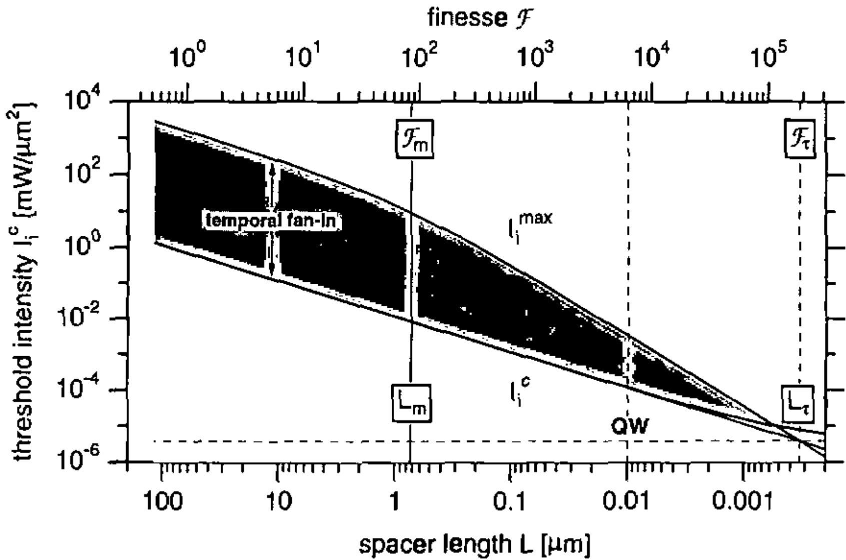

Fig. 4.2: *Scaling of the threshold intensity I_i^c with spacer thickness L (or with cavity finesse $\mathcal{F} = \pi/[2\alpha L]$).*

4.1.3 Smaller device area (pixels)

From the critical energy density and the device area one can estimate the switching energy. The transverse dimensions of a nonlinear Fabry-Perot are restricted by carrier diffusion, and by a diffraction effect which depend on the cavity finesse. For comparison, the transverse confinement in a waveguide structure is estimated first.

Waveguide confinement

An alternative to the planar Fabry-Perot cavity is the use of a waveguide resonator (or cavity with spherical mirrors). The transverse confinement in a waveguide is limited by the achievable refractive index step $\delta\bar{n}_G \equiv (n_H - n_L)$ of the waveguide. The minimum radius w_G of a guided mode is approximately

$$w_G \approx \frac{\lambda}{\pi\sqrt{n_H^2 - n_L^2}} \approx \frac{\lambda}{\pi\sqrt{2n\delta\bar{n}_G}}, \tag{4-7}$$

which leads to an estimated minimum switching energy of

$$E_G = e_a{}^c\,\pi w_G{}^2 \approx \frac{E_0}{\mathcal{F}}\frac{n}{2\delta\bar{n}_G}; \qquad E_0 = \frac{1}{2\pi\sqrt{3}}\frac{\hbar\omega}{\eta}\frac{\lambda^3}{n^2-1}\,. \qquad (4\text{-}8)$$

In this simple waveguide model, the switching energy decreases proportionally to the spacer length, or inversely to the finesse $\mathcal{F}$. The achievable index step $\delta\bar{n}_G$ is generally small compared to the spacer index n. An index step $\delta\bar{n}_G \approx 1.2\cdot10^{-2}$ (cf [111]) allows for a waveguide radius $w_G \approx 1$ µm, and correspondingly for switching energies $E_G \approx 10$ fJ at a finesse $\mathcal{F} = 10^3$. This energy represents $4\cdot10^4$ absorbed photons, considerably more than have been postulated from statistical arguments[108]. Interestingly, in the hypothetical limit of maximum longitudinal ($\mathcal{F} = \mathcal{F}_\tau$) and transverse ($n_L = 1$) confinement, the switching energy corresponds to about one photon ($E_0/\mathcal{F}_\tau \approx \hbar\omega$), which is an indication that the assumed four-dimensional material cross-section $\eta\tau$ is close to a physical limit.

Diffraction limited Fabry-Perot

In a Fabry-Perot cavity, diffraction losses become important for small spotsize and high finesse. Some simple considerations show that diffraction prevents a further reduction of the switching volume, and therefore of the switching energy.

The spectral width ($\delta\lambda/\lambda$) of a Fabry-Perot seen by a beam with angular divergence θ_i (eg a Gaussian beam with a waist $w_0 \approx \lambda/\pi\theta_i$) is limited by the dependence of the resonance on the angle of incidence (Eq. 2-10). This can be expressed[92] by a relation between the finesse $\mathcal{F}$ and the Fresnel number F_s

$$\frac{\delta\lambda}{\lambda} \approx \frac{\lambda}{2nL_{eff}\mathcal{F}} \geq \frac{1}{2}\left(\frac{\theta_i}{n}\right)^2 \Leftrightarrow \qquad F_s \equiv \frac{n\pi w_0{}^2}{\lambda L_{eff}} \geq \frac{\mathcal{F}}{\pi}\,. \qquad (4\text{-}9)$$

This condition calls for a *diffraction limited* spot size (or a limited angular aperture) to reduce the diffraction losses of a planar Fabry-Perot cavity

$$\pi w_0{}^2 = \frac{\lambda L_{eff}}{n\pi}\mathcal{F} = \pi w_\infty^2\left(1 + \frac{L_m}{L}\right) = \pi w_\infty^2\left(1 + \frac{\mathcal{F}}{\mathcal{F}_m}\right); \qquad (4\text{-}10)$$

$$\pi w_\infty^2 = \frac{1}{\pi}\left(\frac{\lambda}{n}\right)^2\frac{\pi n_g}{2\alpha\lambda}\,.$$

The diffraction limited area is about constant $\pi w_\infty^2 \approx 6\ \mu m^2$ for cavities with a low finesse. However, as the finesse $\mathcal{F}$ exceeds $\mathcal{F}_m$, it begins to increase proportionally

(Fig. 4.3). This area, together with the energy per unit area e_a^c, determines the minimum switching energy of a Fabry-Perot device in the diffraction limit

$$E_{FP} = e_a^c \pi w_0^2 = E_0 \left(1 + \frac{\mathcal{F}_m}{\mathcal{F}}\right) \frac{n_g}{n} . \qquad (4\text{-}11)$$

Thus, increasing the finesse (or reducing the spacer thickness L), reduces the switching energy only for finesse values smaller than $\mathcal{F}_m \approx 85$ (Fig. 4.4). The minimal switching energy and the minimal device volume remain approximately constant for a finesse larger than $\mathcal{F}_m$ (or $L \leq L_m$). From the assumed material parameters follows a minimal switching energy $E_0 \cdot n_g/n \approx 0.2$ pJ, and a minimal threshold power $E_0/\tau \cdot n_g/n \approx 50$ μW, as a limit for NLFP based on GaAs.

Experimentally, the switching energy (power) of a device with given finesse can be reduced by using smaller spots (Fig. 3.23). However, as the spotsize reaches the diffraction limit (Eq. 4-10), the diffraction losses unbalance the cavity and lead to an increase of the switching energy. This explains the spotsize dependence observed in Fig. 3.23, where the calculated diffraction limit is $w_0 \approx 1.5$ μm.

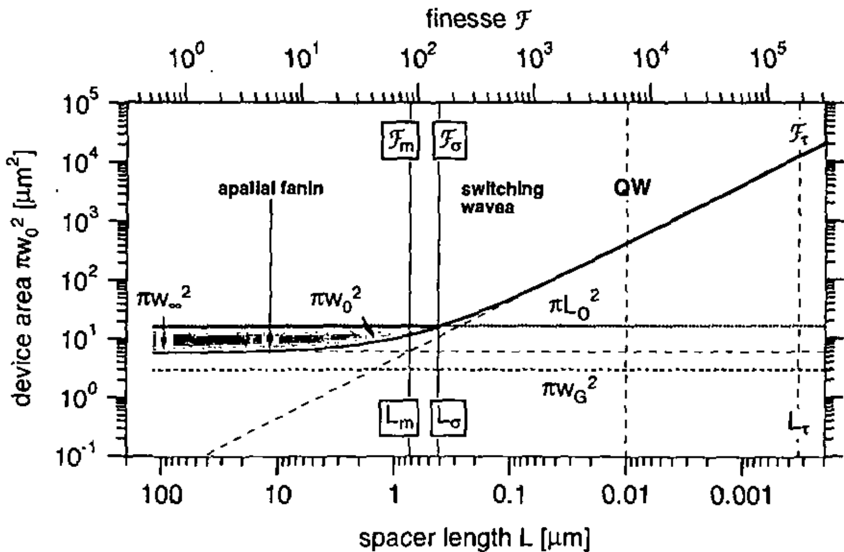

Fig. 4.3: Scaling of the diffraction limited spot size with spacer thickness L (or with cavity finesse $\mathcal{F} = \pi/[2\alpha L]$).

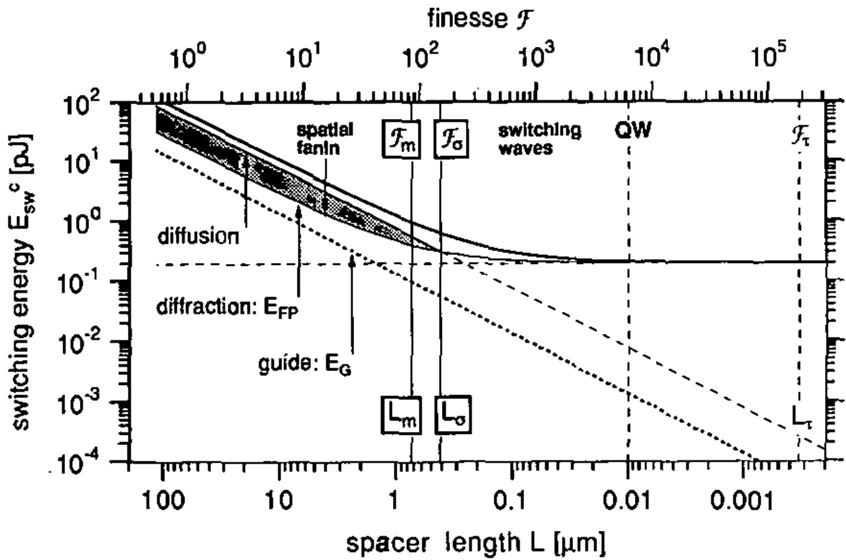

Fig. 4.4: *Scaling of the switching energy (threshold power) with spacer thickness L (or with cavity finesse $\mathcal{F} = \pi/[2\alpha L]$).*

Integrating diffusion spot

Within a time interval Δt, excited carriers diffuse an average distance $\sqrt{\mathcal{D}\Delta t}$. The ambipolar diffusion constant $\mathcal{D} = 2\mathcal{D}_p\mathcal{D}_n/(\mathcal{D}_p+\mathcal{D}_n)$ of GaAs[32] is approximately 13 cm^2/s at a density $N \approx 10^{17}$ cm^{-3}. The diffusion length L_D, corresponding to the recombination time τ, is thus given by

$$L_D{}^2 = \mathcal{D}\tau \,. \qquad (4\text{-}12)$$

The corresponding area $\pi L_D{}^2 \approx 16$ μm^2 describes the averaging area of the device under steady state conditions. It is about three times larger than the asymptotic diffraction limited spot $\pi w_\infty{}^2$. In this case the diffusion determined device area allows for a limited spatial fan-in (cf Sect. 4.2.3), but enlarges the minimum threshold power (and the steady state switching energy) determined by diffraction. The diffraction limited spotsize grows with increasing finesse (Eq. 4-10). It exceeds the diffusion area $\pi L_\sigma{}^2$ for a finesse larger than $\mathcal{F}_\sigma \approx 150$ (or a thickness smaller than $L_\sigma = 0.4$ μm for $\alpha = 250$ cm^{-1}), determined by

$$\frac{L_m}{L_\sigma} = \frac{\mathcal{F}_\sigma}{\mathcal{F}_m} = \left(\frac{\pi\mathcal{D}\tau}{\pi w_\infty{}^2}\right) - 1 = \frac{2\pi\mathcal{D}\tau\alpha n^2}{\lambda n_g} - 1 \,. \qquad (4\text{-}13)$$

Above this limit the switching energy cannot be reduced further by increasing the finesse (Fig. 4.4), and no spatial fan-in exists.

The diffusion spot corresponding to $\Delta t = \tau_{cav} \ll \tau$ is much smaller than the diffraction spot. Therefore at switch-ON, the carrier density follows the intensity distribution adiabatically, and slightly smaller switching energies (not limited by diffusion) are possible with short pulses.

For steady state operation and at switch-OFF however, the recombination time τ is the relevant time constant. Transverse switching waves[109] occur when the spotsize exceeds the diffusion area. Dynamic studies[53] have shown that switching waves at switch-OFF reduce the width of the observed hysteresis loop by a factor of two compared to a plane wave model.

Diffusion is responsible for the saturation of the threshold in the spotsize dependent measurements (Fig. 3.23). The saturation spot $L_D^{eff} \approx 6$ µm which has been fitted to the experiment is larger than the estimated diffusion length $L_D \approx 2.3$ µm because it includes the diffraction effects.

4.1.4 Limits of device scaling

Only the switching intensity, but not the switching energy or threshold power of GaAs based Fabry-Perot devices, can be improved much further by increasing the finesse. This is because device scaling is hindered by the finite confinement in the dielectric mirrors. As the spacer thickness becomes smaller than the penetration length L_m, or alternatively, as the finesse exceeds $\mathcal{F}_m \approx 85$, the diffraction limited spotsize and the cavity build-up time increase proportionally with the finesse so that the effective device volume remains approximately constant. Another limit is given by $\mathcal{F}_\sigma \approx 150$, above which the device given by the diffusion spot accepts a single spatial mode (cf Sect. 4.2.3), and transverse switching waves will occur. Integrated NLFP cannot reach the third limit $\mathcal{F}_\tau$, at which the cavity build-up time would exceed the recombination time (single temporal mode device).

However, with the use of waveguiding (pixellation) a reduction of the switching volume below the diffraction limit can be achieved. Methods based on various etching techniques have been studied[110], providing a good carrier and light confinement, but suffering from enhanced surface recombination effects. Carrier

recombination times drop into the ps range, and surface passivation techniques give only modest improvements. Another promising recent technique, which can be used for multiple quantum well spacers, is alloy mixing based on ion implantation and subsequent interdiffusion. Transverse barriers of 110 meV height, corresponding to an index step of $1.2 \cdot 10^{-2}$, and a resolution better than 5 μm have been reported[111].

4.2 Modes of operation

The characteristics of the NLFP device have been optimized with respect to contrast and threshold ratio. From the reported properties it should be judged if the device is suited for application as a pulse shaping element (limiter), as a threshold/logic element (gate), or as a memory (latch) (Sect. 4.2.1). The implementation (addressing) of a three-port device, and its fan-in and fan-out capabilities are discussed in Sections 4.2.2 and 4.2.3, respectively.

4.2.1 Device applications

The reflected output of a device in response to a single incident input beam has been optimized and studied experimentally. Figure 4.5 sketches the typical inherent two-port I/O characteristic of a reflective NLFP device.

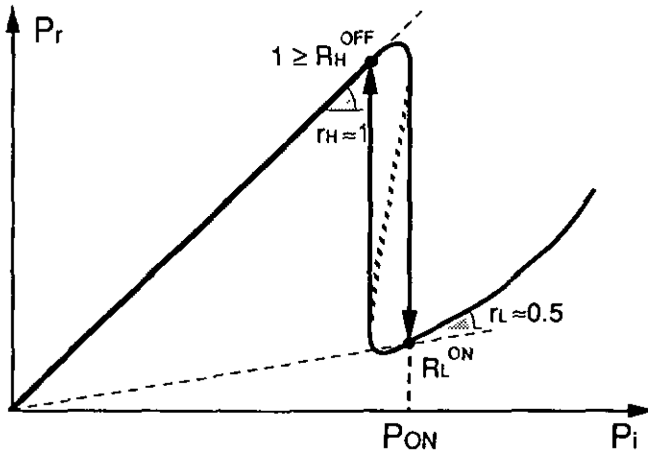

Fig. 4.5: Typical two-port I/O characteristic of a NLFP device.

The principal experimental device parameters are a threshold power of about 1 mW and a switching contrast ratio of about 10:1 (Sect. 3.5.3). The existence and the width of a bistable region depend on the wavelength detuning from resonance (Sect. 3.5.6). Time dependent studies with a (coherent on-axis) bias (Sect. 3.5.8) show that the device can be critically biased below or within the hysteresis region, from where it can be switched with a short signal pulse of approximately 10 pJ

incident energy. The minimal separation between the bias and the threshold power P_{ON} is determined by the fluctuations of the source; a device has been successfully biased at 97% P_{ON} with a $Ti:Al_2O_3$ source. Because of critical slowing down, the transition time is determined by the power of the switching signal: switching within 40 ns has been observed for a switching increment of about 20% P_{ON}, in agreement with a switching energy of less than 10 pJ.

Pulse shaping (limiter)

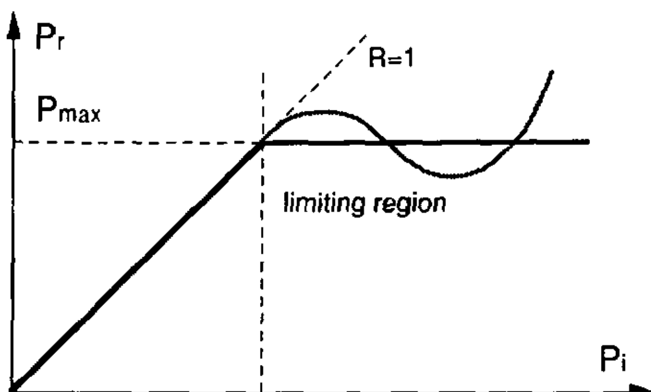

Fig. 4.6: Characteristic of an optical limiter: ideal (black), achievable (grey).

The only true two-port application, of the above mentioned, is pulse shaping. Obviously, the I/O characteristic of a bistable NLFP (Fig. 4.5) is not particularly suited as an optical limiter (Fig. 4.6). However, one could optimize a low finesse NLFP (not bistable), which could provide a restricted, approximately flat limiting region.

Threshold / logic element (gate)

A NOR gate based on the two-port characteristic of a NLFP is sketched in Fig. 4.7. Differential gain, and therefore cascadability, is obtained by adding signal beam(s) to a bias beam. The signal beams have to be incoherent, because a device requiring the control of optical paths to interferometric precision is unrealistic. The power of the input signals (spacing of input levels) is determined by the widths of the hysteresis loop, and by the power fluctuations of the source. Broad output states[112] are obtained for the assumed on-axis addressing scheme as a result of the observed differential reflectivities $r_H \approx 1$ and $r_L \approx 0.5$ (Fig. 4.5).

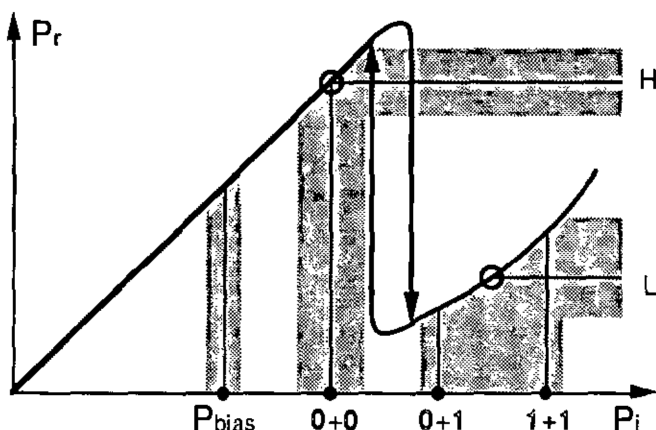

Fig. 4.7: *Cascadable NOR gate (fan-in $f_i = 2$) using an on-axis addressing scheme: the input states correspond to different signal inputs in addition to the bias beam P_{bias}.*

The optimal operating conditions for a desired fan-in and fan-out have been derived and applied to the device parameters of NLFP #360. The results can be summarized as follows: the negating characteristic of NLFP favors its use as a NOR-gate, rather than a NAND-gate, because the differential reflection is smaller in the ON state ($r_L < r_H$). A fan-in of 2 is conceivable for the observed bias fluctuations of 3% P_{ON}, assuming a hysteresis width of the same size. For this case, an optimal bias power of 75% P_{ON} and a cascading attenuation of 0.24, including the fan-out of 2, has been calculated. However, a fan-in of 3 cannot be accommodated, even if a zero hysteresis width is assumed.

Optical memory (latch)

If the device has a bistable characteristic, it can be used as an optical memory by adjusting the bias beam into the hysteresis region (Fig. 4.8). A signal beam will switch the device to the ON-state or leave it in the OFF-state, depending on its amplitude. The memory, or latch, is reset by temporarily reducing the bias beam.

Information storage for up to one second has been demonstrated with NLFP #360 (Sect. 3.5.5). However, this application is not power efficient, because, in addition to the switching energy, the bias power (about equal to P_{ON}) has to be dissipated to maintain the memory in the ON-state.

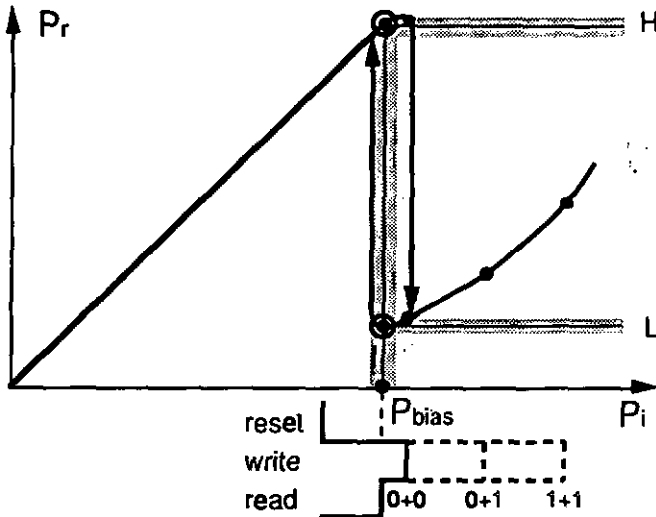

Fig. 4.8: *Latched operation of a NLFP device: the bias beam is located in the hysteresis region. During a write phase, signals may change the output state, which is then read and reset before the next cycle.*

Still, this latching operation can be used to avoid the broad output states of an on-axis addressing scheme, by sequentially resetting, writing, and reading the device[113,112] (Fig. 4.8). With this method one can achieve arbitrary fan-in of time sequential signals, yet at the cost of a complicated clocked addressing scheme, and at a reduced operating speed.

4.2.2 Three-port device

The logic gate and the memory function are inherent three-port elements. Similar to a modulator device, the output is related to two functionally distinct inputs. A signal input switches the device between two possible states and a holding beam supplies the output power, which ideally depends on the device state only. To provide gain, the signal should be small compared to the hold beam. Also, the two inputs should be isolated from one another. Isolation on the input side minimizes the influence of the hold beam on the device state, and isolation on the output side (separation of the reflected input) avoids output fluctuations due to the signal.

In contrast, the NLFP is an inherent two-port device. The logic state of the device depends on the sum of carriers generated within the device volume by the different (incoherent) input beams. The realization of an ideal three-port element is therefore impossible. The two-port I/O characteristic sketched in Fig. 4.5 can nevertheless be improved considerably by separating the reflected signal beams from the hold beam. An optical implementation of a three-port device and the resulting "three-port I/O characteristic" are sketched in Fig. 4.9 and 4.10, respectively.

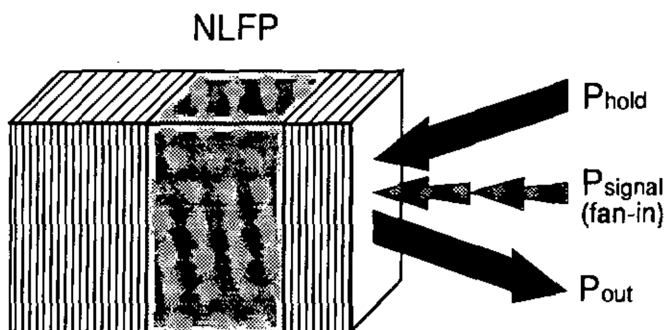

Fig. 4.9 *Optical realization of a three-port device: the hold beam sets the NLFP close to threshold and supplies the output power, while the high or low reflectivity output state is determined by the signal beam(s).*

Gain (fan-out)

In a cascadable system, the differential gain G of a device has to compensate for the power losses which originate from the fan-out f_0 and the attenuation (A) between successive gates

$$G \geq \frac{f_0}{A} . \tag{4-14}$$

The differential gain therefore gives an upper limit for the achievable fan-out f_0. Its maximal value for a bistable device is determined by the aspect ratio of the hysteresis region in Fig. 4.10

$$G \leq \frac{P_{hold}}{P_{sw}} (R_H^{OFF} - R_L^{ON}) . \tag{4-15}$$

The reflectivity in the OFF state R_H^{OFF} guarantees a high throughput, and the ratio R_H^{OFF}/R_L^{ON} defines a contrast ratio of the device. Ideally, the hold power P_{hold} is equal to the threshold P_{th}. In a real device it is smaller, because of tolerance issues (fluctuations of threshold, hysteresis width, hold power and wavelength), and because of the signal power in the OFF state (fi·0). If a logic function other than a NOR-gate, with a threshold th greater than one, is implemented, it is additionally reduced by some ON signals (th·1). No detailed calculation is given here, but it is clear that the achievable gain is highest for a device with a narrow hysteresis loop and a high contrast, used as aNOR gate with a low fan-in fi.

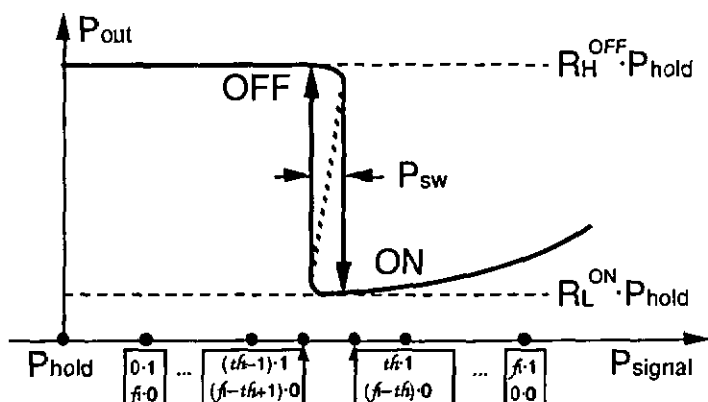

Fig. 4.10 *Three-port characteristic of a NLFP used as a logic gate: reflected hold power P_{out} vs signal power P_{signal}. The input states are determined by the hold beam P_{hold} and the high (1) or low (0) signal inputs (fan-in fi). The threshold th depends on the implemented function (NOR: $th = 1$).*

Gain-bandwidth product

Theoretically, infinite gain and contrast are possible close to the critical detuning (at $\varphi_0\sqrt{F} = \sqrt{3}$ and 2, respectively in Fig. 2.9). In practice, the minimal switching power P_{sw} is determined by device tolerances (cf Sect. 4.3) and by critical slowing down effects (Sects. 3.5.4,8). The observed requirement for an (absorbed) switching energy E_{sw} leads to a limited gain-bandwidth product

$$GBWP \equiv \frac{P_{hold}}{E_{sw}}(R_H^{OFF}-R_L^{ON}) \approx \frac{1}{\tau}\frac{e_i}{e_a}(R_H^{OFF}-R_L^{ON}) . \qquad (4\text{-}16)$$

This estimation is based on an ideal hold power, approximately equal to the steady state threshold (Eq. 4-6). The factor e_i/e_a which will be discussed below allows for a slight improvement (≤ 3) by off-axis addressing. The reflectivity difference $R_H^{OFF}-R_L^{ON}$ is typically larger than 0.5 in impedance matched NLFP (Fig. 2.9b).

Therefore, the carrier recombination rate τ^{-1} is a good approximation for the GBWP of a device. This is in agreement with the GBWP of about 100 MHz found for sample #360 in Sect. 3.5.8. In view of parallel systems, heat dissipation becomes an important issue. If each device of an array dissipates a power $E_{sw} \cdot$GBWP, the 2-dimensional heat sinking capacity limits the number of devices per unit area. Accordingly, an estimated capacity of 100 W/cm^2 imposes a spacing of at least 30 µm between NLFP devices with 1 mW dissipation. This is compatible with a minimum spacing of several diffusion length imposed by cross-talk considerations (Sect. 2.2.3, [55]).

Off-axis addressing

The factor e_i/e_a in Eq. 4-16 accounts for the different efficiencies with which hold and signal beams can be coupled into the cavity. The hold beam has to be initially detuned from the resonance, whereas the signal beams should be coupled resonantly to ensure maximum absorption. This can be realized with an off-axis addressing scheme[114], by making use of the angular dependence of the resonance wavelength (Eq. 2-10). For electronic nonlinearities, one can use a critically detuned hold beam at normal incidence, together with a signal beam of the same frequency, but incident at an off-axis angle[115]. The resonance appears closer to the off-axis signal beam, which is thus absorbed stronger. This freedom allows a theoretical gain improvement of 22/9 (Eq. 2-48), or less, at critical threshold. To compensate for the full critical detuning of 1 nm in the NLFP #360, one would require an angle of about 10° ($\theta_i = 0.17$). The applicability of off-axis addressing to NLFP devices has to be verified experimentally. The influence of beam walk-off at a finite spotsize, and of the reduced finesse at oblique incidence (Eq. 2-10) should be assessed.

Input isolation; (critical biasing)

In intrinsic bistable devices such as the NLFP, the power (and detuning) of the hold beam influences, besides the output level, the switching threshold. This is the origin of the critical biasing requirement for a well-defined, stable holding beam. This inherent lack of input isolation is the major drawback of intrinsic optical devices (cf Sect. 4.3).

Output isolation (addressing)

Partial output isolation is achieved by separating the reflected input beams from the reflected hold beam. To combine and separate the two beams, any combination of polarization-, space- or time diversity could be exploited. The use of orthogonal polarizations for signal and hold beams allows for lossless combination and good isolation at the output, and is therefore the most common choice[116,117]. An angular separation between hold and signal beam may be favorable to improve the gain (off-axis addressing), but is probably not sufficient to allow a good separation of the reflected beams. The use of frequency diversity for addressing is not appropriate if one wants to ensure cascadability.

The resulting three-port characteristic of the reflected hold beam vs the signal input still depends on the applied signal power (Fig. 4.10, 2.9). Better output isolation is achieved with the time sequential, latched addressing, mentioned in Section 4.2.1, where the output states depend on the fluctuations of the hold beam only. However, the clocking is complicated and slows down operating speed.

4.2.3 Fan-in capacity

The fan-in capacity of a device denotes the number of signal channels it accepts with equal sensitivity. The use of coherent optical signals is unrealistic because it would require interferometric alignment precision. The maximal fan-in of a device is therefore equal to the number of optical modes it accepts (Fig. 4.11). This number is determined by the space-time dimensions of the device which were discussed in Sect. 4.1.

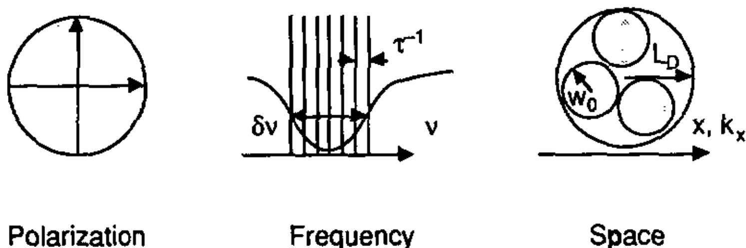

Fig. 4.11 Fan-in capacity due to polarization, frequency and space diversity.

Polarization

Obviously the two polarization modes can be used for fan-in, if they are not already used to distinguish signal and hold beams. The fan-in capacity due to polarization is thus equal to

$$N_\pi = 2\,. \tag{4-17}$$

Time

The device averages intensity fluctuations which are faster than the material recombination time (τ in steady state operation). The number of longitudinal modes N_τ accepted by a NLFP is thus given by the material recombination time τ, and by the spectral resolution of the cavity, $\delta\nu_{cav} = 1/\tau_{cav}$ derived in Eq. 4-4

$$N_\tau = \tau\cdot\delta\nu_{cav} = \frac{\tau}{\tau_{cav\infty}}\left(\frac{1}{1+\mathcal{F}/\mathcal{F}_m}\right) \tag{4-18}$$

This corresponds to the temporal fan-in capacity which is represented as a function of device finesse in Fig. 4.1. For the 2 μm NLFP (#360, $\delta\nu_{cav} \approx 500$ GHz, $\mathcal{F} \approx 35$), close to the asymptotic maximum, N_τ is about 2000. For devices with higher finesse however, the temporal fan-in will decrease almost linearly with finesse. The temporal fan-in capacity is actually restricted to frequency diversity. Time-sequential fan-in of pulses shorter than the recombination time τ is not feasible in a cascaded system, because the duration of the output pulses is given by τ. On the other hand, the use of several beams with frequencies spaced by about 100 MHz, (generated for instance by acoustooptical modulation from one laser source), seems practicable and should be verified experimentally.

Space

Assuming that the device averages spatial carrier density variations within an effective area πL_D^2 given by the diffusion length ($L_D \approx 2.3$ μm), the number of spatial modes is given by the number of diffraction limited spots in that area. For a full solid angle of acceptance $\Omega = 4\pi$ this would be 85. In a FP cavity however, the angle of acceptance $\Omega_{FP} \approx \pi\theta_i^2$ is reduced due to diffraction (Eq. 4-9). Therefore, the spatial fan-in capacity N_σ of a device is

$$N_\sigma = \frac{A\,\Omega}{\lambda^2} = \frac{L_D^2}{w_0^2} = \frac{\mathcal{D}\tau}{\pi w_\infty^2}\left(\frac{1}{1+\mathcal{F}/\mathcal{F}_m}\right). \tag{4-19}$$

The shaded area in Fig. 4.3 shows the spatial fan-in N_σ as a function of finesse. For the assumed material parameters N_σ is always less than 3; it is about 2 for the 2 µm NLFP with $\theta \approx 0.14$, and less than 1 for a finesse above $\mathcal{F}_\sigma \approx 150$ (Eq. 4-13). This shows that spatial fan-in is not practicable in NLFP based on GaAs. Also, it is doubtful if off-axis addressing (sect. 4.2.2) can be used, because the angle corresponding to the critical detuning ($\theta_i = 0.17$) is larger than the angle of acceptance (independent of finesse), and because of other unfavorable effects such as beam walk-off.

Conclusion

The total fan-in capacity ($N_\pi \cdot N_\tau \cdot N_\sigma$) of a NLFP device with a 2 µm thick spacer is about 8000. For $\mathcal{F} \geq \mathcal{F}_m$ this number decreases almost quadratically with finesse. The ratio between temporal and spatial fan-in is a material constant related to the diffusivity $\mathcal{D}$

$$\frac{N_\tau}{N_\sigma} = \frac{1}{\mathcal{D}} \frac{w_\infty^2}{\tau_{cav}^\infty} = \left(\frac{\lambda}{\pi n}\right)^2 \frac{v}{2\mathcal{D}} . \qquad (4\text{-}20)$$

In GaAs this ratio is about 800. The spatial fan-in capacity is extremely limited, but there is a temporal fan-in of about 2000 channels separated by $\tau^{-1} \approx 250$ MHz. Both temporal and spatial fan-in could be improved with a longer carrier recombination time, either by using a different material, or by operating in the critical slowing down regime ($\tilde{t} \geq \tau$, Eq. 2-51). Pixellated devices, with a smaller integrating area, will accept a single spatial mode, while their temporal fan-in will remain unchanged for a given finesse.

4.3 Tolerances

A full hardware tolerancing analysis has already been performed for the nonlinear interference filter (NLIF)[98]. The following discussion focuses on critical biasing only, which is the most severe restriction common to intrinsic devices such as the NLIF and the NLFP. Critical biasing is necessary because the I/O characteristic of these devices is extremely sensitive to fluctuations in the power, and the wavelength detuning of the hold (bias) beam.

4.3.1 Power fluctuations

Hold and signal power are added (incoherently) in the nonlinear spacer. Therefore, to avoid accidental switching, the power of a signal P_{sw} must exceed the fluctuations in the hold power P_{hold}. The achievable gain G

$$G \approx \frac{P_{hold}}{P_{sw}} \leq \frac{P_{hold}}{\Delta P_{hold}} = \left(\frac{P}{\Delta P}\right)_{source} \tag{4-21}$$

is thus limited by the power stability (signal to noise ratio) of the source which provides the hold power P_{hold}. This condition is not too severe because, in practice, speed considerations (critical slowing down, GBWP in Sect. 3.5.4 and 3.5.8, respectively) will impose the minimal switching power P_{sw}. According to the measurements in Sect. 3.5.8, a switching power P_{sw} of 10% of the threshold P_{ON} is a realistic choice which allows for a gain of about 10. For this case, a SNR ≈ 20dB of the source is sufficient to ensure reliable operation. This is fulfilled by the Titanium-Sapphire laser, for which we measured a SNR of 26dB, and it should also be possible with a diode laser.

4.3.2 Wavelength deviation

A much more severe restriction arises from the wavelength sensitivity. According to calculations (Eq. 2-26) and experimental observations (Sect. 3.5.6) the threshold power, and therefore the signal power ($P_{sw} \geq \Delta P_{ON}$), depends strongly on variations $\Delta\lambda$ in the wavelength detuning of the hold beam. Close to the threshold the sensitivity can be approximated by a linear relationship

$$G \le \frac{P_{ON}}{\Delta P_{ON}} \approx \frac{\delta\lambda}{\Delta\lambda} = \frac{\delta\lambda}{\lambda}\left(\frac{\lambda}{\Delta\lambda}\right)_{source}, \quad (4\text{-}22)$$

where $\delta\lambda$ is the spectral width of the Fabry-Perot resonance. The gain is thus limited by the wavelength stability of the source ($\lambda/\Delta\lambda$), and by the finesse of the cavity ($\delta\lambda/\lambda = q\mathcal{F}$). Therefore, to assure the operating stability of 10% (or a gain of 10) with the 2 μm cavity ($\delta\lambda \approx 1$ nm), one requires a wavelength tolerance $\Delta\lambda \le 0.1$ nm. While this requirement is satisfied by the Ti:Al_2O_3 laser, it is hard to achieve with a laser diode: Active stabilization with current or temperature affect the output stability of a laser diode. The required wavelength stability will become more severe for devices with higher finesse.

Wafer homogeneity

Additionally, this wavelength sensitivity restricts the wafer area, on which an array could be operated with a single source. Typical changes of the resonance wavelength of 0.1% per mm (a 1% variation in a central disk of 24 mm) have been measured in Sect. 3.2.1 and 3.5.2. Therefore, with present growth technology, array dimensions of only 0.1 mm (about 1 mm at the wafer center), are feasible for a 10% operating tolerance (gain $\approx$ 10).

Temperature stability

Similarly, the wavelength sensitivity imposes a condition on the temperature variations which can be tolerated for a single device, or between different elements of an array. The impact of a thermal refractive index change on the resonance wavelength is according to Eqs. 3-3, 2-9

$$\frac{\Delta\lambda}{\delta\lambda} = \frac{L}{\mathcal{F}\lambda}\Delta n(T) = \frac{\pi}{\alpha\lambda}\frac{\partial n}{\partial T}\Delta T. \quad (4\text{-}23)$$

The thermal index change $\partial n/\partial T \approx 10^{-3}$ K^{-1} found in Sect. 3.3.3 therefore requires a temperature stability of ≤ 0.7 K (for $\alpha = 250$ cm^{-1}) to assure a 10% operating tolerance.

4.4 Device criteria

The preceding considerations indicate some general issues for optical switching devices based on resonant carrier excitation:

Energy and fan-in

The switching energy of a device is determined by a material dependent energy density that has to be absorbed within the active device volume. Theoretically, a switching energy corresponding to a few photons ($E_0/\mathcal{F}_\tau$, Eq. 4.8) is possible with a device volume which accepts a single spatial and temporal mode (fan-in $N_\pi = 2$). In reality however, the achievable optical confinement is limited. In the case of Fabry-Perot cavities the active volume is limited by diffraction effects related to the finite retardation L_m in the dielectric mirrors. For a spacer thickness smaller than L_m only the fan-in is reduced, but not the limit energy $E_0 \approx 0.2$ pJ. A better confinement, and therefore lower switching energies, can be achieved with waveguiding. Fabry-Perot devices based on GaAs do not provide any practicable spatial fan-in and corresponding waveguide devices would be single (spatial) mode. However, both devices permit a temporal fan-in of about 2000. This temporal fan-in capacity, and the switching energy for the waveguide device, decrease proportionally with finesse.

Gain-bandwidth product and power dissipation

The switching energy requirement, together with the threshold power, implies a limited gain bandwidth product (GBWP) which is essentially equal to the carrier relaxation rate τ^{-1}. This applies not only to intrinsic devices, and can be stated more generally: the gain bandwidth of a device is limited by the rate at which the excitation can be removed from the active device volume.

A large part of this excitation power is generally dissipated as heat. Therefore, the capacity to remove heat ultimately limits the repetitive device operation. This issue is particularly important in view of integrated parallel systems (array devices). A typically assumed heat dissipation capacity of 100 W/cm^2 would limit the density of present devices (threshold: 1 mW) to about 10^5/cm^2.

Device figure of merit

The desire to operate a device with maximum GBWP and fan-in f_i at a minimum switching energy suggests a device figure of merit

$$\mathrm{fom_{device}} \equiv \hbar \frac{\mathrm{GBWP}\, f_i}{E_{sw}} \leq \frac{\sqrt{3}}{2} \eta \left(\frac{n_g \lambda^3}{8 n \delta \bar{n} \delta \bar{n}_G} \right)^{-1} \quad (4\text{-}24)$$

The estimated maximum value ($\approx 10^{-9}$ for intrinsic GaAs devices) is determined by the material figure of merit η (Eq. 4-2) divided by the single mode confinement volume (at $\mathcal{F}_\tau$ in a waveguide, Eq. 4-8), where the fan-in is reduced to $N_\pi = 2$. The figure of merit of real devices, for instance of a NLFP with a finesse smaller than $\mathcal{F}_m$, will be smaller than this figure (cf Table 4.1).

As opposed to fom's which consider speed and switching energy only, this fom is appropriate to evaluate devices for parallel optical computing, because it considers the fan-in capacity. On the other hand, it neglects heat sinking aspects like the overall dissipated power (optical and electrical), and the overall device volume (distance over which heat has to be transported). Although, in practice, one cannot make use of the full fan-in potential of a device because of the tolerancing requirements. Therefore, it is important to first identify the appropriate kind and the minimum required fan-in in order to design an appropriate device.

4.5 Comparison with related devices

The concepts of intrinsic, hybrid and active, optical computing devices are introduced. In Table 4-1 and the following sub-sections, the particularities of the Fabry-Perot device are compared to three mature devices which have been used in optical computing architectures.

4.5.1 Device classification

Intrinsic devices

Intrinsic devices for optical computing are based on refractive or absorptive effects, often related to the local excitation of a resonant electronic transition. A resonant cavity provides positive feedback (except for increasing absorption[118]), enhances the nonlinearity, and transforms phase into amplitude changes.

Thus, the NLFP device and other representatives of this class have similar operating principles and construction; their diversity resides in the nonlinear materials and effects used. Research was originally started on gaseous materials, but rapidly focused on direct gap semiconductors and related multiple quantum well structures (MQW), because of their large resonant nonlinearities. Refractive carrier effects in bulk and MQW AlGaAs, and InP, have been used in NLFP and nonlinear Bragg reflector devices (NLBR). Absorptive switching has been demonstrated[119] in an optically driven asymmetric Fabry-Perot modulator (AFPM)[18]. The potential of organic materials for this application is still being investigated[120].

Intrinsic devices have a simple structure which can often be fabricated in a single fabrication step. Their speed is only limited by the (local) nonlinearity used. Their common drawback is related to the use of the resonant cavity, which imposes coherence requirements and therefore limits fan-in and tolerances.

In the following comparison, intrinsic devices are represented by the NLFP, and the nonlinear interference filter (NLIF) which relies on thermal refractive effect.

Hybrid devices

Hybrid devices have spatially separated detector and modulator parts which are linked by an electrical current. As a consequence, their structure is generally more complicated and their fabrication often involves several processing steps.

One advantage of the hybrid approach is that their functional parts can be optimized independently, although, in practice, this freedom is often restricted by device tradeoffs. The carrier relaxation is based on carrier transport rather than on carrier recombination (or thermal diffusion), which makes hybrid devices potentially faster than all-optical devices. The transported signal may be amplified or even processed in between the two stages. This concept of "smart pixels"[121], has been realized with the self-electrooptic effect device (SEED) devices[122,123], and is being studied for spatial light modulator (SLM) devices. Moreover, the electrically addressable modulators alone can be used as compatible interfacing devices to electronics. It is interesting to note that the optical computing systems demonstrated so far rely on hybrid devices. The only exception is the cellular logic image processor (CLIP) architecture[116,124] which has been built at Heriot-Watt University using NLIF devices.

Two hybrid devices are included in the following comparison: an optically addressable spatial light modulator (OA-SLM) based on a liquid crystal; and the SEED, which relies on external electrical feedback, although the detector and the modulator are the same device.

Active devices

Recently, active bistable hybrid devices like the pnpn optical switch[125], and the surface emitting laser logic (CELL)[16] have gained attention. In these devices, the detector part activates an LED- or a micro laser optical source rather than a modulator, thus promising large optical gain ($\geq 10^4$). Difficulties are related to heat dissipation, series resistance and (electrical) crosstalk.

Although this class of devices looks most promising, the following comparison has been restricted to passive devices because detailed specifications are not available so far.

4.5.2 Comparison of four selected devices

		NLFP/NLBR	NLIF/BEAT	S-SEED	OA-SLM
references			61,126,127	128,129,130,17	131,132,133
physical effect		e-plasma, Δn	thermal, Δn	QCSE, $\Delta\alpha$	$\Delta\sigma$, e.o.
material		GaAs	ZnSe	GaAs-MQW	CdS+nematic LC
wavelength	nm	885	514 to 1064	850	555
dimensions					
pixel volume	μm^3	$\pi \cdot 3^2 \cdot 2$	$\pi \cdot 10^2 \cdot 1$	$10^2 \cdot 1$	$35^2 \cdot (6+2.5)$
pixel spacing	μm	30	≈ 100	20	35
switching					
switching energy E_{sw}	pJ	4	10^5	1	45
switching time	ns	4	10^5	≥ 0.135	$80 \cdot 10^6$
mx. read power P_{read}	mW	1	2	8	$14 \cdot 10^{-6}$
contrast	ratio	10:1	10:1	3:1	41:1
attenuation A	dB	≤ 1	≤ 1	4	1.5
tolerances	10%				
read wavelength	nm	0.1	0.1	≥ 3	≈ 100
signal wavelength	nm	1	1	3	60
homogeneity	mm^2	≤ 1	≈ 100	≈ 1	350
device features					
GBWP AP_{read}/E_{sw}	Hz	$0.2 \cdot 10^9$	$\approx 10^4$	$\approx 10^9$	$2 \cdot 10^2$
fan-in $N_\tau \cdot N_\sigma \cdot N_\pi$		$2000 \cdot 2 \cdot 2$	$\approx 10^8 \cdot 200 \cdot 2$	$\approx 170 \cdot 50 \cdot 2$	$\approx 2 \cdot 10^{12} \cdot 3 \cdot 10^3 \cdot 2$
fom_{device} [Eq. 4-24]	Hz	$\approx 10^{-11}$	$\approx 10^{-13}$	$\approx 10^{-10}$	$\approx 10^{-5}$
operating					
latching		capable	capable	required	not bistable
addressing		critical bias, (off-axis)	crit. bias, off-axis, back side	time sequential, latched, dual rail	back side
output		intensity	intensity	intensity	intensity/polariz.

Table 4.1: Comparison of all-optical switching devices. Data stem from the references, or are estimated, if marked with "≈". (N_τ, N_σ, and N_π denote the temporal, spatial and polarization fan-in, respectively. An f-number of 1 is assumed to estimate the spatial fan-in of SEED and OA-SLM. For NLFP and NLIF, P_{read} is the hold-, or the threshold power.)

NonLinear Fabry-Perot (NLFP)

The reflective NLFP device has a highly nonlinear or bistable, negative I/O characteristic, which is capable of providing differential gain and memory. Used in a three-port addressing scheme with hold and signal inputs of orthogonal polarization, and possibly different angles of incidence, it is suited for operation as a cascadable logic gate or latch.

The scaling laws of NLFP devices have been discussed in Section 4.1. In a Fabry-Perot cavity, the switching energy is limited by diffraction losses. Significant improvement can, however, be expected from waveguiding and carrier confinement. The fan-in capability is essentially temporal.

The principal drawback of the NLFP is the critical biasing requirement which originates from the resonant optical cavity. This extreme sensitivity to wavelength fluctuations in the hold beam puts high demands on the wavelength stability of the driving source, and on the growth homogeneity for potential arrays.

NonLinear Interference Filter (NLIF)

The NLIF has been used successfully to demonstrate optical computing systems[126,134]. Similar to the NLFP, the NLIF relies on a refractive effect inside a Fabry-Perot cavity, but the nonlinearity is the thermally induced refractive index change in ZnSe. As a consequence, this device can be fabricated for a wide range of operating wavelengths, eg for use with an Argon- or Nd:YAG source.

The large time constant τ, characteristic to thermal effects, is responsible for a slow operation speed (sub-ms) and a low GBWP, but increases the temporal fan-in capacity. The corresponding large diffusion spot size ($L_D \approx 25\ \mu m$) facilitates spatial fan-in. While the power levels are comparable to the NLFP, the switching energy is several orders of magnitude higher. Its over-all figure of merit is three orders of magnitude smaller than that of the NLFP.

The relaxation mechanism is based on nonlocal heat transport, rather than local carrier recombination. As a consequence, the recombination time, but not the threshold power, scales with the spacer length (finesse)[135]. This nonlocal property has been exploited in an improved NLIF, the bistable etalon with absorbed transmission[61] (BEAT), where the absorbing layer is placed outside of the cavity. This modification improves switching power, and adds fan-in capability from the rear.

Due to its resonant cavity, the NLIF suffers from the same critical biasing requirement as the NLFP. However, the focusing nonlinearity ($\Delta n_{thermal} > 0$) favors off-axis addressing: unlike the NLFP, the normally incident hold beam does not suffer from beam walk-off, while additional losses are welcome for the off-axis signal beam.

(Symmetric-) Self-Electrooptic Effect Device (S-SEED)

The most prominent example of a bistable hybrid device is the SEED[17] where a layer of intrinsic AlGaAs multiple quantum wells inside a pin-diode operates at the same time as both the detector and the modulator. The electrical coupling of the detector to an external load (originally a resistance, now an identical SEED device in the Symmetric-SEED[136]) introduces feedback via the quantum confined Stark effect[137] (QCSE), and makes the device bistable.

The electrical amplification used in the SEED is low ($P_{el}/P_{opt} \approx 3$). Considering the related material used (AlGaAs-MQW), it is not astonishing that the switching energy and the GBWP are similar to the NLFP device. However, the SEED has potential for faster operation, because the time constant of the QCSE relies on carrier transport, rather than carrier recombination. The shortest reported switching time[128] is 135 ns (without gain, however). This speed is the cause for the small temporal fan-in capacity estimated for the SEED, although its wavelength tolerance (≈3 nm) is larger than that of the NLFP.

An advantage of the (electro-) absorptive effect used in the SEED is that it depends on electrical rather than optical feedback, and therefore does not need a resonant cavity like the NLFP. As a consequence the SEED has notable spatial fan-in, which is the reason for its better device figure of merit. Also, it does not suffer from a critical biasing requirement. On the other hand, the throughput (≈ 30%) and the contrast ratio (≤ 3:1) are low.

The uniqueness of the S-SEED device resides in the concept of symmetric coupling of two identical pin devices. For the cost of a dual rail addressing scheme one gets several desirable features. The S-SEED is bistable in the ratio of two signals, and therefore insensitive to power fluctuations over orders of magnitude. Using a time sequential latched addressing scheme, it can provide large sequential gain, although at proportionally reduced speed. Dual rail encoding allows for positive and negative signals, which is an advantage to implement weights in neural networks, for example. The electrical signal between the two diodes can be amplified or set electrically, leading to a modulator device, and complex logic functions may be realized by connecting several S-SEED's[123].

Optically Addressed Spatial Light Modulator (OA-SLM)

OA-SLM's are the heart of most optical computing systems demonstrated so far. They are based on two-dimensional electrooptic, magnetooptic or mechanical (shutter array) modulators, in conjunction with semiconductor detectors. The values cited in Table 4-1 stem from measurements[133] on a SLM based on a nematic liquid crystal modulator and an amorphous silicon detector[131].

The electrical current between the two functional parts gives potential for large electrical amplification and therefore a high sensitivity and gain. In all measured devices however, the maximum read power, and therefore the achievable gain is (often severely) limited by an insufficient input isolation. Still, in the OA-SLM, as opposed to the other devices, this is a technological, rather than a physical limit.

Due to the missing feedback between the modulator and the detector part, OA-SLM's are generally not bistable (except for ferroelectric modulators), and thus cannot be operated in a latched mode.

The liquid crystal modulator is responsible for the low operating speed. On the other hand, the large time constant, bandwidth and averaging area give rise to extremely large fan-in capabilities. They are the reason for the large figure of merit, and for the success of OA-SLM's in optical computing architectures. It is doubtful, however, that the full spectral range can be effectively used, and that truly integrated SLM devices can be realized.

5 Summary and Outlook

Device measurements

We have optimized and investigated reflective nonlinear Fabry-Perot devices (NLFP) with a nonlinear spacer consisting of bulk GaAs. All our AlGaAs structures were fabricated by molecular beam epitaxy at the Institut de Micro- et Optoélectronique (IMO) at the EPFL in Lausanne.

A NLFP with a 2 µm spacer, which operates at 885 nm, shows bistable switching at a threshold power as low as 1 mW. Thermally stable latched switching has been demonstrated with pulses of 0.5 s duration and heat sinking through the substrate only. A differential gain of up to 8 has been demonstrated by critically biasing the device about 3% below the threshold. Theoretical and experimental investigations of the critical slowing down phenomenon at the switching transition show the existence of a constant switching energy (about 5 pJ), which is independent of the transition time. This energy requirement, together with the observed threshold power, can be associated to a gain-bandwidth product of about 100 MHz.

A NLFP with a spacer of 0.6 µm thickness has also been grown. Because its finesse is not high enough, we were unable to verify our predictions related to thickness scaling. In this device, which operates close to the bandgap, we observed strong transverse effects, indicating index changes close to saturating values. A conclusion is that NLFP devices based on GaAs should be operated at least 25 meV below the bandgap energy. In this bandtail region we have observed an absorption increase with carrier density (for carrier densities below 10^{18} cm^{-3}), which is favorable to reduce the threshold.

In collaboration with IMO-EPFL we have designed and investigated nonlinear Bragg reflector devices (NLBR), where the nonlinear index change is distributed in the high index layers. The nonlinear properties of NLBR are similar to those of NLFP devices, but their simpler construction may be an advantage with respect to growth precision and tuning capability. So far we have observed bistability only in a modified NLBR with an additional linear rear mirror. This structure has still the same complexity as an impedance matched NLFP. However, we see some potential for improvement by using reflectors with more, eventually chirped, dielectric layer pairs.

Theoretical design

Two approaches to the theoretical description of these structures were used: numerical simulations allow to precisely optimize devices and to simulate the effect of modifications and deviations. They are complemented by analytical models with lumped parameters, which are the basis for the physical understanding.

The steady-state operation of NLFP devices is well described by an analytic high finesse model which is extended to include two additional effects. Firstly, the nonlinear refractive effect in GaAs differs from a Kerr material, because the nonlinear index change tends to saturate at high excitation. This can be described by a phenomenological saturating two-level model. Secondly, the finite phase dispersion in the integrated dielectric mirrors has to be accounted for. Close to the Bragg wavelength, these mirrors can be described by a complex reflection coefficient together with an equivalent penetration depth, which we have derived from a coupled wave approach.

We have developed, in close collaboration with IMO-EPFL, a numerical tool to simulate the interaction of general plane waves with dissipative layered structures. The program iterates selfconsistent solutions of the carrier rate equation in each layer, and therefore allows to simulate and optimize structures with an arbitrary number of nonlinear layers. Apart from its application to the NLFP design, the program was useful to optimize nonlinear Bragg mirror structures.

Optical characterization

A setup, based on a modulated tunable laser source, has been built to measure the nonlinear reflection properties of layered structures. Due to the narrow bandwidth and the diffraction limited spatial resolution, this setup is also suited to measure high resolution reflectivity spectra. This optical characterization allows a precise determination of the thickness of resonant optical structures which has been especially valuable to achieve the tight tolerances of typically 0.5% in the epitaxial growth.

Material characterization

Small refractive index changes can be determined accurately by measuring the corresponding wavelength shift of resonant features such as Fabry-Perot resonances. Intensity dependent index changes and their saturation behavior have been determined in this way. The measured values $\Delta n \leq 0.025$ and the

corresponding saturation value $\Delta n_s \approx 0.04$ in bulk GaAs are typically twice as large as in comparable multiple quantum well materials. This favors the use of bulk material for nonlinear devices which rely on carrier plasma effects.

Using this technique to determine nonlinear material parameters, such as the Kerr coefficient n_2 and the cross-section η, is complicated by loss mechanisms. We measured the influence of diffraction and carrier diffusion as a function of spotsize. The results suggest a Kerr coefficient of $n_2 \approx 2 \cdot 10^{-4}$ cm^2/kW, extrapolated for plane wave excitation in GaAs. The measurements confirmed also the assumed recombination time, which allowed us to derive a nonlinear cross-section of $\eta \approx 2 \cdot 10^{-20}$ cm^3. Still, it would be desirable to eliminate the influence of the carrier loss mechanisms, which could be achieved by using large spots and short pulse excitation or by determining the recombination time from independent measurements.

Device scaling: energy and fan-in

Switching in a NLFP device relies on the generation of a critical carrier density N^c in the nonlinear spacer. The nonlinear cross-section η describes the volume in which a single photon generates this density, and is therefore a good figure of merit for the material. The minimum active volume of a Fabry-Perot device is restricted by diffraction, because the longitudinal confinement L_m which can be achieved with dielectric mirrors is limited. We estimate that the switching energy of unconfined NLFP devices saturates at about 0.2 pJ, when the spacer thickness becomes smaller than $L_m \approx 0.7$ µm ($\alpha \approx 200$ cm^{-1}). A further reduction of the switching energy in future devices would require the use of waveguiding (pixellation).

The fan-in capacity of a device is equal to the number of accepted spatial and temporal modes. This is given by the spatial and temporal integration properties of the material (diffusion spot area and carrier recombination time), and the space-time extensions of the cavity (diffraction limited spotsize and photon lifetime). For GaAs devices the spatial fan-in is inferior to 3. However, the temporal fan-in capacity amounts to about 2000 channels, separated by some 100 MHz. This fan-in capacity decreases with increasing finesse. To design an optimum device it is thus important to assess the feasibility of temporal fan-in and the specific fan-in requirements of a particular application.

System and tolerance issues

The narrow spectral bandwidth of NLFP devices limits the temporal fan-in capacity. It is also at the origin of the tight requirements for the critical biasing (wavelength stability of the hold beam). Assuming that switching increments of about 20% threshold are required to avoid critical slowing down, we presume that threshold fluctuations of 10% can be tolerated in a system, allowing for a gain of up to 10. This represents no severe constraint for the stability of potential power sources. However, a severe tolerance issue follows from the wavelength sensitivity of the threshold. Theoretical and experimental investigations show that for the present devices a wavelength stability of ≤ 0.1 nm is required to assure the above 10% tolerance. This stability requirement, besides the wavelength stability of potential sources, restricts temperature deviations to ≤ 0.5 K and limits the area of potential arrays, according to the thickness gradients measured for our wafers, to $0.1 - 1\ mm^2$.

This wavelength tolerance, and the limited fan-in capacity, are the main drawback of NLFP devices. A comparison with three other nonlinear devices for optical computing favors cavity-less hybrid devices, such as spatial light modulators and the SEED. Optoelectronic, rather than all-optical devices are advantageous, in particular where memory, rather than switching is desired. The storage of information with photons is inherently linked to continuous power dissipation because photons, as opposed to electrical charges, cannot be trapped.

ACKNOWLEDGMENTS

First of all, my gratitude goes to Prof. René Dändliker, the director of my thesis, who gave me the opportunity to work on this interesting subject within his applied optics group. His great knowledge and overview have been a valuable and appreciated aid to this research.

I would like to thank the members of the jury, Prof. Franz-Karl Reinhart, Prof. Hans Beck, Dr. Jack L. Jewell and Dr. Jean-Louis Oudar for their interest and their helpful suggestions. Special mention goes to Prof. Reinhart for the support at IMO-EPFL, and for sharing his enthusiasm and his expertise in many interesting discussions.

Significant contributions of this work issued from the stimulating collaboration with Christophe Bagnoud and Dr. Neil Collings at IMT-Uni-NE, as well as Dr. Marc-André Dupertuis, and Michael Proctor at IMO-EPFL. I am grateful to all colleagues and staff members, who contributed to a pleasant and uncomplicated environment at both institutes.

Last but not least, my appreciation goes to Anna Benjamin, all my friends and my family, who endured and supported me with their presence during my time in Neuchâtel.

This work was supported by the Swiss National Science Foundation
(grants 2.255-0.86, 4.045-0.87.13, and 21-30105.90).

BIBLIOGRAPHY

1. D. Prongué, "Diffractive optical elements for interconnections," Ph. D. thesis, Université de Neuchâtel (1992).

2. K.-H. Brenner, "3D-integration of optical digital systems," Optical Computing, 1991, Technical Digest Series (Optical Society of America, Washington, DC 1991), Vol. 6, p. 25, (1991).

3. Special issue on neural networks, Appl. Opt. **26** (23), (December 1. 1987).

4. H. Seidel, "Bistable optical circuit using saturable absorber within a resonant cavity," US Patent 3 610 731, filed May 19, 1969, granted October 5, 1971 (1969).

5. A. Szöke, V. Daneu, J. Goldhar, N.A. Kurnit, "Bistable optical element and its applications," Appl. Phys Lett. **15**, 366 (1969).

6. H.M. Gibbs, "Optical bistability: controlling light with light," Academic Press, Orlando (1985).

7. S.L. McCall, H.M. Gibbs, T.N.C. Venkatesan, "Optical transistor and bistability," J. Opt. Soc. Am. **65**, 1184 (1975).

8. L.A Lugiato, "Theory of optical bistability," Progress in Optics, **21**, (ed. E. Wolf, North Holland, Amsterdam) 69 (1984).

9. H.M. Gibbs, S.L. McCall, T.N.C. Venkatesan," Amplifying characteristics of a cavity-enclosed nonlinear medium," US Patent 4 012 699, filed March 28, 1975, granted March 15, 1979 (1975).

10. F.V. Karpushko, G.V. Sinitzyn, "An optical logic element for integrated optics in a nonlinear semiconductor interferometer," Zh. Prikl. Spektros. **29**, 820 (1978).

11. S.D. Smith, I. Janossy, H.A. MacKenzie, J.G.H. Mathew, J.J.E Reid, M.R. Taghizadeh, F.A.P. Tooley, A.C. Walker, "Nonlinear optical circuit elements as logic gates for optical computers: the first digital optical circuits," Opt. Eng. **24**, 569 (1985).

12. H.M. Gibbs, S.L. McCall, T.N.C. Venkatesan, A.C. Gossard, A. Passner, W. Wiegmann, "Optical bistability in semiconductors," Appl. Phys. Lett. **35**, 451 (1979).

13. H.M. Gibbs, J.L. Jewell, J.V. Moloney, M.C. Rushford, K.Tai, S.S. Tarng, D.A. Weinberger, W.Wiegmann, "Room-temperture optical bistability and self-defocussing in semiconductor etalons," Appl. Phys. B **29**, 171 (1982).

14. H.M. Gibbs, J.L. Jewell, J.V. Moloney, M.C. Rushford, S.S. Tarng, K.Tai, E.A. Watson, A.C. Gossard, S.L. McCall, A. Passner, T.N.C. Venkatesan, W.Wiegmann, "Switching of a GaAs bistable etalon: external switching on and off, regenerative pulsations, transverse effects and lasing," Proc. SPIE **321**, 67 (1982).

15. S.L. McCall, A.C. Gossard, J.H. English, J.L. Jewell, J.F. Duffy, "Operation of a GaAs-AlAs optical logic gate fabricated completely by molecular beam epitaxy," Technical Digest of the Conference on Lasers and Electro-Optics (CLEO), (Optical Society of America), p. 364 (1986).

16. G.R. Olbright, R.P. Bryan, T.M. Brennan, K. Lear, G.E. Poirier, W.S. Fu, J.L. Jewell, Y.H. Lee, "Surface-emitting laser logic," OSA Proceedings on Photonic Switching, H. Scott Hinton and Joseph W. Goodman, eds. (Optical Society of America, Washington, DC 1991), Vol. 8, p. 247 (1991).

17. D.A.B. Miller, D.S. Chemla, T.C. Damen, A.C. Gossard, W. Wiegmann, T.H. Wood, C.A. Burrus, "Novel hybrid optically bistable switch: the quan–tum well self-electro-optic effect device," Appl. Phys. Lett. **45**, 13 (1984).

18. M. Whitehead, G. Parry, "High contrast reflection modulation at normal incidence in asymmetric multiple quantum well Fabry-Perot structure," Electron. Lett. **25**, 566 (1989).

19. J.L. Jewell, A. Scherer, S.L. McCall, A.C. Gossard, J.H. English, "GaAs-AlGaAs monolithic microresonator arrays," Appl. Phys. Lett. **51**, 94 (1987).

20. M. Born, E. Wolf, "Principles of optics", Pergamon Press, Oxford (1980).

21. B.S. Wherrett, "Fabry-Perot bistable cavity optimization on reflection," IEEE J. Quantum Electron. **QE-20**, 646 (1984).

22. D.A.B. Miller, "Refractive Fabry-Perot Bistability with linear absorption: theory of operation and cavity optimization," IEEE J. Quantum Electron. **QE-17**, 306 (1981).

23. E. Garmire, "Criteria for optical bistability in a lossy saturating Fabry-Perot" IEEE J. Quantum Electron. **QE-25**, 289 (1989).

24. J.L. Jewell, Y.H. Lee, S.L. McCall, J.P. Harbison, L.T Florez, "High-finesse (Al,Ga)As interference filters grown by molecular epitaxy," Appl. Phys. Lett. 53, 640 (1988).

25. J.L. Oudar, B. Sfez, R. Kuszelevicz, J.C. Michel, R. Azoulay, "Optical nonlinearities of GaAs-based epitaxial structures for all-optical switching," Phys. Stat. Sol. (b) **159**, 181 (1990).

26. D.E. Grant, H.J. Kimble, "Optical bistability for two-level atoms in a standing wave cavity," Opt. Lett. **7**, 353 (1982). Erratum **8**, 66 (1983).

27. J.D. Jackson, "Classical electrodynamics", Wiley, New York, p. 269 (1975).

28. R. Bonifacio, L.A. Lugatio, "Mean field model for absorptive and dispersive bistability with inhomogeneous broadening," Lett. Nuovo Cimento **21**, 517 (1978).

29. S. Stenholm, "Lasers in applied and fundamental research," Adam Hilger Ltd, Bristol (1985).

30. P. Meystre, M. Sargent III, "Elements of quantum optics," Springer, Berlin (1990).

31. J.S. Blakemore, "Semiconducting and other major properties of gallium arsenide," J. Appl. Phys. Lett. **53**, R123 (1982).

32. S.M. Sze, "Semiconductor devices, physics and technology," Wiley, New York (1985).

33. D.E. Aspnes, "Table of optical functions of intrinsic GaAs: refractive index and absorption coefficient vs energy (0-155 eV)," EMIS Datareview RN=15437, (1985).

34. C. Bosio, J.L. Staehli, M. Guzzi, G. Burri, R.A. Logan, "Direct-energy-gap dependence on Al concentration in AlxGa1−xAs ," Phys. Rev. B **38**, 3263 (1988).

35. H. Kressel, J.K. Butler, "Semiconductor lasers and heterojunction LEDs," Academic Press, New York (1977).

36. H. Haug and S. Schmitt-Rink, "Electron theory of the optical properties of laser-excited semiconductors," Progr. Quantum Electron. 9, 3 (1984).

37. L. Banyai and S.W. Koch, "A simple theory for the effects of plasma screening on the optical spectra of highly excited semiconductors," Z. Physik B **63**, 283 (1986).

38. U. Olin, O. Sahlen, "Model for optical bistability in GaAs/AlGaAs Fabry-Perot étalons including diffraction, carrier diffusion, and heat conduction," J. Opt. Soc. Am. B **7**, 35 (1990).

39. Y.H. Lee, A. Chavez-Pirson, S.W. Koch, H.M. Gibbs, S.H. Park, J. Morhange, A. Jeffrey, N. Peyghambarian, L. Banyai, A.C. Gossard, W. Wiegmann, "Room-temperature optical nonlinearities in GaAs," Phys. Rev. Lett. **57**, 2446 (1986).

40. S. Ovadia, H.M. Gibbs, J.L. Jewell, D. Sarid, N. Peyghambarian, " Evidence that room-temperature optical bistability is excitonic in bulk and quantum well gallium arsenide," Opt. Eng. **24**, 565 (1985).

41. A. Miller, R.J. Manning, P.K. Milsom, D.C. Hutchings, D.W Crust and K. Woodbridge, "Transient grating studies of excitonic optical nonlinearities in GaAs/AlGaAs multiple-quantum-well structures," J. Opt. Soc. Am. B 6, 567 (1989).

42. B.G. Sfez, J.L. Oudar, J.C. Michel, R. Kuszelevicz, R. Azoulay, "High contrast multiple quantum well optical bistable device with integrated Bragg reflectors", Appl. Phys. Lett **57**, 324 (1990).

43. D.S. Chemla, D.A.B. Miller, P.W. Smith, A.C. Gossard, W. T. Tsang, "Large optical nonlinearities in room-temperature in GaAs-AlGaAs multiple quantum well structures," in CLEO Tech. Digest, IEEE, New York (1982).

44. C.D. Poole, E. Garmire, "Bandgap resonant optical nonlinearities in InAs and their use in optical bistability," IEEE J. Quantum. Electron. **QE-21**, 1370 (1985).

45. H. Haug, S.W. Koch, "Quantum theory of the optical and electronic propoerties of semiconductors," World Scientific, Singapoore (1990).

46. U. Olin, "Modelling of optical bistability in semiconductor Fabry-Perot etalons," Ph.D. thesis, Royal Institute of Technology, Stockholm (1990).

47. A. Miller, G. Parry, "Optical bistability in semiconductors with density dependent carrier lifetimes", Opt. Quantum Electron. 16, 339 (1984).

48. B. Sermage, M.F. Pereira, F. Alexandre, J. Beerens, R. Azoulay, N. Kobayashi, "Interface recombination in GaAs-GaAlAs double heterostructures and quantum wells, " Inst. Phys. Conf. Ser. **91**, 605 (1987).

49. P. Mandel, T. Erneux, "Dynamics of nascent hysteresis in optical bistability," Opt. Commun. **44**, 55 (1982).

50. E. Garmire, J.H. Marburger, S.D. Allen, H.G. Winful, "Transient response of hybrid bistable optical devices," Appl. Phys. Lett. **34**, 374 (1979).

51. E.M. Wright, W.J. Firth, J. Galbraith, " Beam propagation in a medium with a diffusive Kerr-type nonlinearity," J. Opt. Soc. Am. B **2**, 383 (1985).

52. D. Weaire, C. O'Carroll, C. Wickham, "Dispersive optical bistability with diffusion: a scaling law," Europhysics Lett. **8**, 25 (1989).

53. B.G. Sfez, R. Padjen, J.L. Oudar, "Experimental evidence of hysteresis narrowing due to carrier diffusion in optical bistable etalons," QELS 91, paper QTuI34, Technical Digest Series (Optical Society of America, Washington DC, 1991), Vol. 11, p. 96 (1991).

54. J.L. Jewell, Y.H. Lee, J.F. Duffy, A.C. Gossard, W. Wiegmann, "Parallel operation and crosstalk measurements in GaAs étalon optical logic devices," Appl. Phys. Lett. 48, 1342 (1986).

55. W.J. Firth, I. Galbraith, "Diffusive transverse coupling of of bistable elements - switching waves and crosstalk," IEEE J. Quantum Electron. QE-**21**, 1399 (1985).

56. D. Frank, B.S. Wherrett, "Optical bistability in cylindrical pixels," Opt. Eng. **26**, 53 (1987).

57. R.J. Ballagh, J. Cooper, M.W. Hamilton, W.J. Sandle, D.M. Warrington, "Optical bistability in a Gaussian cavity mode," Opt. Commun. **37**, 143 (1981).

58. M. Haeltermann, G. Vitrant, R. Reinisch, "Transverse effects in nonlinear planar resonators: modal theory," J. Opt. Soc. Am B **7**, 1309 (1990).

59. U. Olin, "Effects of diffraction and diffusion in dispersive optical bistability in Fabry-Perot etalons," J. Opt. Soc. Am. B **5**, 20 (1988).

60. S.D. Smith, J.G.H. Mathew, M.R. Tagzhizadeh, A.C. Walker, B.S. Wherrett, A. Hendry, "Room temperature, visible wavelength optical bistability in ZnSe interference filters," Optics Comm. **51**, 357 (1984).

61. A.C. Walker, "Reflection bistable etalons with absorbed transmission," Optics Commun. 59, 145 (1986).

62. J.L. Jewell, H.M. Gibbs, S.S. Tarng, A.C. Gossard, W. Wiegmann, "Regenerative pulsations from an intrinsic optical bistable device," Appl. Phys. Lett. **40**, 291 (1982).

63. U. Olin, O. Sahlen, "Theory for the temperature rise in optically bistable GaAs/AlGaAs étalons including diffraction, heat conduction, and carrier diffusion," Opt. Lett **14**, 566 (1989).

64. F. Abeles, "Investigation on the propagation of sinusoidal electromagnetic waves in stratified media," Ann. Phys. (Paris) **5**, 596 (1950).

65. A. Yariv, P. Yeh, "Optical waves in crystals," Wiley, New York (1984).

66. M.A. Dupertuis, M. Proctor, B. Acklin, "Generalization of complex Snell-Descartes and Fresnel laws," submitted to JOSA A.

67. M.A. Dupertuis, B. Acklin, M. Proctor, "Generalized energy balance and reciprocity relations for thin film optics," to be submitted to JOSA A.

68. M.J. Adams, J.V. Collins, J.D. Henning, "Analysis of semiconductor optical amplifiers," IEE Proc., Pt. J: Optoelectron. **132**, 58 (1985).

69. C.H. Henry, R.A. Logan, K.A. Bertness, "Spectral dependence of the change in refractive index due to carrier injection in GaAs lasers," J. Appl. Phys. **52**, 4457 (1981).

70. R.E. Fern and A. Onton, "Refractive index of AlAs, " J. Appl. Phys. **42**, 3499 (1971).

71. H.C. Casey Jr., M.B. Panish, "Heterostructure lasers," Academic Press, New York (1978).

72. S.E. Miller, "Coupled wave theory and waveguide applications, Bell Syst. Tech. J. 33, 661-719 (1954).

73. H. Kogelnik, "Coupled wave theory for thick Hologram gratings," Bell System Tech. Journal, **48**, 2909 (1969).

74. H. Winful, J.H. Marburger, E. Garmire, "Theory of bistability in nonlinear distributed feedback structures," Appl. Phys. Lett. **35**, 379 (1979).

75. J. He, M. Cada, "Optical bistability in semiconductor periodic structures," IEEE J. Quantum. Electron. **QE-27**, 1182 (1991).

76. C. Martijn de Sterke, J.E. Sipe, "Enveloppe-function approach for the electrodynamics of nonlinear periodic structures," Phys. Rev. A **38**, 5149 (1987).

77. P. Rutanera, J.D. Ganière, P-.A. Buffat, "Microscopie électronique en transmission des coins de clivage - application à l'étude du système GaAlAs/GaAs," J. Microscop. Spectroscop. Electron. **13**, 421 (1988).

78. V.S. Speriosu, T. Vreeland Jr, "X-ray rocking curve analysis of superlattices," J. Appl. Phys. **56**, 1591 (1984).

79. J. Hornstra, W.J. Bartels, "Determination of the lattice constant of epitaxial layers of III-V compounds," J. Crystal Growth **44**, 513 (1978).

80. H.B. Bebb, E. Williams, "Photoluminescense (1. Theory)," in Semiconductors and Semimetals: a Treatise (Eds. R.K. Willardson, A.C. Beer), Vol. 8: Transport and optical phenomena, Academic Press, New York (1972).

81. L.C. Andreani, A. Pasquarello, F. Bassani, "Hole subbands in strained GaAs-$Ga_{1-x}Al_xAs$ quantum wells: Exact solution of the effective-mass equation," Phys. Rev. B **36**, 5887 (1987).

82. J. Pankove, "Optical processes in semiconductors," Dover Publications, New York (1975).

83. B.G. Sfez, R. Kuszelewicz, J.L. Oudar, "Measurement of the nonlinear refractive index of semiconductors included in monolithic étalons," Opt. Lett. **16**, 855 (1991).

84. J. Faist, J.D. Ganière, Ph. Buffat, S. Sampson, F.K. Reinhart, "Characterization of GaAs/$(GaAs)_n(AlAs)_m$ surface emitting laser structures through reflectivity and high-resolution electron microscopy measurements," J. Appl. Phys. **66**, 1023 (1989).

85. J. James, M.J. Proctor, C. Faure, W. Baer, F.K. Reinhart, "SiO_2/TiO_2 quarter wave dielectric mirrors for vertical cavity surface emitting lasers," Helv. Phys. Acta Vol. **63**, 513 (1990).

86. Y.H. Lee, A. Chavez-Pirson, B.K. Rhee, H.M. Gibbs, A.C. Gossard, W. Wiegmann, "Direct measurement of dispersive nonlinearities in GaAs," Appl. Phys. Lett 49, 1505 (1986).

87. B. Acklin, C. Bagnoud, M.A. Dupertuis, "Design and investigation of a nonlinear Fabry-Perot device with GaAs spacer layer," Annales de Physique, Colloque n°1, supplément au n°1, Vol. **16**, 11 (1991).

88. B. Segard, J. Segouri, B. Macke, "Switching delays in optical bistability: an experimental study," Opt. Commun. **60**, 323 (1986).

89. P. Mandel, "From optical bistability to optical computing", North Holland, Amsterdam (1987).

90. R. Kuszelewicz, J.L. Oudar, J.C. Michel, R. Azoulay, "Monolithic GaAs/AlAs optical bistable étalons with improved switching characteristics," Appl. Phys. Lett. **53**, 2138 (1988).

91. E. Masseboeuf, O. Sahlen, U. Olin, N. Nordell, M. Rask, G. Landgren, "Low-power optical bistability in a thermally stable AlGaAs étalon," Appl. Phys. Lett. **54**, 2290 (1989).

92. U. Olin, "Model for optical bistability in GaAs/AlGaAs Fabry-Perot étalons including diffraction, carrier diffusion, and heat conduction," J. Opt. Soc. Am. B **7**, 35 (1990).

93. J.L. Jewell, S.L. McCall, A. Scherer, H.H. Hough, N.A. Whitaker, A.C. Gossard, J.H. English, "Transverse modes, waveguide dispersion, and 30 ps recovery in submicron GaAs/AlAs microresonators," Appl. Phys. Lett. **55**, 22 (1989).

94. B. Acklin, M.A. Dupertuis, "Design of an optically bistable Fabry-Perot device based on all-epitaxially grown AlGaAs," Helv. Phys. Acta Vol. **63**, 827 (1990).

95. H.M. Gibbs, J.L. Jewell, J.V. Moloney, K. Tai, S.S. Tarng, D.A Weinberger, A.C. Gossard, S.L. McCall, A. Passner, W. Wiegmann, "Optical bistability, regenerative pulsations, and transverse effects in room-temperature GaAs-AlGaAs superlattice etalons," J. Phys. (Paris) **44**, C2-195 (1983).

96. J.V. Moloney, "Evolution of two-dimensional transverse solitary waves and solitons in an optically bistable resonator," J. Opt. Soc. Am. B **1**, 467 (1984).

97. M.Cada, J. He, B. Acklin, M. Proctor, D. Martin, F. Morier-Genoud, M.A. Dupertuis, J.M. Glinski, "All-optical reflectivity tuning and logic gating in a GaAs/AlAs periodic layered structure", Appl. Phys. Lett. **60**, 404 (1992).

98. B.S. Wherrett, J.F. Snowdon, "Tolerance studies for digital optical computing circuitry, with application to nonlinear interference filters," Int. Journ. of Opt. Computing **1**, 41 (1990).

99. D.S. Chemla, D.A.B. Miller, P.W. Smith, A.C. Gossard, W. Wiegmann, "Room temperature excitonic nonlinear absorption and refraction in GaAs/AlGaAs multiple quantum well structures," IEEE J. Quantum. Electron. **QE-20**, 265 (1984).

100. M. Dagenais, C. Bowden, P. Bhattacharya, P.S. Brody, A.A. Ballmann, G.J. Bjorklund, D.H. Auston et al., "Research on nonlinear optical materials: an assessment," Appl. Opt. **26**, 211 (1987).

101. H.M. Gibbs, G. Khitrova, N. Peyhambarian, "Nonlinear photonics," Springer series in electronics and photonics, Vol. 30, Springer, Berlin (1990).

102. R.T. Bailey, F.R. Cruickshank, D. Pugh, J.N. Sherwood, "Organic electro-optic and nonlinear materials," Int. Journ. of Optoelectronics **5**, 89 (1990).

103. H. Haug, L. Banjay, "Optical switching in low dimensional systems," Plenum Press, New York (1989).

104. G.H. Döhler, H. Künzel, D. Olego, K. Ploog, P. Ruden, H. Stolz, G. Abstreiter, "Observation of Tunable Band Gap and Two-Dimensional Subbands in a Novel GaAs Superlattice," Phys. Rev. Lett. **47**, 864 (1981).

105. M. Wegener, J.E. Zucker, T.Y. Chang, N.J. Sauer, K.L. Jones, D.S. Chemla, "Absorption and refraction spectroscopy of a tunable electron-density quantum-well and reservoir structure," Phys. Rev. B. **41**, 3097 (1989).

106. A. Kost, E. Garmire, A. Danner, P.D. Dapkus, "Large optical nonlinearities in a GaAs/AlGaAs hetero n-i-p-i structure," Appl. Phys. Lett. **52**, 637 (1988).

107. F.V. Karpushko, S.A.Bystrimovich, V.P. Morozov, S.A. Porukevich, G.V. Sinitsyn, I.A. Utkin, "Fast photorefractive effect in high-doped semiconductors: applications to optical bistable interferometric devices," in "Laser optics of condensed matter," (Eds. E. Garmire, A. Kapljanskii, A. Maradudin), Plenum Publish. Corp. New York (1991).

108. P.W. Smith, "On the physical limits of digital optical switching and logic elements," Bell System Technical Journal **61**, 1975 (1982).

109. N.N. Rozanov, "Hysteresis phenomena in distributed optical systems," Sov. Phys. JETP **53**, 47 (1981).

110. A. Scherer, J.L. Jewell, Y.H. Lee, J.P. Harbison, L.T. Florez, "Fabrication of microlasers and microresonator optical switches," Appl. Phys. Lett. **55**, 2724 (1989).

111. B.G. Sfez, E.V. Rao, Y.I. Nissim, J.L. Oudar, "Operation of nonlinear GaAs/AlGaAs multiple quantum well microresonators fabricated using alloy mixing techniques," Appl. Phys. Lett. **60**, 607 (1992).

112. M.E. Prise, N. Streibl, M.M. Downs, "Optical considerations in the design of digital optical computers," Opt. and Quantum Electron. **20**, 49 (1988).

113. B.S. Wherrett, "All-optical computation: a design for tackling a specific physical problem," Appl. Opt. **24**, 2876 (1985).

114. F.A.P Tooley, "Fan-out considerations of digital optical circuits," Appl. Opt. **26**, 1741 (1987).

115. R.Jin, D. Richardson, S.W. Koch, H.M. Gibbs, "Enhancement of differential gain of GaAs etalons by angle tuning of the switch beam," Opt. Eng. **28**, 344 (1989).

116. B.S. Wherrett, R.G.A. Craig, J.F. Snowdon, G.S. Buller, F.A.P. Tooley, S. Bowden, G.S. Pawley, I.R. Redmond, D. McKnight, M.R. Taghizadeh, A.C. Walker, S.D. Smith, "Construction and tolerancing of an optical CLIP," Digital Optical Computing II, SPIE Vol. **1215**, 264 (1990).

117. F.A.P. Tooley, F.B. McCormick, "Design issues in free-space optical interconnection of switching systems," OSA Proceedings on Photonic switching, H. S. Hinton and J.W. Goodman eds., Vol. 8, 38 (OSA, Washington DC 1991).

118. Y. Toyozawa, "Population instability and optical anomalies in high density excited systems," Solid State Commun. **28**, 533 (1978).

119. J.F. Heffernan, M.H. Moloney, J. Hegarty, J.S. Roberts, M. Whitehead, "All optical, high contrast switching in an asymmetric Fabry-Perot etalon," OSA topical meeting on Photonic switching, Salt Lake City (1991).

120. G. J. Bjorklund et al. "Organic and polymeric material," Appl. Opt. **26**, 227 (1987).

121. H.S. Hinton, "Architectural considerations for photonic switching networks," IEEE J. Select. Areas Commun. **SAC-6**, 1209 (1988).

122. A.L. Lentine, D.A.B. Miller, J.E. Henry, J.E. Cunningham, .M.F. Chirovsky, L.A. D'Asaro, "Optical logic using electrically connected quantum well PIN diode modulators and detectors," Appl. Opt. **14**, 2153 (1990).

123. A.L. Lentine, F.A.P. Tooley, S.L. Walker, F.B. McCormick, R.L. Morrisson, L.M.F. Chirovsky, M.W. Focht, J.M. Freund, G.D. Guth, R.E. Leibenguth, G.J. Przybylek, L.E. Smith, L.A. Asaro, D.A.B. Miller, "Integrated SEED photonic switching nodes, multiplexers, demultiplexers, and shift registers," OSA Proceedings on Photonic Switching, H.S. Hinton, J.W. Goodman, eds. (Optical Society of America, Washington, DC 1991) Vol. 8, 65 (1991).

124. S.D. Smith, A.C. Walker, F.A.P. Tooley, B.S. Wherrett, "The demonstration of restoring digital optical logic," Nature **325**, 27 (1987).

125. J.I. Pankove, R. Hayes, A. Majerfeld, M. Hanna, E.G. Oh, D.M. Szmyd, D. Suda, S. Asher, R. Matson, D.J. Arent, G. Borghs, M.G. Harvey, "A pnpn optical switch," SPIE Proceedings, Vol. 963, 191 (1988).

126. S.D. Smith, A.C. Walker, B.S. Wherrett, F.A.P. Tooley, N. Craft, J.G.H. Mathew, M.R. Taghizadeh, I. Redmond, R.J. Campbell, "Restoring optical logic: demonstration of extensible all-optical digital systems," Opt. Eng. **26**, 45 (1987).

127. A.C. Walker, M.R. Taghizadeh, J.G.H. Mathew, I. Redmond, R.J. Campbell, S.D. Smith, J. Dempsey, Guy Lebreton, "Optically bistable thin-film interference devices and holographic techniques for experiments in digital optics," Opt. Eng. **27**, 38 (1988).

128. Preliminary data sheet, 4000-series SEED optical arrays, AT&T Bell Laboratories (1991).

129. A.L. Lentine, F.B. McCormick, R.A. Novotny, L.M.F. Chirovsky, L.A. D'Asaro, R.F. Kopf, J.M. Boyd, "A 2 kbit array of symmetric self-electrooptic effect devices," IEEE Photon. Technol. Lett. **2**, 51 (1990).

130. A.L. Lentine, H.S. Hinton, D.A.B. Miller, J.E. Henry, J.E. Cunningham, L.M.F. Chirovsky, "Symmetric self-electrooptic effect device: optical set-reset latch, differential gate, and differential modulator/detector," IEEE J. Quantum. Electron. **QE-25**, 1928 (1989).

131. A nematic LCLV fabricated for our institute by ASULAB S.A., Neuchâtel.

132. G. Pedrini, B. Acklin, R. Thalmann, "Optical logic and sequential circuits using light valves," report IMT 238EC05/88 (1988).

133. W. Xue, N. Collings, K.J. Weible, "The characteristics of three kinds of LCLV: measurement and comparison," report IMT 305DA10/91 (1991).

134. A.C. Walker, R.G.A. Craig, D.J. McKnight, I.R. Redmond, J.F. Snowdon, G.S. Buller, E.J. Restall, R.A. Wilson, S. Wakelin, N. McArdle, P. Meredith, J.M. Miller, G. MacKinnon, M.R. Taghizadeh, S.D. Smith, B.S. Wherrett, "Design and construction of a programmable optical 16x16 array processor," in Optical Computing, 1991, Technical Digest Series (Optical Society of America, Washington, DC 1991) Vol. 6, 199 (1991).

135. D.C. Hutchins, B.S. Wherrett, C. Wang, "Theory and optimization of optical bistability in multilayer interference filters," Int. Journ. of Optoelectronics, **5**, 179 (1990).

136. A.L. Lentine, H.S. Hinton, D.A.B. Miller, J.E. Henry, J.E. Cunningham, L.M.F. Chirovsky, "Symmetric self-electro-optic effect device: optical set-reset latch," Appl Phys. Lett. **52**, 1419 (1988).

137. D.S. Chemla, T.C. Damen, D.A.B. Miller, A.C. Gossard, W. Wiegmann, "Electroabsorption by Stark effect on room-temperature excitons in GaAs/GaAlAs multiple quantum well structures," Appl. Phys. Lett. **42**, 864 (1983).

INDEX

Absorption coefficient 25
Absorption saturation 23
AC-Stark effect 27
Acoustooptic modulator 77
Active devices 145
Airy function 11
Airy's formula 53
AlGaAs alloy 30
Ambipolar diffusion 34,127
Balanced cavity 15
Band matrix 45
Band structure 29
Band-filling 31
Bandgap renormalization 31
BEAT 147
Boundary interfaces 53
Bragg condition 50
Carrier diffusion 37
Carrier rate equation 34
Cavity build-up time 122
Cavity round-trip phase 9
Conductivity 25,74
Contrast ratio 11,134
Coulomb enhancement 29
Coupled wave theory 50
Critical biasing 106
Critical energy density 121
Critical slowing down 35
Critical switching 18
Density matrix 27
Detuning 11,17
Detuning dependence 102
Device figure of merit 142
Dielectric properties 24
Differential gain 134
Differential reflectivity 111
Diffraction effects 39,125
Diffusion 34,38,127
Dipole matrix element 21 26
Doping concentration 74
Dynamic stability 100
Effective spacer length 59
Electrical characteristics 74
Equivalent thickness 52,122
Exciton 29
Experimental setup 75
Fabry-Perot resonance 11
Fan-in capacity 137
Fan-out 134
Finesse 12
Finesse parameter 16
Free spectral range 11
Fresnel laws 43
Fresnel number 125
Gain-bandwidth product 135
GaAlAs 29
Graphical solution 17
Group index 59
Harmonic plane waves 41
Heat dissipation 40,142
High finesse limit 15
Hybrid devices 145
Hysteresis region 19
Impedance matching 14
Index saturation 21
Inhomog. plane waves 44
Input isolation 136
Intrinsic devices 144
Kerr coefficient n2 17,92
Kramers-Kronig relations 25
Lattice constant 72
Light velocity 42
Material figure of merit 121
Matrix-inversion method 31
MBE 71
Minimum threshold 18
Mirror coefficients 8
Mott density 31
MQW heterostructures 33
NLB program 45
NL Bragg Reflector 112
Nonlinear cross-section 16,92
NL Interference Filter 147
Nonlinear materials 121
NOR gate 135
Normal dispersion 30
Normalized reflectivity 10
Off-axis addressing 136
Optical bistability 17
Optical limiter 131
Optical memory 132
Oscillator model 26
Output isolation 137
Peltier cooler 78
Phase mismatch 50
Photoluminescence 73
Photon lifetime 122
Plasma frequency 26
Plasma theory 32
Polarization 25,138
Power fluctuations 140
Poynting vector 45
Pulse area scaling law 36
Pulse shaping 131
Pulsed operation 40
Rabi frequency 27
Rate equation 34
Rayleigh length 40
Reactive ion etching 84
Recombination 34,47,92,122
Reflectivity spectra 79
Refractive index 25,30,89
Reversibility 9
RHEED 83
Round trip attenuation 9
Saturating index 21,93
Screening 31
S-SEED 148
Smart pixels 145
Spatial Light Modulator 149
Spectral resolution 77
Spotsize dependence 103
Sputtering 86
Standing wave effects 38
Stopband 52
Surface emitting laser 145
Switching energy 35,99,128
Switching 123
Switching wave 39,127
TEM 71
Thermal index change 87
Thermal stability 40,100,141
Thickness gradient 96,141
Three-port device 133
Threshold 97,105,123
Threshold / logic element 131
Threshold criterion 99
Throughput 134
Time-power tradeoff 37
Ti:Al_2O_3 laser 77
Tolerances 140
Transverse crosstalk 39
Two-port characteristic 130
Vacuum polarization 24
VCSEL 85
Vignetting 78
Wafer homogeneity 141
Wave impedance 41
Wave vector 41
Waveguide confinement 124
Wavelength deviation 140
X-Ray Diffraction 72